Nonlinear Frequency Response Analysis for the Diagnosis of Polymer Electrolyte Membrane Fuel Cells

Dissertation
zur Erlangung des akademischen Grades
Doktoringenieur
(Dr.-Ing.)

von:	Dipl.-Ing. (FH) Thomas Kadyk
geb. am:	22.02.1982
in:	Dessau

genehmigt durch die Fakultät für Verfahrens- und Systemtechnik
der Otto-von-Guericke-Universität Magdeburg

Gutachter:	Prof. Dr. Ing. Ulrike Krewer
	Prof. Dr. Francois Lapicque
	Prof. Dr.-Ing. Kai Sundmacher
eingereicht am:	03.04.2012
Promotionskolloquium am:	09.11.2012

Zusammenfassung

In der vorliegenden Arbeit wird untersucht, ob die Methode der nichtlinearen Frequenzganganalyse (engl. Nonlinear Frequency Response Analysis, NFRA) für die Diagnose von Polymerelektrolytmembran-Brennstoffzellen (engl. Polymer Electrolyte Membrane Fuel Cell, PEMFC) geeignet ist. Die NFRA ist ein vielversprechender Ansatz, da sie in-situ und während des laufenden Betriebes einsetzbar ist und mit geringem gerätetechnischen Aufwand leicht implementiert werden kann. Mit der NFRA ist es möglich, kritische Zustände von Brennstoffzellen zu diagnostizieren, welche zu Leistungsverlust, erhöhter Degradation oder Zellschädigung führen können. Der Fokus der Arbeit liegt auf den reversiblen kritischen Zuständen, welchen durch eine Änderung der Betriebsparameter entgegengewirkt werden kann. Daher wurden speziell die Zustände der Austrocknung, Flutung und der Vergiftung mit Kohlenstoffmonoxid in PEMFC untersucht.

In ersten Voruntersuchungen wurde die NFRA an einer PEM-Brennstoffzelle im technisch relevanten Massstab zur Diagnose der oben genannten Zustände erprobt. Dabei wurde ein vereinfachter mathematischer Ansatz der NFRA verwendet, welcher es ermöglicht die Frequenzgänge erster und zweiter Ordnung ($H_{1,0}$ und $H_{2,0}$) simultan zu ermitteln. Dabei wurde festgestellt, dass $H_{1,0}$ unter Flutungsbedingungen klare Merkmale (vor allem einen Anstieg des Stofftransportwiderstandes) zeigt, welche zur eindeutigen Diagnose von Flutung eingesetzt werden können. Leider sind die Merkmale der $H_{1,0}$ Spektren unter Austrocknung und CO-Vergiftung qualitativ gleich, so dass eine eindeutige Diagnose dieser beiden Zustände nicht möglich ist. Interessanterweise zeigen die $H_{2,0}$ Spektren während dieser beiden Zustände jedoch qualitativ unterschiedliche Merkmale, die eine Unterscheidung von Austrocknung und CO-Vergiftung und damit eine eindeutige Diagnose ermöglichen.

Diese Beobachtungen motivierten eine weitere, detailiertere Untersuchung von Austrocknung und CO-Vergiftung. Das Ziel dabei war einerseits aufzuklären, warum die $H_{1,0}$ Spektren in beiden Fällen gleiche Merkmale zeigen und andererseits die mögliche Nutzung der $H_{2,0}$ Spektren zur Diagnose beider Fälle genauer zu untersuchen. Dazu wurde ein kombinierter Ansatz von Experiment und Modellierung entwickelt. Auf experimenteller Seite wurde eine differenzielle H_2/H_2-Zelle entworfen, in welcher maskierende Effekte durch die langsame Sauerstoffreduktion auf der Kathode durch den Austausch dieser Reaktion mit der schnellen Wasserstoffentwicklung unterdrückt wurden. Außerdem wurden durch differenziell kurze Kanäle Konzentrationsgradienten entlang des Kanals vermieden. Dieser experimentelle Ansatz

ermöglichte eine stark vereinfachte Modellierung, welche die numerische Berechnung der NFRA-Spektren erlaubte.

An dieser differenzielle H_2/H_2-Zelle wurden NFRA-Spektren unter anodischer CO-Vergiftung gemessen. Zunächst wurde ein praxisrelevanter Arbeitspunkt bestimmt, der eine beginnende CO-Vergiftung simuliert. An diesem Arbeitspunkt wurden NFRA-Spektren gemessen und der Einfluss der CO-Konzentration auf diese untersucht. Die Hauptmerkmale der NFRA-Spektren unter CO-Vergiftung wurden identifiziert. Zusätzlich zu den Messungen wurde ein vereinfachter Modellierungsansatz aus der Literatur genutzt um NFRA-Spektren der differenziellen H_2/H_2-Zelle unter CO-Vergiftung zu simulieren. Dadurch konnte bestätigt werden, dass die gemessenen Hauptmerkmale der Spektren vom CO-Vergiftungsmechanismus (d.h. der Blockade der Katalysatorplätze durch präferenzielle Adsorption von CO) verursacht werden.

In weiteren Messungen wurden NFRA-Spektren unter Austrochnung an der differenziellen H_2/H_2-Zelle gemessen. Dabei wurde in den $H_{1,0}$ Spektren neben der erwarteten Verschlechterung des Protonentransportes in der Membran auch eine viel dominierndere Verschlechterung der Reaktionskinetik gemessen. Eine Hypothese für diese Beobachtung war, dass die Austrocknung der Zelle auch zu einer Verringerung des Protonentransportes im Polymernetzwerk der Katalysatorschicht führt. Somit wird die protonische Anbindung von Katalysatorpartikeln zur Membran verschlechtert und weiter entfernte Katalysatorplätze werden inaktiv. Dies führt zum Verlust von aktiver Katalysatorfläche und damit zur beobachteten Verschlechterung der Reaktionskinetik.

Um diese Hypothese zu bestätigen, wurde ein Modellansatz verwendet. Dazu wurde ein Modell der differenziellen H_2/H_2-Zelle mit zusätzlichem Protonentransport in der Katalysatorschicht aufgestellt. Mit diesem Modell wurden NFRA-Spektren unter Austrocknungbedingungen numerisch simuliert. Dabei konnte die in den experimentellen $H_{1,0}$ Spektren beobachtete Verschlechterung der Reaktionskinetik qualitativ abgebildet werden. Zusätzlich bildeten die Modellergebnisse auch die qualitativen Hauptmerkmale der $H_{2,0}$ Spektren unter Austrocknung ab.

Leider bildete das Modell die Verschlechterung der Reaktionskinetik nur qualitativ aber nicht quantitativ ausreichend ab. Ursache war, dass die Verringerung des Protonentransportes in der Katalysatorschicht nur auf Basis der geänderten Gasbefeuchtung abgeschätzt wurde, was nicht ausreichend war. Eine weitere Verringerung des Protonentransportes war notwendig, um die experimenellen Daten auch quantitativ zu erfassen. Diese Verringerung könnte vom elektroosmotischen Wassertransport verursacht werden, welcher aus Komplexitätsgründen nicht im Modell berücksichtigt wurde.

Zuletzt wurden die Hauptmerkmale der NFRA-Spektren der differenziellen H_2/H_2-Zelle unter CO-Vergiftung und Austrocknung verglichen. In den $H_{1,0}$ Spektren wurden in beiden Fällen gleichartige Merkmale festgestellt (wie schon in der technischen Zelle), insbesondere eine Verschlechterung der Reaktionskinetik verursacht von einer verringerten aktiven Katalysatorfläche. Daher ist die Verwendung der $H_{1,0}$ Spektren nicht ausreichend für eine eindeutige Diagnose. Die $H_{2,0}$ Spektren bieten jedoch qualitative als auch quantitative Unterschiede, welche eine eindeutige Diagnose erlauben.

Abschließend muss jedoch erwähnt werden, dass die NFRA-Methode leider schwierig ist. Die praktische Messung der NFRA-Spektren erfordert selbst in der stark vereinfachten differenziellen H_2/H_2-Zelle eine sorgfältige Messprozedur, speziell im Hinblick auf die Bestimmung der korrekten Anregungsamplitude, das Messrauschen und die Reproduzierbarkeit der Messungen. In den Modellierungsarbeiten wurde festgestellt, dass die ermittelten Spektren höherer Ordnung sehr anfällig gegen Parameterungenauigkeiten ist. Außerdem erfordern komplexere Modelle einen wesentlich höheren Aufwand für die numerische oder analytische Ermittlung der NFRA-Spektren. Insgesamt zeigen die Frequenzgänge höherer Ordnung ein sehr viel komplexeres Verhalten, welches nicht direkt einzelnen Prozessen zugeordnet werden kann und eine Interpretation sehr schwierig und wenig intuitiv macht.

In dieser Arbeit wurde neben dem Hauptaspekt der NFRA für die Diagnose von PEM-Brennstoffzellen noch ein weiterer Nebenaspekt untersucht. Während der Messungen zur CO-Vergiftung an der differenziellen H_2/H_2-Zelle konnten zum ersten Mal autonome Spannungsoszillationen in einer Brennstoffzelle mit Platinkatalysator beobachtet werden. In einer ersten Messreihe wurde der Einfluss der CO-Konzentration auf das Verhalten der Oszillationen untersucht. Eine größere CO-Konzentration erhöht die Oszillationsfrequenz aufgrund der schnelleren CO-Adsorption. In einer zweiten Messreihe wurde der Einfluss der Zelltemperatur untersucht. Durch eine Bestimmung der Aktivierungsenergie wurde ein unterschiedlicher Temperatureinfluss am Platin (E_a = 40.5$\pm$0.6 kJ mol^{-1}) als bei in der Literatur genannten Oszillationen an Platin-Ruthenium (E_a = 60.9 kJ mol^{-1}) festgestellt. Des weiteren wurden in der differenziellen Zelle auch Oszillationen im H_2/O_2-Betrieb gemessen. Diese treten auf, wenn die Anodenüberspannung bis auf Werte erhöht wird, an denen die CO-Oxidation am Platin einsetzt. Solche Anodenüberspannungen werden jedoch im normalen Brennstoffzellenbetrieb an passiven Lasten nicht erreicht, da ein großer Teil der Zellüberspannung durch die Überspannungen von Kathode und Membran verursacht werden. Allerdings konnten durch Verwendung der differenziellen H_2/H_2-Zelle diese Oszillationen enthüllt werden.

Acknowledgements

I would like to acknowledge the ministry of culture and education and the ministry of economics of the Federal State of Saxony-Anhalt as well as the Federal Ministry for Education and Research (BMBF) for funding the projects “Intel-FC – Intelligente Diagnosesysteme, Monitoring Technologien, und Steuerungsverfahren zur Optimierung des Betriebs von Brennstoffzellen”(project number: 6003286500) and “NEWE – Netzwerke elektrochemischer Wandler zur Energieerzeugung”. My reseach was funded by these projects as well as by additional funding from the Max-Planck Institute of Dynamics of Complex Technical Systems. I am very thankfull for these fundings.

Furthermore, I would like to acknowledge the professional work of Anne Koch (http://www.koch-uebersetzungen.de/), who proof-read the manuscript and many of my english publications during my scientific carreer. Her high-quality critics and insight into the english language is of high value for my english language skills and improved the quality of my publications significantly.

Contents

1 Introduction **1**

2 Critical States of PEMFC and Methods for their Diagnosis **5**

2.1 Critical States of PEMFCs 5

2.1.1 Irreversible critical states 6

2.1.2 Reversible critical states 12

2.2 Methods for Diagnosis 18

2.2.1 Diagnosis of Water Management Issues 19

2.2.2 Diagnosis of CO Poisoning 24

2.2.3 Conclusions 24

3 Nonlinear Frequency Response Analysis **26**

3.1 Nonlinear Electrochemical Methods 26

3.2 Principle of the NFRA Method 27

3.3 Analytical Derivation of Higher Order Frequency Response Functions 29

3.4 Experimental and Numerical Derivation of Higher Order Frequency Response Functions 33

4 Experimental **39**

4.1 Experiments with PEMFCs of Technical Size 39

4.2 Experiments with Differential H_2/H_2 cells 41

4.3 Reproducibility 43

5 NFRA for Diagnosis of Dehydration, Flooding and CO Poisoning in a PEMFC of Technical Size **46**

5.1 Normal Conditions 47

5.2 Dehydration and Flooding 47

5.3 CO-Poisoning 53

5.4 Conclusions 57

6 CO poisoning in the Differential H_2/H_2 Cell **59**

6.1 Autonomous Potential Oscillations at the Pt Anode of a PEM Fuel Cell under CO Poisoning 60

6.2 Experimental NFRA Spectra of a Differential H_2/H_2 Cell under CO Poisoning 71

6.3 Modeling and Simulation of NFRA Spectra of a Differential H_2/H_2 Cell under CO Poisoning 75

6.4 Conclusions 82

7 Dehydration Phenomena in the Differential H_2/H_2 Cell **85**

7.1 Experimental Results 85

7.2 Simulation of Dehydration Phenomena in the Catalyst Layer 87

7.3 Comparison of Key Features of NFRA Spectra under CO Poisoning and Dehydration 98

7.4 Conclusions 100

8 Summary and Conclusions **103**

Symbols

Latin

a	internal surface area of the catalyst	m^2_{act} m^{-2}_{geom}
a_{H_2O}	activity of water	[0...1]
A	amplitude	A m^{-2}
$b_{c/h}$	Tafel slope of CO or hydrogen electrooxidation	V
$b_{fc/fh}$	ratio of desorption to adsorption rate constant for CO or H_2	[0...1]
c	concentration	mol m^{-3}
C_{cat}	molar area density of active sites	mol m^{-2}_{act}
$C_{dl,a/c}$	anodic or cathodic double layer capacity	F m^{-2}_{act}
d_M	thickness of the membrane	m
$D^{eff}_{\alpha,\beta}$	effective diffusion coefficient of species α in β	m^2 s^{-1}
E^0	standard electrode potential	V
f	frequency	Hz
F	Faraday constant, 96485.3 A s mol^{-1}	
g	material flux	mol m^{-3}
$h_n(\omega_1, ..., \omega_n)$	generalized impulse function or Volterra kernel of order n	
H_n	n-th order frequency response function	
$H_{q,n}$	n-th order quasi-frequency response function	
i	current density	A m^{-2}
i^0	exchange current density	A m^{-2}
I	current	A
I_r	reverse current of a diode	A
$k_{ec/eh}$	rate constant of CO or H_2 electrooxidation	mol m^{-2}_{act} s^{-1}
$k_{fc/fh}$	rate constant of CO or H_2 adsorption	mol m^{-2}_{act} s^{-1}
N_{ns}	number of neighbouring active sites	
p	pressure	Pa

$r_{CO/H}^{ads/des/ox}$	rates of CO or H_2 adsorption, desorption or oxidation	mol m_{act}^{-2} s^{-1}
R	universal gas constant, 8.31451 J K^{-1} mol^{-1}	
R_M	membrane resistance	Ω m_{geom}^{-2}
S_{act}	active surface area	m^2
t	time	s
T	temperature	K
U	voltage	V
U_{cell}	cell voltage	V
U_t	thermal voltage of a diode	V
$x_{CO/H}$	mole fraction of CO or hydrogen	[0...1]
$x(t)$	input signal	
$y(t)$	output signal, response signal	

Greek

$\delta(\Delta G_{CO})$	variation of adsorption free energy between Θ_{CO}=0 and Θ_{CO}=1	J mol^{-1}
$\delta(\Delta E_H)$	change in activation energy for hydrogen dissociative adsorption near CO occupied site	J mol^{-1}
$\Delta\phi_a$	anode potential difference between solid and liquid phase	V
ϵ	correction factor	m_{act}^2 m_{act}^{-2}
$\eta_{a/c}$	anode or cathode overpotential	V
$\Theta_{CO/H}$	coverage of catalyst with CO or hydrogen	[0...1]
Θ_{Pt}	free active Pt catalyst sites	[0...1]
ι	charge flux	A m_{act}^{-2}
$\kappa_{l/s}^{eff}$	effective conductivity of the liquid phase (i.e. polymer) or solid phase in the catalyst layer	S m^{-1}
κ_m	proton conductivity of the membrane	S m^{-1}
τ	time constant	s
$\phi_{l/s}$	potential of the liquid or solid phase	V
ω	angular frequency, = 2π f	s^{-1}

Subscripts

0	reference conditions
a	anode
act	active area
c	cathode
CO	carbon monoxide
eh	electrooxidation of hydrogen
ec	electrooxidation of carbon monoxide
fh	adsorption of hydrogen
fc	adsorption of carbon monoxide
$geom$	geometric area
H	hydrogen
H_2O	water
l	liquid phase
m	membrane
Pt	platinum
s	solid phase
t	total
WP	working point

Superscripts

ads	adsorption
des	desorption
eff	effective
ox	oxidation
red	reduction

Chapter 1

Introduction

Today's energy supply encounters two main problems: on the one hand, the emission of greenhouse gases causes an anthropogenic climate change with negative consequences for natural and human systems on a global scale [1]. On the other hand, fossil energy sources, on which today's energy supply is mainly based, are limited and expected to run out within the next generations [2]. Possible solutions and mitigation strategies for these problems include the use of sustainable, renewable energy sources and the increase of the efficiency in the use of energy.

Fuel cells play a key role in this context. On the one hand, they are able to use a variety of fuels. This opens up the possibility to use renewable energy sources like biogas, methanol, ethanol or hydrogen produced by reforming of renewable hydrocarbons. Furthermore, the combination of fuel cells and hydrogen production from electrolysis might be used as an intermediate energy storage for intermittent sources like solar or wind energy. On the other hand, they have the potential to reach a high efficiency as direct converters of chemical into electrical energy. This is possible, because in contrast to conventional combustion engines, fuel cells are not subject to the restrictions of the Carnot cycle. Therefore, they are not limited to its efficiency, which is strongly temperature dependent and reaches acceptible values only at very high temperatures. In contrast, the thermodynamic efficiency of the fuel cell reaches high values even at low temperatures which are more favourable from a material and operation point of view.

It is aimed to use fuel cells in the fields of automobile, stationary and decentralised energy supply. In the medium-term, fuel cells might be introduced into these fields via niche markets like auxiliary, uninterruptible or self-sufficient power supply as well as power supply for warehouse vehicles, light vehicles and boats. In form of micro fuel

cells, they might be an alternative to lithium ion batteries in small and micro mobile devices [3].

Polymer electrolyte membrane fuel cells (PEMFCs), which are the subject of this work, are highly suitable for most of these applications. Their design, function and principle is described in detail in the literature [4–8] and is therefore not repeated here. The advantages of PEMFCs are easy operation management, low operation temperature, the ability for fast load changes, quick start-up and shut-down, good scalability and a high technical maturity. Compared to their strongest conventional competitors, i.e. combustion engines and combined heat and power units, the disadvantages of PEM fuel cells are their high price and low durability.

Furthermore, the operation of a PEM fuel cell is not a trivial task. Improper operation of PEMFCs can lead to critical states (e.g. improper water management can lead to dehydration or flooding of the cell), which can result in performance loss, enhanced degradation or even damage of the cell. In order to prevent or react to such critical states, a clear diagnosis of the cell is necessary. Ideally, a method for such a diagosis should be applicable in-situ and during operation. It should be simple, practically applicable and useable on unmodified commercial cells.

Methods which use the electrical input-output behaviour can fulfil these requirements and are preferred because they can be easily implemented, e.g. in power electronics like DC/DC or DC/AC converters which are already present in the fuel cell system.

The best developed method on this basis is Electrochemical Impedance Spectroscopy (EIS). It is widely used for the analysis of PEMFCs under laboratory conditions and attempts were made to use it for practical diagnosis. However, under certain operation conditions ambiguities in the results of EIS have been reported. These might result from the linear analysis principle of EIS applied to the highly nonlinear PEMFC system. Due to these ambiguities, a clear diagnosis of the PEM fuel cell by means of EIS is not possible in all cases.

Aim and Approach of This Work

The aim of this work is to analyse the applicability of the so-called nonlinear frequency response analysis (NFRA) method for fuel cell diagnosis. NFRA has the potential to overcome the aforementioned drawbacks of EIS, because it is a nonlinear analysis method. With NFRA, not only the linear electrochemical impedance spectra are obtained (as with EIS) but also nonlinear spectra of higher order, which contain additional

information about the nonlinearities of the system.

Using the NFRA method, this work analyses on the one hand, why the linear spectra can be ambiguous for some critical states and evaluates on the other hand, if the nonlinear information obtained with NFRA can be used for a discrimination of these states. To do so, at first possible critical states in a PEMFC have been reviewed systematically (Chapter 2). Reversible critical states are most relevant for practical diagnosis, because they can be counteracted by changing the operation conditions. Therefore, they have been chosen for further analysis. Methods for the diagnosis of these states were reviewed with respect to their applicability. As mentioned before, EIS was found to be the most suitable method for practical diagnosis but is not sufficient for the discrimination of certain critical states. Therefore, the NFRA method (explained in Chapter 3) was adapted for fuel cell diagnosis.

In preliminary experiments (described in Chapter 4), NFRA was used for the diagnosis of the most important critical states flooding, dehydration and CO poisoning in a PEMFC of technical size (Chapter 5). It was seen that the NFRA spectra of the first order, which are identical with classic EIS spectra, can be used to identify flooding but show similar qualitative features under dehydration and CO poisoning. However, the spectra of the second order showed qualitatively different characteristics, which might be used for the discrimination of these two cases.

In order to clarify these preliminary results in detail, a combined experimental and modelling approach was used. A special experimental approach was developed [9–11], because a fuel cell of technical size and dimensions is rather complex, interesting processes might be masked and the modelling of such a system is very intricate. Therefore, a differential fuel cell design was developed, in which a very short channel length and highly over-stoichiometric gas flow rates avoided along-the-channel effects like concentration gradients, fuel gas starvation or CO accumulation. Additionally, H_2/H_2 operation, well established in literature [12–14], was used to avoid the slow cathodic oxygen reduction kinetics and to prevent cathodic land-channel effects like oxygen starvation or water accumulation under the ribs [15].

With this setup, the case of CO poisoning was investigated (Chapter 6). In a first step, steady-state polarisation curves were measured in order to find a suitable working point for the intended NFRA measurements. During these measurements, in galvanostatic operation autonomous potential oscillations were found for the first time in a PEMFC with Pt catalyst. The mechanism and occurence of the CO oscillations was analysed in order to determine a working point for the NFRA which is reliable in the non-oscillatory region. This was necessary because otherwise the autonomous oscilla-

tions would interfere with the applied perturbation of the NFRA method. This would lead to a much more complex behaviour and would require a much more complicated analysis.

At the determined working point, NFRA spectra at different levels of CO poisoning were measured and analysed. Furthermore, the differential H_2/H_2 cell made a simplified modelling approach possible focussing on the main CO poisoning mechanism. From the comparison of experimental and numerically simulated NFRA spectra, key features of the NFRA spectra under CO poisoning could be identified, which might be useful as a "fingerprint" for diagnosis.

In the next step, NFRA spectra under dehydration conditions were investigated in the same differential H_2/H_2 cell setup (Chapter 7). It was seen that the first order spectra (i.e. EIS spectra) under dehydration showed similar qualitative behaviour as under CO poisoning: a strong decrease in the anodic reaction kinetics. For the case of CO poisoning this decrease was caused by the CO poisoning mechanism but for the case of dehydration this behaviour was not clear. In literature, such behaviour was found but controversially discussed. Therefore, in this work a hypothesis was developed that is able to explain the observations made in literature as well as in the current measurements: dehydration leads not only to a decrease of proton conductivity in the membrane but also in the electrolyte phase within the catalyst layer. As a result, the protonic connection of the catalyst sites to the membrane is decreased. Especially sites with a long protonic path to the membrane are affected and might become inactive. This effectively leads to a loss in active area of the catalyst for the hydrogen oxidation reaction (as proposed by Ciureanu [16]) but would not change the active area measured during stripping voltammetry (as done by Neyerlin et al. [17]).

In order to prove if this proposed mechanism leads to the observed characteristics in the NFRA spectra, a model of the H_2/H_2 cell was developed which includes the proton transport in the catalyst layer. Thus, the model was able to reproduce and explain the main dehydration effects, which lead to the observed key features of the NFRA spectra under dehydration. The differences of the key features during CO poisoning and dehydration were analysed. Based on this comparison, a specific strategy to use these features for an unambiguous diagnosis was developed.

At the end of this work, a final resumé about the usability of NFRA for the diagnosis is drawn. Although NFRA has the potential to discriminate different critical states, the method itself uncovers practical difficulties in the determination and interpretation of the higher order frequency response functions. This makes NFRA a possible, but rather complex method for practical diagnosis.

Chapter 2

Critical States of PEMFC and Methods for their Diagnosis

As discussed in the introduction, the operation of a PEMFC is not trivial. If the cell is operated improperly, critical operation states can occur in which the cell suffers from performance loss, enhanced degradation or even damage. A review of possible critical states is given in Section 2.1. In order to avoid or react to such critical states, they have to be diagnosed clearly. Therefore, possible methods for such a diagnosis are reviewed in Section 2.2.

2.1 Critical States of PEMFCs

Critical states of PEM fuel cells can be divided into two groups: irreversible and reversible states. While reversible states lead only to temporary performance losses and can be omitted by changing the operation conditions, irreversible states leave a permanent negative impact.

Although the present work focuses on reversible critical states, the irreversible states have to be kept in mind especially during the experimental work. They have to be minimized and controlled, not only to be sure to work on well-performing cells with practical relevance but also to avoid mistaking their effects with the effect under investigation. Therefore, in the following a detailed overview of irreversible critical states will be given before the investigated reversible states are explained.

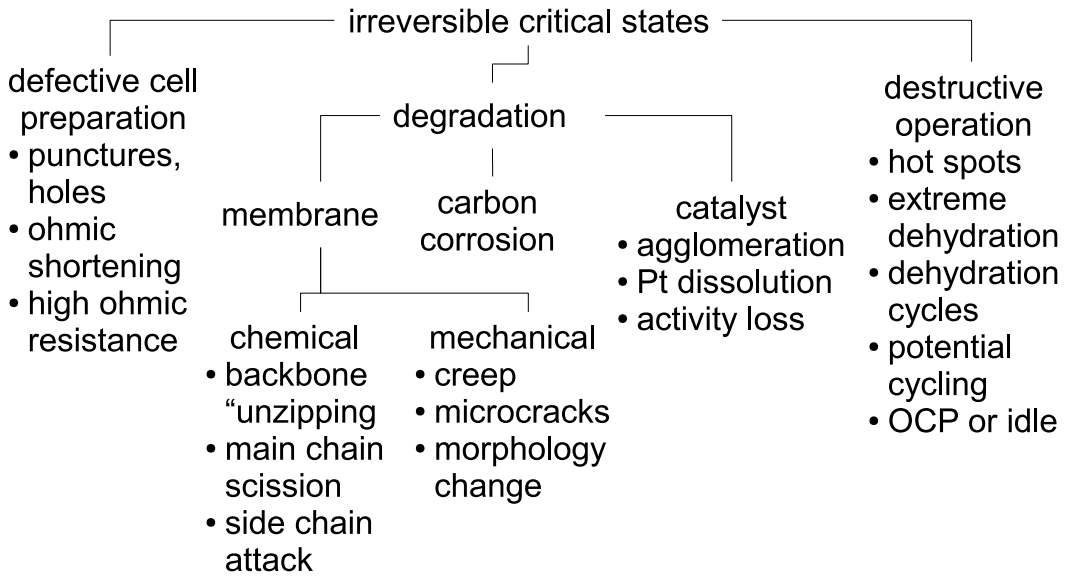

Figure 2.1: Schematic overview of irreversible critical states in PEMFCs.

2.1.1 Irreversible critical states

Irreversible critical states can result from a defective cell preparation process, degradation or irreversible destructive processes during operation. A schematic overview of irreversible critical states can be found in Figure 2.1

Defective Cell Preparation

Defects during the cell preparation process can be punctures and holes in the membrane, which lead to gas crossover. Thus, a part of the fuel can directly react with the oxidant at the catalyst surface without electrical energy being produced (e.g. [18]). A second sort of defects is ohmic shortening of the cell, e.g. by fibers from the gas diffusion layer material piercing through the membrane (e.g. [19]). Finally, after the cell preparation high ohmic resistances can occur. These can result from materials with low electronic conductivity or from high contact resistances e.g. because of low or non-uniform contact pressure or from detrimental oxide layers covering the fuel cell components (e.g. [18]).

Degradation

A further source of irreversible critical states is degradation. Mainly three types of degradation occur: membrane degradation, carbon corrosion and catalyst degradation (for survey articles see e.g. [20, 21]).

Membrane Degradation In order to understand the degradation mechanisms of the membrane, it is necessary to elucidate the chemical structure of its polymer material. State-of-the-art proton conducting polymers are perfluorosulfonic acid (PFSA) iononomers. Reviews of different types of PFSA membranes can be found in [22–26]. One of the most important PFSA ionomers is Nafion® (produced by DuPont). A review of Nafion's characteristics can be found in [27]. Nafion is a copolymer consisting of a backbone of polytetrafluoroethylene (PTFE) with sidechains formed from a perflourinated vinyl ether co-monomer:

$$\begin{array}{l}[\text{–}(\mathrm{CF_2-CF_2})_{\mathrm{x}}\text{–}(\mathrm{CF_2-CF})\text{–}]_{\mathrm{y}} \\ \qquad\qquad\qquad\qquad\quad | \\ \qquad\qquad\qquad\quad [\mathrm{O-CF_2-CF-CF_3}]_{\mathrm{m}} \\ \qquad\qquad\qquad\qquad\quad | \\ \qquad\qquad\qquad\quad \mathrm{O-[CF_2]_n\text{–}SO_3^-H^+}\end{array}$$

where $\mathrm{x}=5$–13, $\mathrm{y}\approx 1000$, $\mathrm{m}=0$–3 and $\mathrm{n}=2$–6 [23, 27].

The hydrophobic PTFE backbone ensures mechanical and chemical stability, while hydrophilic sulfonic acid end groups of the side chains make proton transport possible.

The degradation of such a Nafion membrane can be caused by chemical or mechanical degradation. The chemical decomposition mechanism of PFSA membranes is based on the attack of the polymer backbone by hydroxyl ($\bullet\mathrm{OH}$) or hydroperoxyl radicals ($\bullet\mathrm{OOH}$). Several sources of these radicals are discussed in literature [20, 21]. They can be formed either directly from oxygen-containing species on Pt (e.g. Pt-OH and Pt-OOH) [28–30] or indirectly by decomposition of intermediate hydrogen peroxide (H_2O_2).

For the latter, it is discussed that H_2O_2 might be formed either on the anode, cathode or at a Pt band formed inside the membrane by Pt dissolution and re-deposition (an issue discussed later in this chapter) [20, 21]. First, La Conti et al. [31, 32] proposed a mechanism, in which oxygen crossover to the anode side leads to the formation of

hydrogen peroxide (H_2O_2):

$$\mathrm{H_2 + 2Pt} \rightarrow \mathrm{2(Pt - H)} \tag{2.1}$$

$$\mathrm{Pt - H + O_2} \rightarrow \mathrm{\bullet OOH + Pt} \tag{2.2}$$

$$\mathrm{\bullet OOH + Pt - H} \rightarrow \mathrm{H_2O_2} \tag{2.3}$$

It is known that H_2O_2 formation is greatly enhanced in the anode potential region (≈0V vs. RHE) with a yield that can exceed 80% (in rotating disk electrode experiments with Pt/C catalyst highly dispersed on glassy carbon) [33].

For the explanation of membrane degradation in the cathode region, it has been suggested that H_2O_2 might form at the cathode by reduction of adsorbed oxygen with permeating hydrogen [34, 35].

Additionally, Ohma et al. [36] found Pt band formation in the bulk membrane in a relatively short time (several tens to a few hundreds of hours). They suggested that Pt band formation greatly enhances H_2O_2 formation, because it occurs at places where the theoretical potential profile in the membrane suddenly changes from the cathode side (≈1V vs. RHE) to the anode side (≈0V vs. RHE) and therefore meets the potential necessary for H_2O_2 formation. Additionally, since the Pt band is in the vicinity of the cathode the oxygen flux to the Pt band is much higher than to the anode side (especially under H_2/air conditions).

After its formation, H_2O_2 is assumed to decompose into hydroxy or hydroperoxy radicals on Fenton reagents (e.g. Fe^{2+}, Cu^{2+}) [31]:

$$\mathrm{H_2O_2 + M^{2+}} \rightarrow \mathrm{M^{3+} + \bullet OH + OH^-} \tag{2.4}$$

$$\mathrm{\bullet OH + H_2O_2} \rightarrow \mathrm{H_2O + \bullet OOH} \tag{2.5}$$

Directly or indirectly formed radicals primarily attack the linear polymer backbone. A mechanism that is widely agreed upon is the ”unzipping” of the polymer backbone [37, 38], beginning at incompletely fluorinated end-groups such as -COOH:

$$\mathrm{R - CF_2COOH + \bullet OH} \rightarrow \mathrm{R_CF_2 \bullet + CO_2 + H_2O} \tag{2.6}$$

$$\mathrm{R_CF_2 \bullet + \bullet\, OH} \rightarrow \mathrm{R - CF_2OH \rightarrow R - COF + HF} \tag{2.7}$$

$$\mathrm{R - COF + H_2O} \rightarrow \mathrm{R - COOH + HF} \tag{2.8}$$

Thereby, after decomposition of a complete PFSA unit into CO_2 and HF, Reaction (2.8) leaves again a -COOH end-group vulnerable for further attack.

However, attack of reactive end groups is not the only source of chemical degradation. Even if these end groups are fully fluorinated, the degradation rate can not be

reduced to zero. Durability tests of Hommura et al. [38] showed not only a decrease of the average molecular weight but also an increase of the number of -COOH groups with time. Therefore, they concluded that main-chain scission, which produces vulnerable -COOH groups, is additionally involved in the membrane degradation mechanism.

Finally, the attack of Nafion side chains by oxygen radicals is also possible [39], but occurs less prevalent during normal fuel cell operation [40].

In addition to chemical degradation, mechanical membrane degradation can occur. Membrane creep, micro-crack fractures and morphological changes are the three main issues. During normal operation, the MEA is subject to a constant compressive force between the bipolar plates. Under such stress, polymer membranes sustain time-dependent deformation, i.e. creep. This polymer creep can cause permanent membrane thinning and even failures like pinhole formation.

Additionally, micro-crack formation can occur in areas with high local stress like the edge of the flow channels, the boundary region between reaction and non-reaction zones or at ”hot spots”. Especially membrane swelling and contraction caused by changing membrane water content induces local stresses. This can lead to micro-crack formation and can also change the morphology of the polymer, leading to weak spots and tears in the membrane.

Other morphological changes are the formation and break-up of ion clusters of the functional end groups due to hydrothermal processes [41, 42]. These clusters are formed during membrane drying at elevated temperature and lead to a decrease of water uptake, conductivity and water/gas transport of the polymer [41,42]. Conversely, immersing the membrane in water of elevated temperature leads to an increase of these properties [43, 44].

Carbon Corrosion A second material in PEMFCs that is prone to degradation is carbon. It is commonly used as a catalyst support, in gas-diffusion and microporous layers and as material for bipolar plates. However, carbon is not thermodynamically stable under all conditions encountered during fuel cell operation. The general corrosion reaction of carbon material in aqueous acid electrolytes including proton exchange membranes is:

$$\mathrm{C} + 2\mathrm{H_2O} \rightarrow \mathrm{CO_2} + 4\mathrm{H^+} + 4\mathrm{e^-} \tag{2.9}$$

This reaction is enhanced with higher temperatures and a higher electrode potential. Because the operating temperature of PEMFCs is relatively low, the corrosion rate is generally slow enough to allow long-life operation. However, there are operating

conditions that lead to elevated potentials severely increasing the carbon corrosion rate. Especially at or near open circuit voltage (OCV), the potential of the cathode is relatively high (about 1V). Slightly higher potentials (about 1.1V) are reached when the cell is turned off and has air at both sides, e.g. during storage of the fuel cell. In this case, the electrodes achieve a mixed potential that is set by oxygen reduction and corrosion reactions of the components.

Even higher potentials that lead to serious carbon corrosion might be reached during start-up, shut-down or during operation with local fuel starvation areas (e.g. caused by low fuel stoichiometry or under ribs or droplets of liquid water). During start-up, the fuel flow field is usually filled up by air at first, which must be replaced by the fuel gas. This process usually takes several hundreds of milliseconds. During this transition time, the entering fuel causes the cell voltage to rise while there is still air at the exit of the fuel flow field. This voltage rise drives an ionic current through the cell at the exit location, which runs in reverse direction to the normal current flow (therefore, this mechanism is called "reverse-current mechanism") [45]. This current drives the air electrode at the exit to very high potentials ($>$1.4V), at which carbon corrosion is strongly enhanced.

The same mechanism occurs during shut-down if the fuel gas is purged out for safety reasons. When the purge gas enters the cell, there is a reverse current in the inlet region that drives the potential of the air electrode to high values resulting in enhanced carbon corrosion. In the same way, a reverse current is forced in regions where hydrogen starvation takes place, e.g. at the end of the flow channel during understoichiometric fuel supply or under ribs and even under droplets of liquid water [46].

In a fuel cell stack, fuel starvation in a single cell is a source of carbon corrosion at the anode. Due to the series connection of the cells in the stack, the same electron and proton current is flowing at every anode. In case of starvation of a single cell, this current cannot be produced from fuel oxidation. A substitutional reaction takes place, i.e. the potential of the anode shifts until O_2 evolution takes place. At this potential ($\gg$ 1.2V vs. RHE) rapid carbon corrosion takes place and can degrade the electrode within seconds [21].

Catalyst Layer Degradation The catalyst layer can be affected by various degradation mechanisms. The carbon support of the catalyst can corrode via the aforementioned carbon corrosion mechanism. This leads to detachment and loss of catalyst particles. The presence of catalyst can even increase the carbon corrosion rate (by the so-called spillover mechanism [47]). Additionally, the incomplete oxidation of carbon

can also impact the catalyst. For example, surface groups can form on the carbon (e.g. quinones, phenols, lactones [48]) and interact directly with the catalyst or indirectly via interactions with water or OH species [49]. Carbon surface groups can also change the hydrophobicity of the electrode, which can impact the access of reactants to the catalyst sites.

Additionally, the polymer electrolyte network can be attacked by the same chemical degradation mechanism as the membrane, which was described in the previous section. This leads to a decrease of the proton conductivity of the electrode.

Furthermore, the catalyst material itself can degrade. The goal of using a catalyst is to minimize the reaction overpotential. Therefore, a large electrochemically active surface area (ECSA) is necessary. To obtain a large surface area with minimal catalyst mass requires very small catalyst particles. Unfortunately, these small particles are thermodynamically less stable than larger particles. Multiple mechanisms can lead to particle growth and thus to loss in ECSA: local coalescence of agglomerated particles, agglomeration of non-adjacent crystallites via particle migration and subsequent ripening and finally dissolution of platinum and subsequent re-precipitation.

Such platinum dissolution takes place in acid electrolyte at potentials between 1 and 1.25 V vs. RHE at 25 °C [50], which occur especially at the cathode under "idling" conditions. Potential cycling, e.g. caused by varying load, leads to even higher dissolution rates than potentiostatic operation at similar potentials [51–53]. Platinum dissolution causes ECSA loss in several ways. On the one hand, dissolved platinum can redeposit on existing catalyst particles. Since smaller particles are thermodynamically less stable, they will dissolve and redeposit on larger particles. This leads to a growth of the larger particles and vanishing of the small particle fraction - an effect called Ostwald ripening. On the other hand, dissolved platinum may diffuse and redeposit into electrochemically inaccessible portions of the membrane-electrode assembly (MEA), i.e. sites not fulfilling the requirements of gas, electron and proton access.

A special form of the last mechanism mentioned above is the Pt band formation in the membrane: platinum dissolves, diffuses into the membrane and is reduced to Pt particles by dissolved hydrogen in the membrane near the cathode-membrane interface. As mentioned before, this Pt band is a possible source of H_2O_2 production in the chemical membrane degradation mechanism (Equation 2.5–2.8).

In addition to loss of ECSA, changes in the surface composition of the catalyst can decrease its inherent activity. Especially in alloy catalysts, the surface composition can change in time as the particles grow or rearrange to lower energy states. In pure platinum, common surface changes that might lower the activity are chemisorption,

place exchange reactions or platinum oxide formation [54].

Destructive Processes

This section focusses on critical states that lead to fast and irreversible destruction or degradation of the cell or its vital components. The main issues are cell reversal, extreme dehydration and hot spots. As explained before, cell reversal occurs in a fuel cell stack as a result of fuel starvation. It leads to enhanced carbon corrosion, especially of the anode catalyst support and can degrade the anode catalyst layer within seconds.

Extreme dehydration has been mentioned in the previous Section "Membrane Degradation". Especially at high temperatures, strong dehydration of the ionomer leads to the formation of ion clusters and thus to a decrease of the water uptake, conductivity and water/gas transport properties of the polymer. This process can be reversed by immersing the membrane in hot water, e.g. by boiling, but this procedure is not practically possible with a built-in MEA. Thus, extreme dehydration does not destroy the cell but leads to an irreversible performance loss. Additionally, low humidification conditions enhances the membrane degradation [55].

Hot spots can be caused by high local electrical current densities. A local increase of the current density can be the result of a non-uniform current distribution. This can be caused by an inhomogeneous fuel or oxidant distribution. Furthermore, the electrolyte conductivity can be non-uniform because of distributed water content or changing thickness of the membrane (e.g. as a result of degradation or the preparation process). Finally, non-uniform contact resistances caused by inhomogeneous contact pressure are an additional source of inhomogeneous current distribution.

Hot spots can also occur when fuel is oxidised chemically instead of electrochemically. This can be a result of severe gas crossover (e.g. at locations with a very thin membrane caused by chemical or mechanical degradation) or holes in the membrane. Thus, fuel and oxidant can react directly with each other at the catalyst. Such direct reaction produces heat, which is not only lost as electrical energy but can even burn the MEA.

2.1.2 Reversible critical states

The most important reversible critical states occuring in PEM fuel cells are dehydration and flooding (i.e. problems of water management) as well as poisoning of the anode catalyst with carbon monoxide. A schematic overview of reversible critical states can

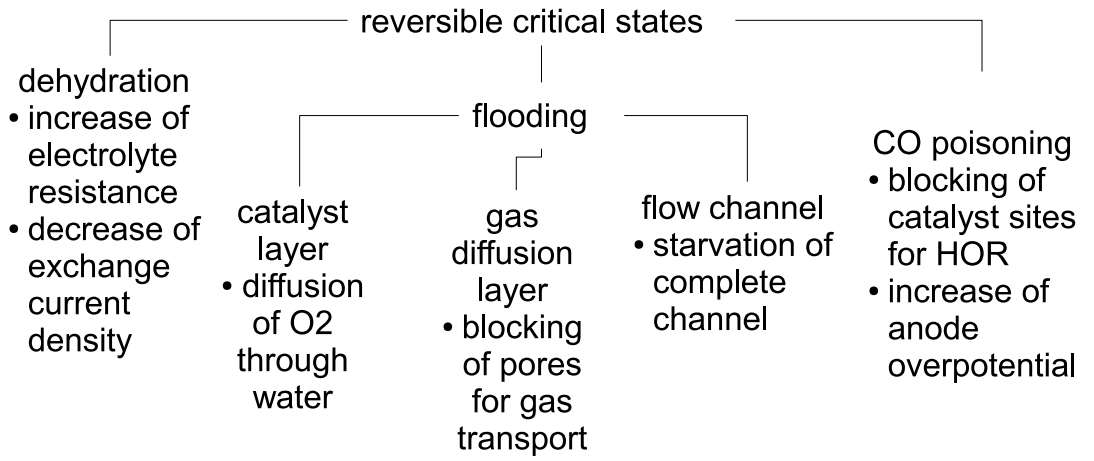

Figure 2.2: Schematic overview of reversible critical states in PEMFCs.

be found in Figure 2.2.

Dehydration

An inevitable source of performance loss in a PEMFC is the electrolyte resistance resulting from finite proton conductivity. In current polymer electrolytes, proton conductivity depends on the water content of the membrane, which is dependent on the humidification of the gases and the rate of water production. Therefore, proper water management is necessary, otherwise dehydration of the polymer electrolyte leads to an increased electrolyte resistance and thus to increased losses. In order to elucidate the relationship of humidification and proton conductivity, it is necessary to understand the structure of the polymer electrolyte (i.e. Nafion), the mechanisms of proton conduction and the role of water within these mechanisms.

The chemical structure of Nafion has been described in detail in Chapter 2.1.1, paragraph “Membrane Degradation”. It consists of a hydrophobic polymer backbone with side chains ending in hydrophilic sulfonic acid end-groups. Properly humidified, the sulfonic acid dissociates into SO_3^- groups which are fixed to the polymer backbone and into mobile, solvated protons. Hydrophilic ionic clusters are formed from solvated SO_3^-, water and protons (or some other counter-ions like Na^+, K^+ etc. depending on pretreatment). These clusters are connected by short and narrow channels.

A widely known model of the nature and geometry of these clusters is that of Gierke et al. [24, 56, 57], who proposed an inverted micellar structure with spherical clusters interconnected by cylindrical pores. A different concept is that of Yeager and Steck [58], who proposed a three-phase model in which the ionic clusters do not have a strict geometric definition. Additionally, they proposed a transition region between hydrophilic and hydrophobic regions because of the side chain architecture of Nafion. This transition region swells with increasing hydration (observed by SAXS studies [59]) indicating side chain unfolding (an idea supported by electronic structure calculations [60]). Beside these two important models, a large number of publications on this topic exist but no single view on the structure of Nafion membranes has been established yet.

Whatever the true structure of Nafion is, within this structure there is water in two different environments: surface water and bulk water [61]. A certain amount of water is needed for the solvation of the SO_3^- end groups and is therefore bound to the inner surface of the ionic clusters. Water that is additionally taken up fills the volume of pores and channels and acts bulk-like.

Proton transport in Nafion membranes can be categorised into different mechanisms (for reviews of proton transport mechanisms see [61, 62]): direct proton transport between vibrating polymer side chains (without water being involved), the Grotthus mechanism (a proton hopping mechanism, also called structural diffusion) and the vehicle-mechanism . The latter is the diffusion of protons on a vehicle, e.g. as H_3O^+ ions, in a Zundel ion $H_5O_2^+$ with a symmetric positioning of the proton between two water molecules or as an Eigen ion $H_9O_4^+$ with a H_3O^+ ion hydrated by three water molecules.

The proton conductivity results from the combination of these structural and kinetic characteristics of the membrane. Macroscopically, the proton conductivity increases approximately linear with water content [41, 63]. Thereby, the water content is determined by the relative humidity of the fuel gases via a phase equilibrium. Up to a relative humidity (rh) of 75% rh the membrane water content increases only weakly from 2 to 6 mol of H_2O per mol SO_3H but then a strong increase up to 14 $\mathrm{mol_{H_2O}/mol_{SO_3H}}$ at 100% rh follows [41]. This results in a highly nonlinear dependency of proton conductivity on humidification, which approximately follows an exponential function [64].

As a result, insufficient humidification of the gases can lead to a strongly decreased electrolyte conductivity. This can lead to three kinds of losses [65]: first, the membrane resistance increases leading to larger ohmic losses. Second, the resistance of the ionomeric component in the catalyst layer increases. Third, a loss in oxygen reduction reaction (ORR) kinetics has been found [65, 66].

Different possible explanations for the latter observation can be found in literature. Uribe et al. [66] suggest that loss of ORR activity may be caused by ionomer surface restructuring where the hydrophobic component of the ionomer comes into contact with the Pt surface at a low ionomer water content. This interfacial configuration leads to poor ORR reactivity. Alternatively, Xu et al. [67] suggested that a decrease in relative humidity would lead to a decrease in proton and/or water activity, leading to an increase in the cathode overpotential. However, the authors did not account for the potential drop in the electrolyte phase of the catalyst layer, which brought Neyerlin et al. [17] to a more detailed analysis. They concluded that the decrease of the exchange current density of ORR by a factor of 2 is most likely due to a lowering of the proton activity. A third explanation for the lowering of the ORR kinetics was given by Ciureanu [16], who investigated electrochemical impedance spectra (EIS) under dehydration. Ciureanu concluded that the observed activity decrease of the cathode may in principle be due to a decrease in the intrinsic activity i^0 of the cathode or a decrease in the electrocatalytically active surface area S_{act}, according to:

$$i^0_{apparent} \quad = \quad i^0 \cdot S_{act} \tag{2.10}$$

Bode plots (phase angle of the impedance vs. frequency) helped to decide between these two options: while a change in i^0 would lead to a change in the phase angle, a change of S_{act} would affect only the magnitude but not the phase angle of the impedance (because real and imaginary part of the impedance would be affected in the same proportion). The latter effect was visible in Ciureanu's measurements, ergo it was concluded that a decrease of humidification leads to a decreased ECSA caused by dehydration of the Nafion's pathways for protons in the catalyst layer, which is equivalent with the disappearance of part of the active sites.

Flooding

The formation of excess liquid water (so-called flooding) can be a source of performance loss in a PEMFC. Several comprehensive review articles on this topic can be found in literature [68–71], therefore only the most important points will be summarised in the following. Liquid water occurs as a result of an improper balance between: 1. the water transported into and out of the cell by the reactant gas streams, 2. water generated at the cathode by the electrochemical reaction, 3. water transported through the membrane by electro-osmosis, back-diffusion, pressure driven hydraulic permeation [71] or thermal-osmotic drag [72, 73]. Because of the water production

and the electro-osmotic drag of water to the cathode, flooding mainly occurs at high current densities at the cathode side, although at low current densities flooding of the anode is possible, too [69].

In the catalyst layer, liquid water can fill the pores and block the active sites from direct contact with the fuel or oxidant gas. Thus, the gases can reach these sites only by dissolution and diffusion through the covering water film, which hinders mass transport dramatically.

In the GDL, liquid water fills the hydrophilic part of the pore network, making it impassable for gas transport. However, due to impregnation with hydrophobic material (usually PTFE) a part of the pore structure repels liquid water and ensures gas transport at least to some extend. On the contrary, the hydrophilic part of the pore network wicks the liquid water out of the catalyst layer and transports it into the flow channel via capillary transport. In the flow channel, liquid water can be transported out of the cell by the gas streams. However, if too much water accumulates in the flow field, complete channels can be blocked by liquid water (especially in parallel flow fields) and transport of reactant gases into these channels is hindered.

Flooding results in a performance loss mostly attributable to the greatly reduced oxygen transport rate at high current densities, where the water generation rate exceeds the water removal rate. This becomes visible as a steep decrease in the polarization curve at high current densities (e.g. see Figure 2 in [68]). In case flooding leads to complete oxygen starvation (e.g. in a blocked channel or in a blocked single cell within a stack), the oxygen reduction reaction would be replaced by the proton reduction reaction (i.e. hydrogen evolution):

$$2\mathrm{H_3O^+} + 2\mathrm{e^-} \quad = \quad \mathrm{H_2} + 2\mathrm{H_2O} \qquad (\mathrm{E^0} = 0.00\mathrm{V}) \tag{2.11}$$

In this case, the cathode potential shifts towards the negative direction. This leads to a smaller cell voltage in case of partial oxygen starvation. In case of starvation of a complete cell (e.g. within a stack), the result is a negative cell voltage (≈ -0.2V), i.e. cell voltage reversal. Note, that in contrast to cell voltage reversal by fuel starvation as described in Section 2.1.1, oxygen starvation does not lead to enhanced carbon corrosion (both electrodes are at low potentials). Nevertheless, it seriously impairs the stack performance.

An additional transient effect is oscillation-like behaviour of the cell voltage during galvanostatic operation [68, 69, 74]. In this case, liquid water accumulates until severe flooding occurs and the gas flow path becomes temporarily blocked. Thus, the cell voltage drops in form of a negative spike. The blocking of the gas flow path leads to a

sudden build-up of local pressure, which then flushes out the liquid water and restores the cell voltage again. Thus, periodic build-up and removal of liquid water causes typical cell voltage patterns.

Catalyst poisoning

Contaminants are a further source of performance loss in a PEMFC. An overview of contaminant sources, their impact, poisoning mechanisms and mitigation strategies can be found in [75]. One of the most relevant contaminants is carbon monoxide. It is a side product of the industrial production of hydrogen via the reforming of hydrocarbons, such as methane or hydrocarbons from renewable sources like biogas, methanol, ethanol or biomass. Due to preferential adsorption on the one hand and reduction of catalytic activity on the other hand, CO is a strong catalyst poison (e.g. [76]). Even trace amounts of 5-50 ppm are sufficient to cause large anodic overpotentials reducing the cell voltage dramatically (e.g. [77]). A comprehensive review of carbon monoxide poisoning was given by Baschuk and Li [78], therefore only a short summary will be given in the following.

Carbon monoxide chemisorbs preferentially on the Pt catalyst sites to the exclusion of hydrogen [79, 80]. This is because CO has a more negative free Gibbs energy of adsorption and is more strongly bonded to Pt (indicated by a greater oxidation potential) with a 15 times higher sticking probability [79].

Additionally, CO poisons the electrode not only by site exclusion but reduces the catalytic activity of unoccupied catalyst sites for hydrogen oxidation [81–83]. Several suggestions for an explanation of this behaviour can be found in literature. Dhar et al. [82] suggested that either CO preferentially adsorbs to the “best” sites for hydrogen oxidation or that hydrogen is involved in the CO adsorption process. On the contrary, Springer et al. [83] assumed that an adsorbed CO molecule affects the rate of dissociative adsorption of hydrogen at a number of CO-free adjacent sites.

There are two main mitigation strategies for CO poisoning. First, oxygen or air can be mixed into the CO-containing fuel gas (so-called “air bleed”) [84]. Thus, CO is chemically oxidised into CO_2 at the catalyst (without producing electrical energy). An indirect method of introducing oxygen into the fuel gas is the injection of hydrogen peroxide [85]. H_2O_2 decomposes at the catalyst and oxidises CO without the safety issues associated with mixing hydrogen and oxygen gas [86]. The disadvantage of air-bleed is that a part of the fuel gas is oxidised chemically, too.

A second strategy is the development of catalysts which are more CO tolerant.Alloys

with a second metal (Ru, Sn, Co, Cr, Fe, Ni, Pd, Os, Mo, Mn, etc.) or even ternary or quaternary alloys are very popular. More details on this topic can be found in [87]. Two main models were proposed to explain the positive effect of alloying: a bifunctional model involving a promotion mechanism and an electronic model dealing with an intrinsic mechanism [75]. On the one hand, the bifunctional mechanism suggests an improved water activation reaction on the second alloying metal which enhances the electrochemical oxidation of CO:

$$\mathrm{M} + \mathrm{H_2O} \rightarrow \mathrm{M-OH} + \mathrm{H^+} + \mathrm{e^-} \tag{2.12}$$

$$\mathrm{Pt-CO} + \mathrm{M-OH} \rightarrow \mathrm{Pt} + \mathrm{M} + \mathrm{CO_2} + \mathrm{H^+} + \mathrm{e^-} \tag{2.13}$$

This mechanism was supported by CO stripping [88] and rotating disc electrode (RDE) experiments [89–91].

On the other hand, the intrinsic mechanism suggests that alloying decreases the stability of the CO bond to the catalyst surface more than that of H by modifying the electronic properties of the pure Pt. This mechanism was confirmed by experimental studies on PtRu [92, 93] as well as by density functional calculations and Monte Carlo simulations for $Pt_{0.5}Ru_{0.5}$ [94].

The development of catalysts with improved CO oxidation resulted in the suggestion of a PEMFC-like reactor for deep CO removal from fuel gas based on the electrochemical preferential oxidation (ECPrOx) of CO [95, 96]. During galvanostatic operation of such a reactor, autonomous potential oscillations occur which greatly enhance CO oxidation [97–100]. These oscillations consist of a CO adsorption phase followed by a CO oxidation phase [95] forming a cyclic self cleaning process of the anode. Note that in such an ECPrOx reactor the energy of CO oxidation and undesired H oxidation is partly converted into electrical energy, as opposed to chemical oxidation (e.g. during air bleed or preferential oxidation).

2.2 Methods for Diagnosis

As explained before, this work focusses on the diagnosis of reversible critical states. In the previous section it has been discussed that the most important reversible criticals states are dehydration, flooding and CO poisoning. Therefore, in this section methods for the diagnosis of those states are briefly reviewed. In literature, comprehensive reviews of diagnostic tools for PEM fuel cells can be found (divided into electrochemical [101] and physical or chemical methods [102] or focussing on different length

scales [103]). In the current work, the focus is on methods with practical applicability, i.e. methods that are applicable in-situ and non-intrusive.

In the following, at first methods for the diagnosis of water management issues, i.e. dehydration and flooding, are discussed (Section 2.2.1). Second, methods for CO poisoning diagnosis are explained (Section 2.2.2). Finally, conclusions for practical application and suitability of the reviewed methods are drawn (Section 2.2.3).

2.2.1 Diagnosis of Water Management Issues

A variety of measuring techniques related to water management can be found in literature (for reviews see [62, 68–70] and for reviews focussing on liquid water see [104, 105]). From these techniques, intrusive methods using modified cells (first paragraph) and intricate non-intrusive methods (second paragraph) are less suitable for practical application in the field of diagnosis but might be usefull for reference measurements. In the last paragraph non-intrusive in-situ methods which are more practice-oriented are discussed.

Intrusive Methods Using Modified Cells

A straightforward approach to gain insight into liquid water distribution inside a PEMFC is direct visualisation. With this approach, a transparent cell plate allows access to the channels for optical devices such as digital camcorders and high-speed cameras [106, 107], infrared cameras [108] or CCD cameras [109–112]. These techniques provide a high temporal and spatial resolution. With this, water transport was investigated in the flow channels [106–108, 113–124], GDL pores [111, 112, 125–131] and on the micro-scale of the catalyst surface [106]. The effect of the operating conditions on water droplet formation, growth and movement were investigated [107, 115, 121, 125, 126] and different flow patterns have been classified [109, 119].

Additional techniques for direct measurement of water content are based on adsorption spectroscopy. The groups around Basu, Renfro and Cetegen et al. [132–137] developed a tunable laser diode measurement system to measure the water vapour concentration in the gas channel spatially resolved under steady state and dynamic conditions. Fushinobu et al. [138] developed an infrared transmission measurement technique for the measurement of membrane water content. Morita et al. [139] used a near-infrared laser sheet beam to measure the two-dimensional in-plane distribution of water in the membrane.

In situ water vapour distribution can also be measured using gas extracting systems in combination with gas chromatography [140] or mass spectrometry [141–143]. A review of techniques and concepts for local online gas analysis can be found in [143]. With these techniques, local species concentrations can be measured along the channel. Additionally, by use of tracer gases the through-plane permeation and in-plane gas diffusion layer permeation can be measured. Thus, conclusions about local liquid water distribution can be drawn [143].

A further approach for the measurement of local humidity is the integration of humidity sensors into the cell [144,145]. In the same way, David et al. [146] introduced optical fibre sensors for simultaneous measurement of local temperature and relative humidity. Herrera et al. [147] placed sensing electrodes into the cell for the diagnosis of flooding, dehydration and low fuel stoichiometry.

With the measurement of current density distribution, conclusions about local flooding or dehydration can be drawn. This is possible using segmented cells, a technique introduced by Cleghorn et al. [148]. Three main types of segmented cells are used based on printed circuit boards, resistor networks and Hall effect sensors. Recently, a comprehensive literature review on these approaches was given by Pérez et al. [149] and is therefore not repeated here.

Intricate Non-Intrusive Methods

In addition to the segmented cell approach, it is possible to measure the current density distribution non-invasively by sophisticated magnetic field measurement devices [102, 149]. Claycomb et al. [150] used high and low temperature superconducting (HTS and LTS, respectively) quantum interference devices (SQUID) and flux gate magnetometers to obtain spatial magnetic field maps of an operating PEMFC. Candusso et al. [151] used SQUID in combination with magnetoresistive sensors. Hauer et al. [152] introduced a magnetic induction tomography technique to indirectly measure the 3D current density distribution of the cell.

An elaborate method for direct visualisation of water in a PEMFC is nuclear magnetic resonance imaging (NMR) (also known as magnetic resonance imaging, MRI). With this method, the PEMFC is put into a static magnetic field and excited with a radio frequency signal. Thus, specific atomic nuclei with non-zero spin moments such as ^{1}H are excited to higher energy levels. Relaxation of these excited atoms emits a characteristic radio-frequency signal. The amplitude of this signal is proportional to the number of water molecules in the cell. Frequency and phase of the signal are used

to encode spatial information [105]. With this technique, Tsushima et al. investigated the spatial distribution of water in through-plane direction of the membrane depending on operating conditions [153–155], membrane thickness [156], varying membrane materials [154, 157, 158] and liquid water supply [154]. The group of Feindel et al. used NMR to measure the water distribution in in-plane direction [159–162] and demonstrated that hydrogen-deuterium exchange can be used to increase the contrast [163]. Minard et al. [164] used NMR in the in-plane direction and observed the formation and slow propagation of a dehydration front from the gas inlet to the outlet. However, drawbacks of NMR are the limited temporal resolution (50 s [105, 153]), limited in-plane spatial resolution (25 μm [105, 153]), limited sensing volume (cells of 0.5-2 cm^2 active area [105]) and the invasiveness due to necessary changes in the fuel cell materials (e.g. non-magnetic current collectors). Additionally, water content is difficult to measure in the GDL due to negative effects of magnetic susceptibility differences, electrical conductivity and the paramagnetic nature of the GDL materials on the signal [162].

Beam interrogation techniques are another principle to detect liquid water in fuel cells. Mainly X-rays and neutron beams are used to visualise liquid water. X-rays are used in two configurations, either measuring the beam deflection by diffraction or measuring the beam attenuation [105]. In both cases the measured transmitted beam amplitude is proportional to the water content. Especially with the use of synchrotron radiation, high spatial resolutions (3-7 μm [165]) coupled with high signal to noise ratios [166] are possible. Albertini et al. reported the first X-ray diffraction experiments of membrane dehydration [166] and real time changes of water content using energy dispersive X-ray diffraction [167]. X-ray microtomography [168, 169] and synchrotron X-ray radiography [165, 170, 171] were used to measure liquid water saturation distribution [165, 168, 170] and liquid water accumulation [169, 171].

Neutron imaging has developed significantly in the last years. Neutrons are sensitive to hydrogen-containing compounds such as water while being relatively insensitive to common fuel cell materials (e.g. aluminium, graphite). This makes neutron imaging an ideal, non invasive method for liquid water visualisation in all dimensions. Thus, the development of this method has lead to ever increasing spatial and temporal resolutions [172]. The main disadvantage is the necessity of a high intensity thermal neutron source, which is only available at a few institutions worldwide [104]. Bellows et al. [173] were the first to use neutron imaging to determine water distribution inside a PEMFC. Further works have recently been reviewed by Mukundan and Borup [172] in a paper focussing especially on visualising liquid water using neutron

imaging. For further information, additional review aricles can be found in abundance in literature [68, 69, 101, 104, 105].

Non-Intrusive In-situ Methods

A common and simple technique for fuel cell characterisation is the measurement of polarisation curves (i.e. measurement of cell voltage vs. current) [101]. They are useful indicators for the performance of the cell (or stack) as a whole under specific operating conditions. However, they fail to obtain detailed information about individual components of the cell, are incapable of resolving time dependent processes and cannot be used to differentiate different mechanisms from each other.

However, the hysteresis of a polarisation curve recorded subsequently both in increasing and decreasing current density direction can be used as an indicator for flooding or dehydration [70, 174]. When the backward curve shows lower voltages than the curve recorded with increasing current, this indicates flooding. This is because during the forward scan more and more liquid water is produced and thus flooding is enhanced. Conversely, if the backward scan shows higher voltages, the cell was dehydrated and the increased water production during the forward scan leads to increased cell voltage in the backward scan.

An additional technique in combination with polarisation curve measurement is the exchange of the cathode gas. Comparison of polarisation curves recorded during operation with air and pure oxygen can be used to characterise mass transfer limitations on the cathode (e.g. due to liquid water) [175–177]. Ralph et al. [176] used air, pure oxygen and helox (mixture of 79% helium and 21% oxygen, in which oxygen diffusion is easier than in air, thus reducing mass transport losses) to characterise losses associated with oxygen gas diffusion (comparison of air and helox operation) and oxygen permeability (comparison of helox and pure oxygen operation).

Because polarisation curve measurements are time consuming, dehydration is usually detected by an increase of the membrane resistance. The membrane resistance can be measured with an electrical excitation of the cell. On the one hand, current steps in form of current pulses [178–180] or current interruption [181–184] can be used to determine the ohmic resistance of the cell. The principle of this technique is that after a current step the ohmic voltage drop has a much faster relaxation time than the electrochemical overpotential. Thus, the ohmic resistance can be determined from the voltage before and directly after the current step according to $R_\Omega = \Delta U / \Delta I$. In order to obtain accurate results, the current step has to be very sharp. Therefore, Büchi et

al. [178–180] designed a current pulse generator with a very low inductance of the current pulse path which resulted in very fast trailing edges (decay time < 5 ns). Thus, it was possible to accurately separate the ohmic resistance from the other overpotentials at the electrochemical interface in a fuel cell under DC operation.

On the other hand, the ohmic resistance of the cell can be measured by a sinusoidal electrical perturbation. Therefore, a sinusoidal signal (current or voltage) of small amplitude and high frequency (usually 1kHz) is superimposed to the DC operating point. This is done either by controlling the load itself (this is called high frequency resistance (HFR) method and is a sub-method of the electrochemical impedance spectroscopy explained later in this section) [185] or by using an external AC milliohm meter in parallel to the load (this is called high frequency milliohm meter (HFM) method or AC resistance method) [185, 186]. The latter method has an easier instrumentation setup, but has the disadvantage of measuring both the cell and load resistance in parallel, which makes it necessary to measure the impedance of the load separately and can lead to considerable errors due to interferences of load and milliohm meter.

Flooding itself can be detected by pressure drop measurements [70, 102, 105], because liquid water increases the gas flow resistance in the cell. For example, Barbir et al. [187] and He et al. [188] used pressure drop in cells with interdigitated flow fields as diagnostic tool for liquid water, which strongly decreases the gas permeability in the porous electrodes. Liu et al. [113, 114] studied the influence of operating parameters and defined a parameter assessing the channel flooding rate as a function of the pressure drop. General Motors patented a method and apparatus for flooding detection and correction based on pressure drop monitoring [189].

Stumper et al. [190] developed an in-situ cathode discharge method (i.e. galvanostatic cell discharge with interrupted reactant supply) as a diagnostic tool to determine ohmic resistance, effective diffusivity and the free gas volume of the fuel cell. The ohmic resistance enables the determination of the membrane water content, whereas the free gas volume measurement makes it possible to deduce the amount of liquid water. Combination of the discharge method with a current mapping approach allowed to measure the membrane resistance locally resolved.

Electrochemical impedance spectroscopy (EIS) is a well established method for the diagnosis of critical states in fuel cells [65, 191–194]. This method is based on a small sinusoidal perturbation of the electrochemical system (either in current or voltage) and measuring the response signal. Because of the small amplitude of the perturbation, the system is assumed to be linear in the range of the perturbation and the linear impedance is analysed. Due to the variation of the perturbation frequency, processes

with different time constants can be separated. For example, the high frequency end of the impedance spectra provides the ohmic resistance of the cell, from which the change of the membrane resistance due to dehydration can be deduced. Thus, EIS has been applied for the analysis and diagnosis of dehydration and flooding [16, 184, 195–199].

2.2.2 Diagnosis of CO Poisoning

Usually ceramic sensors [200–202] or miniature PEMFC-type sensors [203–206] are used for the detection of CO. For fuel cell diagnosis, they can be placed in the gas streams before they enter the fuel cell.

Polarisation curve measurements as explained in the previous chapter can also be used as an indicator for CO poisoning. Polarisation curves in potentiostatic operation under CO poisoning show typical S-shape profiles [207, 208], which have especially been discussed by Camara et al. [209] and Lopes et al. [210]. In galvanostatic operation, the polarisation curve is identical until higher overpotentials are reached at which oscillations might occur, as explained in Section 2.1.2. These features can be used as indicators for CO poisoning.

CO stripping voltammetry, i.e. a variant of the well established cyclic voltammetry [211], is another common technique for the diagnosis of fuel cells [101]. It is used to measure the electrochemically active surface area [101] or explore the reaction mechanism at catalyst alloys [88–90]. Additionally, Brett et al. [212] used CO stripping voltammetry in a segmented cell to investigate the local CO concentration distribution at varying gas flow rates.

Electrochemical impedance spectroscopy, as explained in the last section, has also been widely used for the analysis and diagnosis of CO poisoning in PEMFCs [13, 199, 213–215]. It can be appliead easily in situ, non-intrusively and during operation and allows the separation of processes with different time constants.

2.2.3 Conclusions

In literature, there are numerous methods available for the analysis of dehydration, flooding and CO poisoning. However, for a practical application, non-invasive in-situ methods without the necessity of special cell designs are preferred. Intricate methods as described above are useful tools for basic research and reference measurements but are not suitable for wide commercialisation because of their cost and complexity. Additionally, an ideal method should not interrupt the operation.

Techniques that fulfil these requirements are pressure drop monitoring for the diagnosis of flooding, high frequency resistance measurement or the high frequency milliohm metre method for dehydration, external sensors for CO and electrochemical impedance spectroscopy for the diagnosis of all three critical states. Therefore, EIS is the most favourable method for the simultaneous diagnosis of flooding, dehydration and CO poisoning. Otherwise, a combination of different methods would be necessary which would require numerous external measurement devices. On the contrary, EIS uses the electrical behaviour for diagnosis, which is easily accessible for in-situ measurement. For example, it can be easily implemented into power electronics like DC/DC or DC/AC converters [216].

Nevertheless, some deficiencies of EIS have been found. Under certain operating conditions, impedance spectra for different processes can be similar, like for flooding and CO poisoning [199] or for dehydration and flooding [217] as will be shown in Chapter 5. This similarity of the spectra is the case if the processes have similar time constants and therefore are measured in the same frequency range. Additionally, a masking effect due to the high double layer capacity can occur. This makes it impossible, e.g. to distinguish between thin film diffusion and agglomerate diffusion of oxygen at the cathode [218, 219]. Another drawback of EIS is that for the complete characterisation of the nonlinear fuel cell behaviour multiple impedance spectra at various working points would be necessary.

Chapter 3

Nonlinear Frequency Response Analysis

In this chapter, the method of nonlinear frequency response analysis is explained in detail. NFRA is a nonlinear electrochemical method based on sinusoidal electrical perturbation. Therefore, a literature review of such methods is of interest and is provided in Section 3.1. In this review, the advantages and disadvantages of NFRA in comparison to other methods are discussed. Afterwards, in Section 3.2 the principle and mathematical background of NFRA is explained. With this, it is possible to derive NFRA spectra analytically from model equations. This will be explained in Section 3.3 and demonstrated using a simple electrical model system. Additionally, the NFRA spectra can be determined from measured or numerically simulated data, which will be explained and exemplarily demonstrated in Section 3.4.

3.1 Nonlinear Electrochemical Methods

A variety of nonlinear electrochemical methods using sinusoidal perturbation was established during the last decades. These can be divided into two classes. The first class is referred to as high amplitude AC voltammetry. It has been developed independently by Engblom et al. [220] and Gavaghan and Bond [221]. It extends the second order AC voltammetry which was developed by Smith in the 1960s [222]. In this technique, a sinusoidal potential of a single frequency and elevated amplitude is superimposed onto the linear or cyclic voltage sweep used in classic voltammetry.

The second class of nonlinear methods is based on high amplitude sinusoidal perturbation of the system around one steady operating point. If this perturbation is

applied to nonlinear electrochemical systems, the output signal is characterised by a DC rectification signal and the occurrence of higher harmonics. This second class of nonlinear methods can be divided into three subcategories: (1) methods dealing with the DC rectification (faradaic rectification; see [223] for a review); (2) methods analysing the higher harmonics (harmonic analysis; see [223–225] for reviews), e.g. faradaic distortion, harmonic impedance spectroscopy, electrochemical frequency modulation/intermodulation voltammetry, harmonic synthesis, total harmonic distortion analysis [226,227] and nonlinear frequency response analysis [217,228]; (3) methods analysing the amplitude dependence of the fundamental harmonics (nonlinear EIS, suggested by Darowicki [229–231]).

Among these methods, nonlinear frequency response analysis (NFRA) is highly suitable for the analysis of PEM fuel cells because it is not tailored to one special model or mechanism but allows the analysis of complex models and mechanisms. Additionally, with NFRA analytical solutions of modeled spectra are possible [228]. Thus, problems with the numerical treatment, e.g. long computing times, numerical errors, solver problems etc., can be avoided.

3.2 Principle of the NFRA Method

NFRA uses a sinusoidal input signal with a moderately increased amplitude. Thus, the system can no longer be assumed to be linear around the working point but nonlinear distortions occur. These distortions can be analysed with a mathematical framework of Fourier transform from which Volterra series approximation and so called higher order frequency response functions (HFRF) are obtained. Thereby, the HFRF of first order is identical to the EIS spectrum and describes the linear behavior of the system around the working point. Additionally, HFRF of higher order contain information about the nonlinearities of the system. NFRA has been developed in the 1980 for the analysis of analogue electrical circuits [232] and successfully used for the investigation of adsorption systems (see [233] for a review) and methanol oxidation kinetics [228]. One important result was the possibility to discriminate between different adsorption kinetic mechanisms [233, 234] and different methanol oxidation kinetics [228] based on the shape of the second order frequency response functions.

In the following, the generic mathematical background of NFRA is explained. This concept can be applied to any weakly nonlinear system with a polynomial nonlinearity. Other systems can be transformed into polynom form by Taylor series expansion, as

explained later in this chapter. The response $y(t)$ of a nonlinear system with polynomial nonlinearity to any input $x(t)$ can be represented by the Volterra series [235]:

$$y(t) = \sum_{n=1}^{\infty} \underbrace{\int_{-\infty}^{\infty} \cdots \int_{-\infty}^{\infty}}_{n-fold} h_n(\tau_1, \ldots, \tau_n) x(t-\tau_1) x(t-\tau_n) d\tau_1 \ldots d\tau_n \tag{3.1}$$

In this equation, the function $h_n(\tau_1, \ldots, \tau_n)$ is the generalised impulse response function of order n, also known as the n-th order Volterra kernel. If the input $x(t)$ to the nonlinear system is a single harmonic function of the form:

$$x(t) = A\cos(\omega t) = \frac{A}{2} e^{j\omega t} + \frac{A}{2} e^{-j\omega t} \tag{3.2}$$

the output signal can be described as:

$$\begin{aligned} y(t) = & \sum_{n=1}^{\infty} \left(\frac{A}{2}\right)^n \underbrace{\int_{-\infty}^{\infty} \cdots \int_{-\infty}^{\infty}}_{n-fold} h_n(\tau_1, \ldots, \tau_n) \cdot (e^{j\omega(t-\tau_1)} + e^{-j\omega(t-\tau_1)}) \cdots \\ & (e^{j\omega(t-\tau_n)} + e^{-j\omega(t-\tau_n)}) d\tau_1 \ldots d\tau_n \end{aligned} \tag{3.3}$$

The application of the n-dimensional Fourier transform to this function provides the higher (n-th) order frequency response function (FRF) $H_n(\omega_1, \ldots, \omega_n)$ [232]:

$$H_n(\omega_1, \ldots, \omega_n) = \underbrace{\int_{-\infty}^{\infty} \cdots \int_{-\infty}^{\infty}}_{n-fold} h_n(\tau_1, \ldots, \tau_n) e^{-j(\omega_1\tau_1 + \ldots + \omega_n\tau_n)} d\tau_1 \ldots d\tau_n \tag{3.4}$$

With this, the first three elements of the Volterra series (Equation 3.1) are as follows:

$$\begin{aligned} y(t) = & \left(\frac{A}{2}\right) e^{j\omega t} H_1(\omega) + \left(\frac{A}{2}\right) e^{-j\omega t} H_1(-\omega) + \\ & \left(\frac{A}{2}\right)^2 e^{2j\omega t} H_2(\omega, \omega) + 2\left(\frac{A}{2}\right)^2 e^{0} H_2(\omega, -\omega) + \\ & \left(\frac{A}{2}\right)^2 e^{-2j\omega t} H_2(-\omega, -\omega) + \\ & \left(\frac{A}{2}\right)^3 e^{3j\omega t} H_3(\omega, \omega, \omega) + 3\left(\frac{A}{2}\right)^3 e^{j\omega t} H_3(\omega, \omega, -\omega) + \\ & 3\left(\frac{A}{2}\right)^3 e^{-j\omega t} H_3(\omega, -\omega, -\omega) + \left(\frac{A}{2}\right)^3 e^{-3j\omega t} H_3(-\omega, -\omega, -\omega) \\ & + \ldots \end{aligned} \tag{3.5}$$

In this equation, h_1 is the linear impulse response function and H_1 is the linear frequency response function, which corresponds to the classic EIS spectrum. The frequency response functions of higher orders (H_2, H_3,...) contain the nonlinear fingerprint of the system and are therefore able to provide information which cannot be obtained from EIS.

Note that for reasons of readability, in the following a short notation for the HFRF is introduced: $H_{n,i}$ where n is the order of the FRF and i is the "number of negative ωs", e.g. $H_3(\omega, \omega, -\omega)$ is written as $H_{3,1}$.

With this, the Volterra series for the special harmonic input signal $x(t) = cos(\omega t)$ (Equation 3.5) can be written in a short form as [236]:

$$y(t) \;=\; \sum_{n=1}^{\infty} \sum_{i=0}^{n} \binom{n}{i} H_{n,i} \left(\frac{A}{2}\right)^n e^{j(n-2i)\omega t} \tag{3.6}$$

Furthermore, the symmetry of the FRF has to be mentioned: FRFs with the same difference of positive and negative ω's are symmetrical, i.e. $H_1(\omega)$ is symmetrical to $H_1(-\omega)$, $H_2(\omega, \omega)$ is symmetrical to $H_2(-\omega, -\omega)$ and $H_3(\omega, \omega, -\omega)$ is symmetrical to $H_3(\omega, -\omega, -\omega)$. Therefore, in the following the focus will be on only one of the symmetrical FRFs (namely the more positive ones, i.e. $H_{1,0}$, $H_{2,0}$, $H_{3,0}$, $H_{3,1}$ etc.). A specialty are the FRFs with the same number of positive and negative ωs, i.e. $H_2(\omega, -\omega)$, $H_4(\omega, \omega, -\omega, -\omega)$ etc. As explained later in Section 3.4, they form the DC part of the signal.

3.3 Analytical Derivation of Higher Order Frequency Response Functions

The mathematical framework described in the previous section can be used to derive the higher order frequency response functions analytically from mathematical model equations of the system. To do so, the following procedure as described by Bensmann et al. [228] might be used:

1. Defining the input and output variables. In this work, usually the current is used as an input and the cell voltage as output.

2. Taylor series expansion of the nonlinear terms. For the derivation of the frequency response functions, all nonlinear terms in the model equations (e.g. kinetic equations) must be of polynomial form. This can be achieved by Taylor

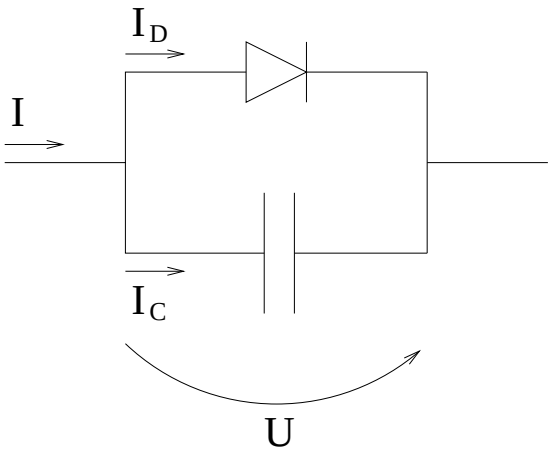

Figure 3.1: Schematic representation of the analysed electrical circuit.

series expansion of these terms around the working point. Thereby, the Taylor series should be expanded to the same order as the order of the highest HFRF that shall be derived. Higher orders of the Taylor expansion do not change the results of the obtained HFRF, but lower orders lead to approximation errors.

3. Substituting the Taylor-approximated kinetic equations into the balance equations of the model. Thus, a set of ordinary differential equations or a set of differential algebraic equations is obtained.

4. Substituting the ansatz functions of the input (Equation 3.2) and output signal (Equation 3.6) into the equations resulting from step 3.

5. Applying harmonic probing. This is done by collecting all the terms corresponding to the same order (i.e. same power of input amplitude A^n and same frequency $n\omega$) from the equations obtained from step 4. Thus, a set of linear equations corresponding to $H_{1,0}$, $H_{2,0}$ etc. is obtained.

6. Solving the set of linear equations obtained in step 5. As a result, the higher order frequency response functions are obtained as functions of the model parameters.

In the following, a simple nonlinear electrical system is used as an example to illustrate the aforementioned procedure. This system is shown in Figure 3.1 and consists of a parallel connection of a diode (i.e. a nonlinear element) and a capacitor (i.e. a dynamic element). The current flowing through the diode can be approximately described as

[237]:

$$I_D = I_r \left(e^{(\frac{U_D}{U_t})} - 1 \right) \tag{3.7}$$

where the reverse current I_r is a parameter of the diode and the thermal voltage U_t can be determined from the temperature T, Boltzmann constant k and elementary charge e according to $U_t = kT/e$.

The current through the capacitor is given by:

$$I_C = \frac{dU_C}{dt} C \tag{3.8}$$

where C is the capacity. According to Kirchhoff's first law, the overall current is:

$$I = I_C + I_D = I_r \left(e^{\frac{U}{U_t}} - 1 \right) + C \frac{dU}{dt} \tag{3.9}$$

Separating the differential leads to the system equation:

$$\frac{dU}{dt} = \frac{1}{C} \left(I - I_r \left(e^{\frac{U}{U_t}} - 1 \right) \right) \tag{3.10}$$

According to step 1, the current I is defined as the input $x(t)$ and the voltage U as the output $y(t)$.

Following step 2, the nonlinear system equation (3.10) is expanded in a Taylor series around the working point $WP(U_{WP}; I_{WP})$:

$$\begin{aligned} \frac{dU}{dt} = f\left(U_{WP}, I_{WP}\right) &+ \left.\frac{\partial f}{\partial I}\right|_{WP} (I - I_{WP}) \\ &+ \left.\frac{\partial f}{\partial U}\right|_{WP} (U - U_{WP}) \\ &+ \left.\frac{\partial^2 f}{\partial U^2}\right|_{WP} \frac{(U - U_{WP})^2}{2!} \\ &+ \left.\frac{\partial^3 f}{\partial U^3}\right|_{WP} \frac{(U - U_{WP})^3}{3!} + \dots \end{aligned} \tag{3.11}$$

where the function f is the right-hand side of Equation 3.10:

$$f = \frac{1}{C} \left(I - I_r \left(e^{\frac{U}{U_t}} - 1 \right) \right) \tag{3.12}$$

$$f\left(U_{WP}, I_{WP}\right) = 0 \tag{3.13}$$

For a given working point current I_{WP}, the working-point voltage U_{WP} can be calculated from the stationary solution of the system Equation 3.10:

$$\begin{aligned} 0 &= I_{WP} - I_r \left(e^{\frac{U_{WP}}{U_t}} - 1 \right) \\ U_{WP} &= U_t \ln \left(\frac{I_{WP}}{I_r} + 1 \right) \end{aligned} \tag{3.14}$$

For convenience, offset variables for current and voltage are introduced:

$$U^* = U - U_{WP}; \qquad I^* = I - I_{WP}; \qquad \dot{U}^* = \dot{U} - \dot{U}_{WP} \tag{3.15}$$

i.e. only the AC part of the signal (amplitude and phase shift) is analysed and the DC part is neglected, because it is already known (Equation 3.14) and constant, i.e. it does not influence the higher harmonics. With this, the model equation Taylor-approximated around the working point becomes:

$$\begin{aligned} \frac{dU^*}{dt} = \frac{I^*}{C} &- \frac{I_r}{CU_t} e^{\frac{U_{WP}}{U_t}} U^* \\ &- \frac{I_r}{2CU_t^2} e^{\frac{U_{WP}}{U_t}} U^{*2} \\ &- \frac{I_r}{6CU_t^3} e^{\frac{U_{WP}}{U_t}} U^{*3} \quad + \dots \end{aligned} \tag{3.16}$$

For simplicity, the constant factors are combined into global constants:

$$\begin{aligned} K_1 = \frac{1}{C} \quad ; \qquad K_2 = -\frac{I_r}{CU_t} e^{\frac{U_{WP}}{U_t}} \\ K_3 = -\frac{I_r}{2CU_t^2} e^{\frac{U_{WP}}{U_t}} \quad ; \qquad K_4 = -\frac{I_r}{6CU_t^3} e^{\frac{U_{WP}}{U_t}} \end{aligned} \tag{3.17}$$

So the Taylor-approximated system equation becomes:

$$\frac{dU^*}{dt} = K_1 \cdot I^* + K_2 \cdot U^* + K_3 \cdot U^{*2} + K_4 \cdot U^{*3} + \dots \tag{3.18}$$

Substituting the ansatz functions (Equation 3.2) with $x(t) = I^*$ for the input and Equation 3.5 with $y(t) = U^*$ for the output signal) into this equation (step 4) and applying harmonic probing for the first order $e^{j\omega t}$ results in:

$$\begin{aligned} \frac{A}{2} e^{j\omega t} H_{1,0} \cdot j\omega &= K_1 \cdot \frac{A}{2} e^{j\omega t} + K_2 \cdot \frac{A}{2} e^{j\omega t} H_{1,0} \\ H_{1,0} \cdot j\omega &= K_1 + K_2 \cdot H_{1,0} \\ H_{1,0} &= \frac{K_1}{j\omega - K_2} \end{aligned} \tag{3.19}$$

In the same way, harmonic probing for the second order $e^{2j\omega t}$ results in:

$$\begin{aligned} H_{2,0} \cdot 2j\omega &= K_2 \cdot H_{2,0} + K_3 \cdot (H_{1,0})^2 \\ H_{2,0} &= \frac{K_3 \cdot (H_{1,0})^2}{2j\omega - K_2} = \frac{K_3 K_1}{(2j\omega - K_2)(j\omega - K_2)^2} \end{aligned} \tag{3.20}$$

Similarly, harmonic probing for $e^{3j\omega t}$ results in $H_{3,0}$:

$$H_{3,0} = \frac{6K_3 H_1(\omega) H_2(\omega, \omega) + 3K_4 H_1(\omega)^3)}{3(-K_2 + 3j\omega)} \tag{3.21}$$

As can be seen from Equation 3.19, the first order FRF (i.e. the EIS spectrum) contains only the linear system parameters K_1 and K_2 of the system. Thus, as seen from Equations 3.17, only the capacity is contained in K_1, but K_2 contains both diode parameters I_r and U_t. To separate these, knowledge of K_3 (i.e. a nonlinear system parameter) is necessary, which can only be obtained from $H_{2,0}$ or higher order FRFs.

In the next chapter, this example will be further developed to demonstrate the derivation of the HFRF from measured or numerically simulated higher harmonics.

3.4 Experimental and Numerical Derivation of Higher Order Frequency Response Functions

In addition to the analytical derivation, the HFRF can be determined from experimentally measured or numerically simulated quasi-frequency response functions (QFRF) $H_{q,n}(\omega, A)$. These functions are obtained by measuring or simulating the output signal and transforming it into the frequency domain (e.g. by discrete Fourier transform, DFT) for a whole spectrum of frequencies of the input signal. Then, these quasi-frequency response functions can be related to the HFRF. This can be demonstrated by

rearranging the Volterra series (Equation 3.6) by the power of $e^{j\omega t}$:

$$
\begin{aligned}
y(t) \;=\; & e^0 \left[\underbrace{\frac{A^2}{2} H_{2,1} + \frac{3}{8} A^4 H_{4,2} + \ldots}_{H_{q,DC}(\omega,A)} \right] + \\
& \frac{1}{2} \Bigg(e^{j\omega t} \left[\underbrace{A H_{1,0} + \frac{3}{4} A^3 H_{3,1} + \ldots}_{H_{q,I}(\omega,A)} \right] + e^{-j\omega t} \left[\underbrace{A H_{1,1} + \frac{3}{4} A^3 H_{3,2} + \ldots}_{H_{q,I}(-\omega,A)} \right] + \\
& e^{2j\omega t} \left[\underbrace{\frac{A^2}{2} H_{2,0} + \frac{A^4}{2} H_{4,1} + \ldots}_{H_{q,II}(\omega,A)} \right] + e^{-2j\omega t} \left[\underbrace{\frac{A^2}{2} H_{2,2} + \frac{A^4}{2} H_{4,3} + \ldots}_{H_{q,II}(-\omega,A)} \right] + \\
& e^{3j\omega t} \left[\underbrace{\frac{A^3}{4} H_{3,0} + \frac{5}{16} A^5 H_{5,1} + \ldots}_{H_{q,III}(\omega,A)} \right] + e^{-3j\omega t} \left[\underbrace{\frac{A^3}{4} H_{3,3} + \frac{5}{16} A^5 H_{5,4} + \ldots}_{H_{q,III}(-\omega,A)} \right] \Bigg) \\
& + \ldots
\end{aligned}
\tag{3.22}
$$

With this, the individual higher order frequency response functions $H_n(\omega_1, \ldots, \omega_n)$ can be related to the amplitude dependent quasi-response functions of the harmonics $H_{q,i}(\omega, A)$:

$$
\begin{aligned}
H_{q,I}(\omega, A) &= A H_{1,0} + \frac{3}{4} A^3 H_{3,1} + \frac{5}{8} H_{5,2} + \ldots && (3.23) \\
H_{q,II}(\omega, A) &= \frac{A^2}{2} H_{2,0} + \frac{A^4}{2} H_{4,1} + \ldots && (3.24) \\
H_{q,III}(\omega, A) &= \frac{A^3}{4} H_{3,0} + \frac{5}{16} A^5 H_{5,1} + \ldots && (3.25) \\
&\ldots
\end{aligned}
$$

One possibility to determine the HFRF is to measure the quasi-response functions at several exciting amplitudes and to use a conversion matrix to approximate the HFRF. From Equation 3.23 it can be seen that if one measures the first quasi-response function at three different amplitudes, the conversion can be done by solving [236]:

$$
\begin{bmatrix} H_{q,I}(\omega, A_1) \\ H_{q,I}(\omega, A_2) \\ H_{q,I}(\omega, A_3) \end{bmatrix} = \begin{bmatrix} A_1 & \frac{3}{4} A_1^3 & \frac{5}{8} A_1^5 \\ A_2 & \frac{3}{4} A_2^3 & \frac{5}{8} A_2^5 \\ A_3 & \frac{3}{4} A_3^3 & \frac{5}{8} A_3^5 \end{bmatrix} \begin{bmatrix} H_{1,0} \\ H_{3,1} \\ H_{5,2} \end{bmatrix} \tag{3.26}
$$

Alternatively, if the amplitude is chosen carefully, the HFRF can be approximated in a very simple way and only one measurement with one specific amplitude is necessary. If the amplitude is chosen such that the third and higher order harmonics are negligibly small in comparison with the first and second harmonic, then also the third and higher order HFRF become negligible, i.e. Equation (3.25) can be neglected and the sums in Equations 3.23 and 3.24 can be aborted after the first term, leading to the following simple conversion equations:

$$H_{1,0} = \frac{H_{q,I}(\omega, A)}{A} \tag{3.27}$$

$$H_{2,0} = 2\frac{H_{q,II}(\omega, A)}{A^2} \tag{3.28}$$

Both of these conversion methods of QFRF into HFRF (i.e. Equation 3.26 or Equations 3.27–3.28) have advantages and disadvantages. On the one hand, the first method (Equation 3.26) requires several measurements at different amplitudes. However, with this approach it is possible to derive as many HFRF as desired. Additionally, the accuracy of the results can be improved by taking more harmonics into account. Therefore, this method is suitable for basic analysis, e.g. model discrimination or parameter estimation. On the other hand, the second method (Equations 3.27–3.28) requires a carefull determination of the excitation amplitude. However, once a suitable amplitude is determined, this method already gives additional nonlinear information in one experiment with the same experimental effort as EIS. With this, it is especially suitable for diagnosis.

As an example for the first method, the determination of HFRF from experimentally measured and numerically simulated QFRF for the electrical system described in Section 3.3 is demonstrated in Figure 3.2. The diode parameters I_r and U_t were determined in advance from polarisation curve measurements. With these parameters, the analytically derived HFRF (Equations 3.19–3.21) were plotted. Additionally, numerical simulations of the time signal for three different amplitudes of the input signal were done. Fourier transform into the frequency domain resulted in numerical QFRFs which were transformed to HFRFs according to the first method described above (Equation 3.26). In the same fashion, experimentally measured QFRFs were transformed to HFRFs. The comparison of analytical, numerical and experimental HFRF shows a good congruence and validates the method. However, small deviations are observed, especially for high frequencies at which the magnitude of the higher harmonics become very small. These deviations are caused by numerical inaccuracies of the simulation and by measurement errors of both QFRF and polarisation curve

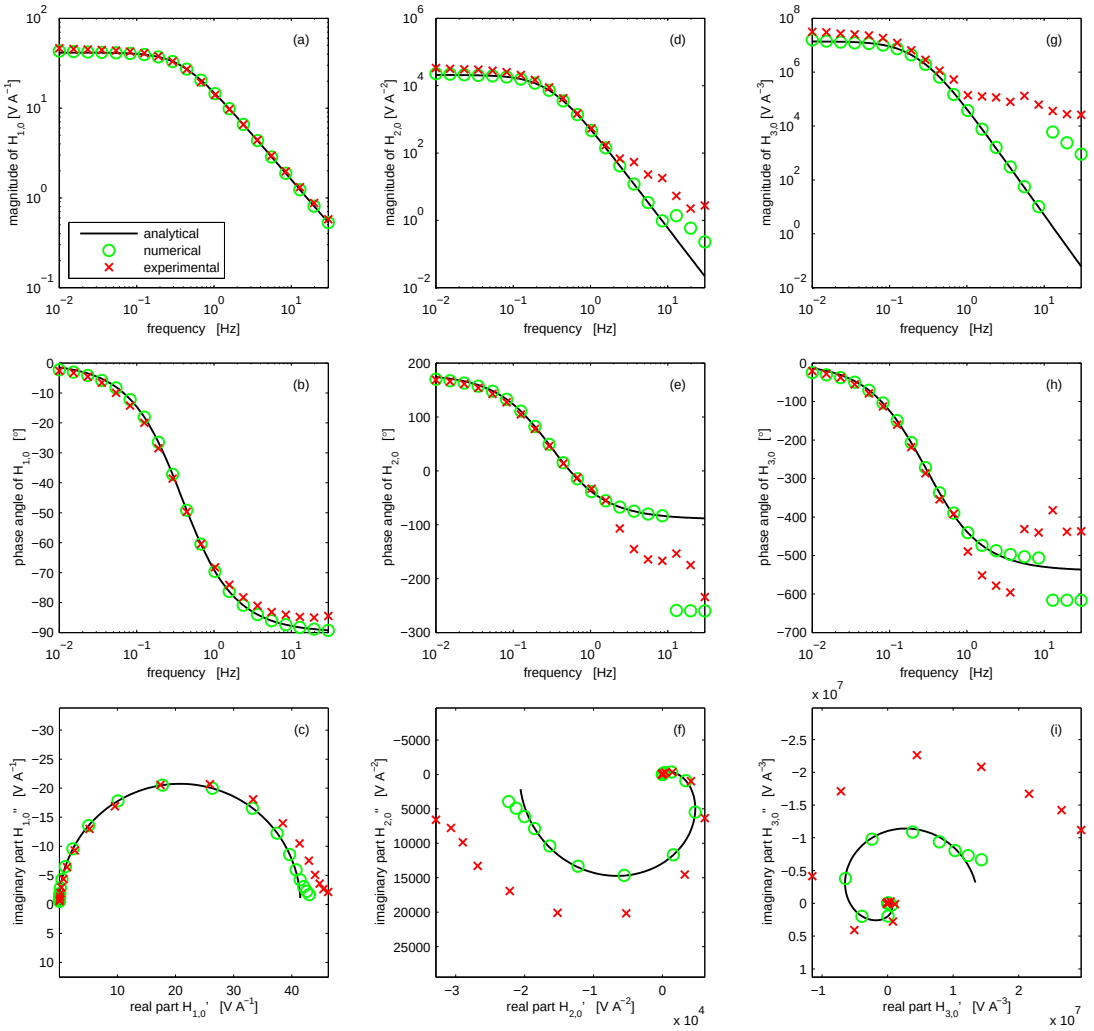

Figure 3.2: Comparison analytically (solid black line), numerically (green circles) and experimentally (red crosses) determined $H_{1,0}$ spectra (a–c), $H_{2,0}$ spectra (d–f) and $H_{3,0}$ spectra (g–i) of the electrical circuit example depicted in Figure 3.1. (a),(d) and (g) magnitude, (b),(e) and (h) phase angle and (c),(f) and (i) Nyquist-plot of $H_{1,0}$, $H_{2,0}$ and $H_{3,0}$, respectively. Experimental conditions: Capacitance 10 mF, Diode type 1N4004 with experimentally determined U_t=39.4 mV, I_r=3.137$\times 10^{-10}$ A, working point current I_{WP}=1 mA, measurements with 3 perturbation amplitudes: 0.3 mA, 0.5 mA and 0.7 mA, determination of NFRA spectra according to Eq. 3.26.

measurements.

The second method of deriving HFRF from QFRF after Equations 3.27 and 3.28 is demonstrated in Figure 3.3. In Figure 3.3a–c, the experimentally determined $H_{1,0}$ spectrum of a PEM fuel cell is compared to an EIS measurement. It is seen that $H_{1,0}$ is in congruence with the EIS spectrum (as expected from theory) although it was measured with a much higher amplitude (90mA in NFRA compared to 5mA in EIS). Simultaneously with $H_{1,0}$, the $H_{2,0}$ spectrum (Figure 3.3e–f) was obtained (Equation 3.28) with the same experimental effort (measurement time, equipment etc.) as the EIS measurement. This spectrum provides additional nonlinear information which characterises the system.

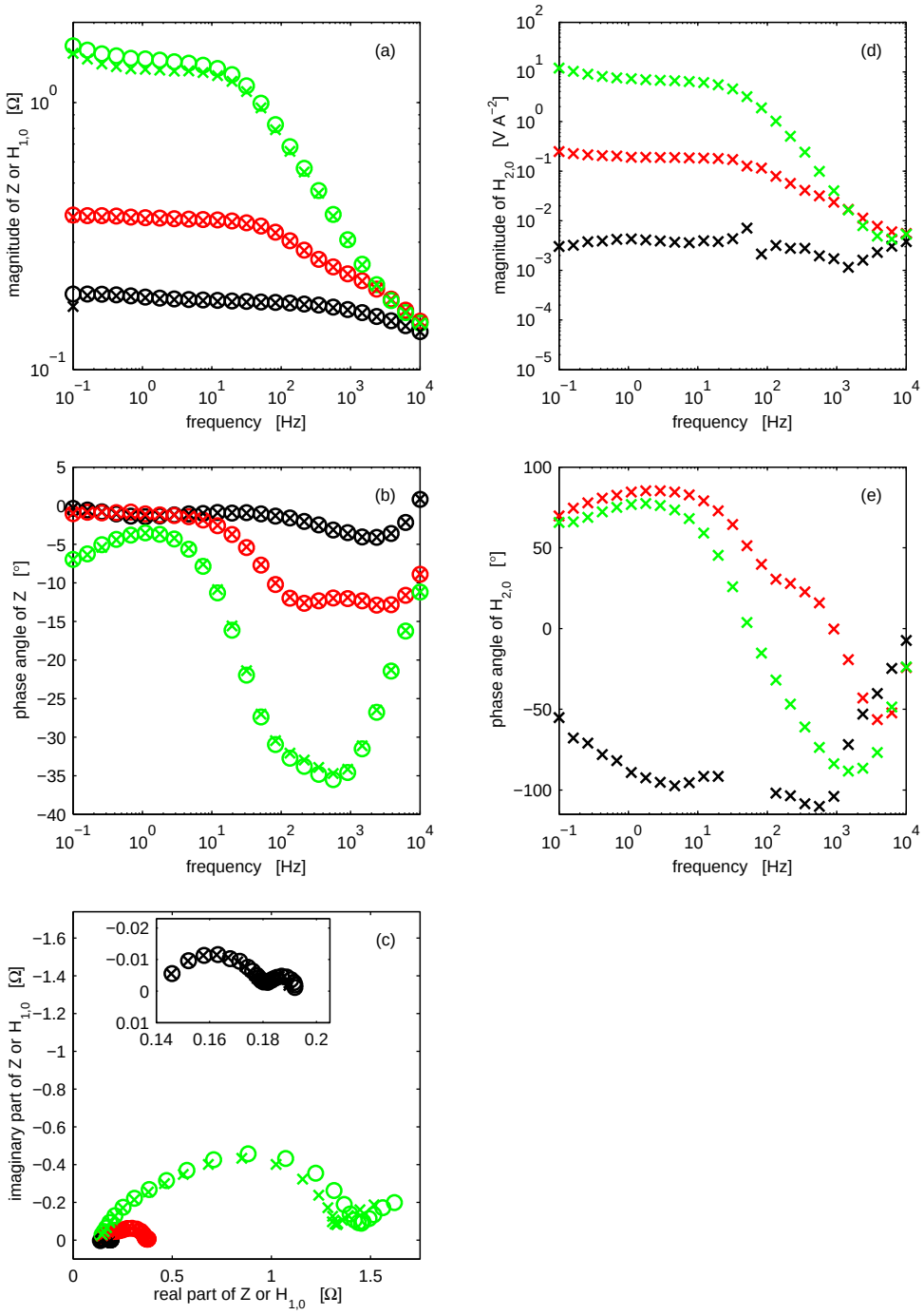

Figure 3.3: Demonstration of the experimental derivation of HFRF with Equations 3.27 and 3.28. (a–c) Comparison of experimentally derived $H_{1,0}$ spectra (crosses) and measured EIS spectra (circles) of a PEM fuel cell. (d–e) Experimentally derived $H_{2,0}$ spectra of a PEM fuel cell. Colours depict different levels of CO poisoning (black = no CO, red = 20 ppm CO, green = 100 ppm CO). H_2+CO/H_2 operation, T=80 °C, I_{WP}=0.1 A, amplitude of NFRA measurement 60 mA, amplitude of EIS measurement 5 mA.

Chapter 4

Experimental

As explained in the introduction (Chapter 1), preliminary experiments with a PEM fuel cell under dehydration, flooding and CO poisoning are done in this work (Chapter 5). The methods and materials for those experiments are explained in Section 4.1. As a consequence of those preliminary experiments, a special experimental setup was designed for a further detailed analysis of the most interesting cases of CO poisoning (Chapter 6) and dehydration (Chapter 7). This so-called differential H_2/H_2 cell setup is described in Section 4.2 and the experimental procedures for the detailed analysis are explained. Finally, some comments on stability, accuracy and reproducibility of the measurements are given in Section 4.3.

4.1 Experiments with PEMFCs of Technical Size

The experiments which will be presented in Chapter 5 were performed using a single 26 cm^2 PEM fuel cell with a Nafion® 1035 membrane. The Nafion® membrane was prepared by boiling in 5% H_2O_2 solution for one hour at 90 °C, washing in hot water, boiling in 1 molar H_2SO_4 solution for two hours at 100 °C, washing in hot water and boiling in water for two hours. Deionised water additionally filtered with a Millipore® purification system and an ohmic resistivity greater than 10 MΩ cm was used for all experiments.

A catalyst ink consisting of platinum black (Alfa Aesar) and 10 wt% Nafion® from Nafion solution (10 wt% in water) was spray-painted onto the membrane with a resulting catalyst loading of 1 mg cm^{-2} Pt. After spraying, the catalyst layer was dried at 120 °C and sintered onto the membrane at 130 °C for 30 min to ensure protonic conductivity between catalyst layer and membrane.

Toray paper TGP-H-060 hydrophobised with 30 wt% PTFE was used as gas diffusion layer. Graphite plates with a flow field consisting of four parallel serpentine channels with a length of 142 mm, width of 1.5 mm, depth of 2 mm and 2 mm ribs between them and covering an area of 40 mm $\times$ 63 mm were used for the gas distribution. Gold-plated copper current collector plates provided the electrical connection. Stainless steel end plates braced the cell together with 12 screws fixed with a torque of 7 Nm, thus providing mechanical stability and high heat distribution whereas the clamping pressure supported a low contact resistance. The cell temperature was set by a PID controlled heating band. The feed gases were humidified by temperature controlled bubbler bottles and then further heated up to the desired temperature by PID controlled heated gas pipes. The desired relative humidity was set by the ratio between humidification and gas temperature. The relative humidities and temperatures of the gases were measured directly before the cell entries and after the cell exits by Driesen+Kern DKRF400-EXT Humidity and Temperature Probes. The volume flow rates of the gases were adjusted by ABB Model A6100 flowmeters.

The cell was electrically controlled by an Amel Instruments Model 7060 High Current Potentiostat/Galvanostat with two Model 7061 Power Boosters, resulting in a maximum current range of 30 A. The resulting output signals were analysed by a Newtons4th PsimetriQ PSM1700 Phase Sensitive Multimeter.

The gas flow rates were set to 16 l h^{-1} for hydrogen and 25 l h^{-1} for air. The gas temperature and the cell temperature were set to 70 °C. In the CO experiments 10 ppm CO were mixed into the hydrogen and the humidification temperature was 70 °C. Polarisation curves were taken before each experimental series with 0.5 A increments of 45 min holding time each and a ramp of 1 mA s^{-1} between each increment.

The NFRA spectra were taken in galvanostatic mode at three different working points, i.e. 3 A, 6 A and 9 A (corresponding to 0.115 A cm^{-2}, 0.231 A cm^{-2} and 0.346 A cm^{-2}), with excitation amplitudes given in Table 4.1. The frequency interval of the spectra ranged from 1 kHz to 10 mHz with five points per decade. The first five harmonics of the output signal were measured to ensure that the harmonics higher then the desired second were sufficiently small. To determine the appropriate amplitude to meet the criteria for the analysis corresponding to Section 3.4, a first spectrum at a sufficiently high amplitude was measured. The frequency of the maximum of the third harmonic was determined. At this frequency, the amplitude was varied to determine the value at which the third harmonic disappears, while the second harmonic is still visible. Consequently, the determined amplitude was used to measure the desired NFRA spectra in this working point. These NFRA spectra were determined according

Table 4.1: Excitation amplitudes for a 26 cm^2 PEMFC under dehydration, flooding and anode CO poisoning.

operating condition	working point		
	3 A	6 A	9 A
dehydrated	1.5 A	1.5 A	2 A
normal	1.5 A	1.5 A	1.5 A
flooded	1.2 A	1.5 A	1 A
without CO	1.5 A	2.5 A	2.5 A
with CO	1.5 A	2.5 A	1.7A

to the mathematical method described in Section 3.4 using Equations 3.27 and 3.28.

In order to obtain NFRA spectra under dehydrated, optimal and flooded conditions, the influence of humidification on the fuel cell behaviour was determined in preliminary experiments. For this, the cell was kept at constant current and the relative humidity of the feed gases was increased stepwise from low values until flooding occurred. If the cell voltage increased after increasing the humidity, the cell had been dehydrated before. If the voltage decreased rapidly after increasing the humidity, the cell had been flooded. After this, NFRA spectra were measured under all operating conditions after a minimum holding time of at least 30 min.

4.2 Experiments with Differential H_2/H_2 cells

In this section, the preparation and conditioning of a differential H_2/H_2 cell as used in Chapters 6 and 7 is described. Furthermore, the instrumentation and procedures for the measurement of polarisation curves, EIS spectra and NFRA spectra are explained.

A sketch of the differential H_2/H_2 PEM fuel cell can be found in Figure 4.1. The polymer electrolyte membrane consisted of Nafion® 1035 and was prepared with the same boiling procedure as described previously in Section 4.1.

The catalyst layer was prepared by a spray painting procedure as described in the previous section. The active area of the differential design was 1.6 mm x 63 mm, i.e. 1 cm^2 with a target Pt loading of 1 mg cm^{-2}. Due to the low overall Pt mass the target loading could only be prepared with high relative error and a large inaccuracy in the Pt loading was expected. Therefore, the mathematical models had to account for this inaccuracy, as will be explained later in the discussion of the results.

The gas diffusion layer consisted of Toray paper TGP-H-060 hydrophobised with 15 wt% PTFE. Graphite flow field plates with 21 parallel flow channels with a length

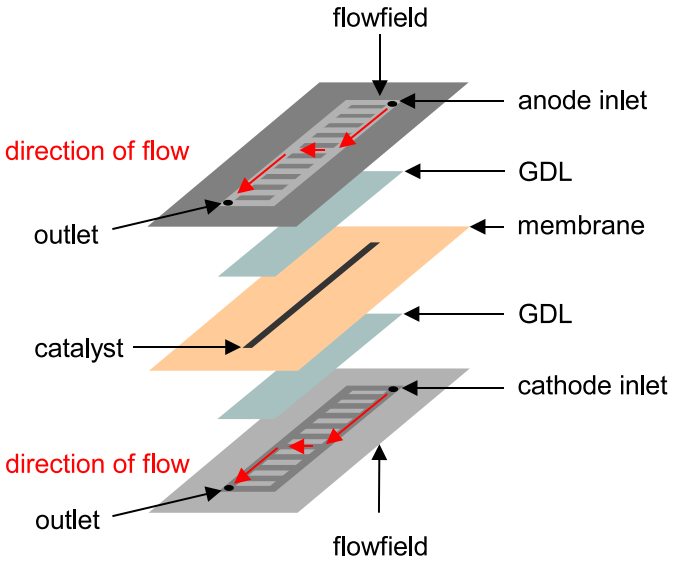

Figure 4.1: Sketch of the differential fuel cell assembly.

of 40 mm, width of 2 mm, depth of 2 mm and 1 mm ribs between them distributed the gases. Similar gold plated copper current collectors and stainless steel end plates as described in Section 4.1 completed the cell.

The cell was run in a FuelCon Evaluator C test station at a temperature of 80 °C. The gases had flow rates of 200 ml min^{-1} on both sides in order to ensure a high overstoichiometry. They were humidified by the bubbler bottles at 70 °C and kept at 90 °C between the bubbler bottles and the cell in order to prevent condensation of the water. A Solartron 1286 potentiostat together with a Solartron 1250 frequency response analyser were used for the measurements.

The cell was initially conditioned by a method similar to that of Himanen et al. [14]. During the conditioning, the cell was operated in normal fuel cell mode with hydrogen at the anode and oxygen at the cathode. The current was increased stepwise from 0 to 1 A cm^{-2} in steps of 50 mA cm^{-2} with a duration of 20 min. After this, the cell was purged with nitrogen, anode and cathode were reversed and the procedure was repeated. This whole procedure was repeated three times until the cell performance was stable and the polarisation curve was reproducible. After this, the cell was purged with nitrogen and the H_2/H_2 measurements were started.

Cell polarisation curves were taken by applying constant voltage steps from the

open circuit voltage 0 V to -0.9 V with 2 min duration, after which the measured current was stable and in steady state.

All EIS and NFRA spectra were taken in galvanostatic mode in order to control the reaction rates directly. If potentiostatic control would have been used, especially in the case of NFRA, a high amplitude voltage signal could force very high currents to flow and the resulting faradaic rectification current could lead to accelerated degradation of the cell. This is prevented by using galvanostatic control.

EIS spectra were measured at a working point of 0.1 A cm^{-2} (see Chapter 6 for a discussion of the working point selection) with an amplitude of 10 mA cm^{-2} in the frequency range from 0.1 Hz to 10 kHz. For the measurement of NFRA spectra the same working point and frequency range were used. The excitation amplitude for the NFRA spectra was determined in a preliminary experiment: in order to use the simplified NFRA approach as described in Section 3.4, the amplitude must be large enough to be able to measure first and second harmonic but has to be so small that the third harmonic is negligible compared to the first harmonic and the fourth harmonic has to be negligible compared to the second harmonic. This restriction was fullfilled at an amplitude of 90 mA cm^{-2} in the measurements without CO (Chapter 7 and reference measurements in Chapter 6) and at an amplitude of 60 mA cm^{-2} in the measurements with 20 ppm and 100 ppm CO in Chapter 6. The NFRA spectra were calculated from the measured higher harmonics according to the mathematical method described in Section 3.4 using Equations 3.27 and 3.28.

4.3 Reproducibility

In the preliminary experiments in Chapter 5, the reproducibility of the NFRA measurements was analysed by measuring every NFRA spectrum three times and calculating the measurement error. From this analysis, a more rigorous experimental procedure was derived for the measurements of the EIS and NFRA spectra with the differential H_2/H_2 cell in Chapters 6 and 7: first, the working point was approached with a slow ramp from 0–100 mA cm^{-2} with a slew rate of 1 mA cm^{-2} s^{-1}. Then the cell was operated at the working point for 5 min to ensure that the voltage was stable. After this, an EIS spectrum was measured. Then the cell was again operated for 5 min at constant current before an NFRA spectrum was measured and finally the cell was again operated for 5min at constant current. The measurement of the cell voltage during the operating phases at constant current ensured that the working point was stable during

the whole measurement cycle. This measurement cycle was repeated three times in order to check and ensure a good reproducibility of the measurements.

As an example, in Figure 4.2 three NFRA spectra measured with this procedure are shown. This example is the measurement with the “worst case” of reproducibility: 100 ppm CO poisoning of the anode. However, even in this case an acceptable reproducibility is achieved.

Furthermore, it can be seen in these spectra that measurement noise is worst in the low frequency region because at low frequencies the measurement time for one data point is longer. Thus, measurement of very low frequencies is not only time-consuming but also more inaccurate.

Accuracy of the data points can be improved by measuring and averaging over several cycles of the input signal. Nevertheless, this is a trade-off between accuracy and measurement time (and thus stability). In this work, the input signal was averaged over 20 cycles. Thus, noise is reduced by a factor of $\sqrt{20}$ while increasing measurement time by a factor of 20.

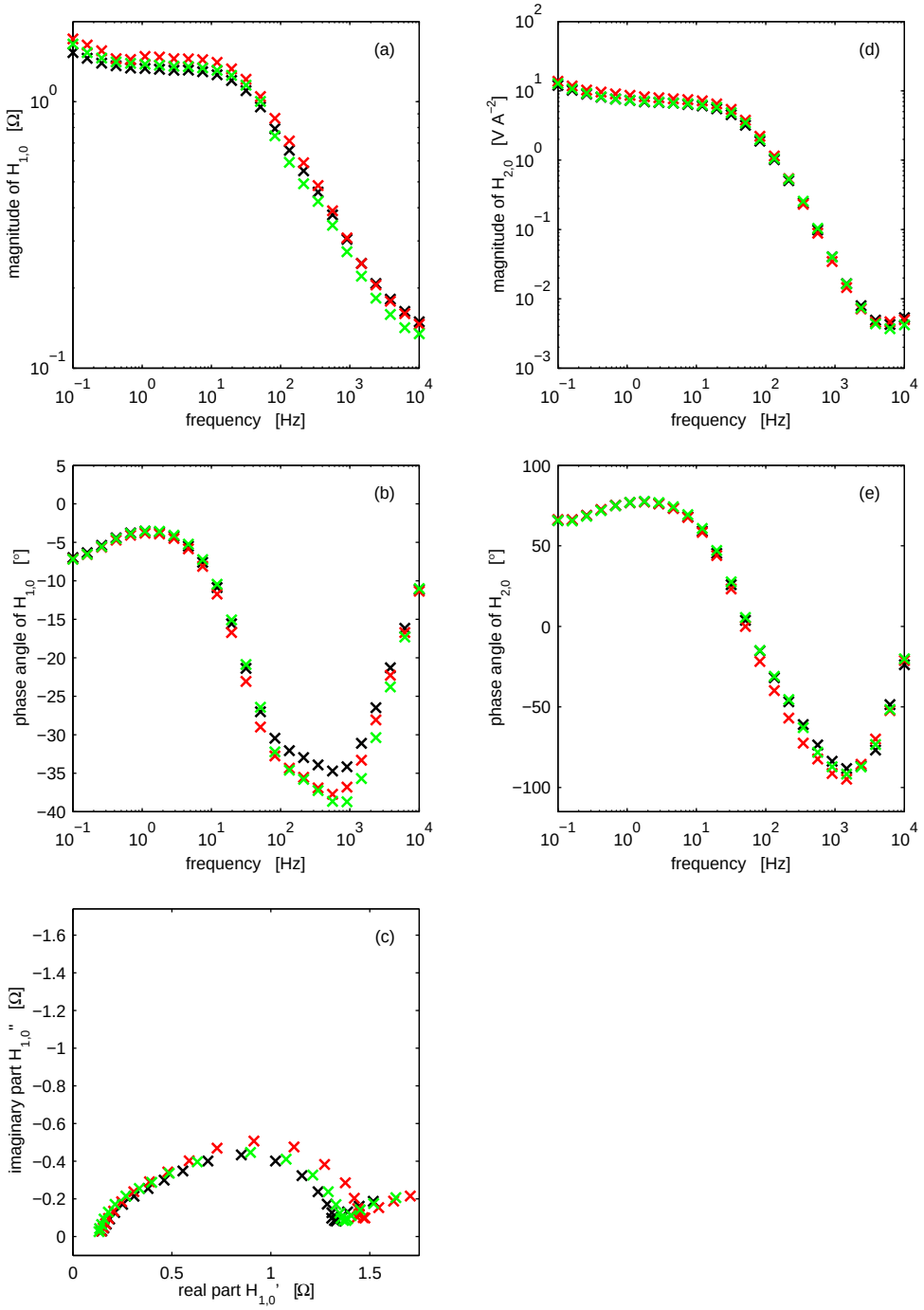

Figure 4.2: Reproducibility of 3 measured $H_{1,0}$ spectra (a–c) and $H_{2,0}$ (d–e) spectra. H_2+CO/H_2 operation with 100 ppm CO, T=80 °C, I_{WP}=0.1 A, amplitude of NFRA measurement 60 mA. Black = first measurement, red = second measurement, green = third measurement.

Chapter 5

NFRA for Diagnosis of Dehydration, Flooding and CO Poisoning in a PEMFC of Technical Size

In a first step, the unambiguous diagnosis of dehydration, flooding or CO poisoning in a PEMFC of technical size is investigated. For this, the linear frequency response function $H_{1,0}$ is used in correspondence to classic EIS spectra. Additionally, the nonlinear behaviour of the system is taken into consideration in the form of the second order frequency response function $H_{2,0}$, determined as described in Section 3.4. In order to do so, the first and second order FRFs under normal operating conditions are measured at three different working points: 3A, 6A and 9A (corresponding to 0.115 A cm^{-2}, 0.231 A cm^{-2} and 0.346 A cm^{-2}), i.e. activation controlled region, linear region controlled by membrane and ohmic resistances and mass transport controlled region, respectively. At first, reference measurements at these points under normal operating conditions are made. Afterwards, the humidification is changed to dehydrate and flood the cell. In the last step, the anode is poisoned with 10ppm CO in the fuel gas. Under these conditions, first and second order FRFs are measured at all three working points. In the following analysis, the differences of the linear FRFs will be discussed in the first step. It can be seen that this information is not sufficient to distinguish the failure sources unambiguously. Therefore, in the next step the second order FRFs are discussed, which provide sufficient additional information to diagnose the PEMFC's failures unambiguously.

5.1 Normal Conditions

Figure 5.1 shows the first and second order frequency response functions under normal conditions at the aforementioned working points. The first order FRF $H_{1,0}$ represents the linear part of the system. According to the theory, it is identical with the classic electrochemical impedance spectra. It can be seen that the measured $H_{1,0}$ functions in Figure 5.1a–c are similar to measured EIS spectra in literature (e.g. [65, 195, 197–199, 218, 219, 238]).

As Springer et al. [65] stated, the generic linear impedance spectra of fuel cells consist of a high frequency arc representing the combination of an effective charge transfer resistance in parallel to the double layer capacity and a low frequency arc reflecting the mass-transport limitations of the gas within the gas diffusion and catalyst layers (see Figure 5.1c). Additionally, at very low frequencies a slight inductive behaviour is measured, which might be attributed to water transport in the anode side of the membrane [239, 240] and/or peroxide production at the cathode [241]. As the current increases, i.e. the voltage decreases, the overpotential increases. With this, the diameter of the high frequency arc decreases, reflecting the increasing driving force for the interfacial oxygen reduction process [65]. The low frequency arc grows with increasing current, reflecting the increasing diffusion limitations in the backing [65].

The second order FRFs $H_{2,0}$ in Figure 5.1d–e can unfortunately not be directly related to different physical effects, they can only be interpreted in a mathematical form. Nevertheless, their main feature under normal conditions is their decrease in magnitude with increasing current, especially at middle to low frequencies. The error bars show that the accuracy of the second order FRFs is good, except in the frequency range below 100 mHz, which is not of interest for the current discussion. These inaccuracies occur because at lower frequencies the recording time and with this the error proneness increases, as described in Section 4.3.

5.2 Dehydration and Flooding

As described in Section 2.1.2, a delicate balance of liquid and vapour water depending on the operating conditions is needed in order to achieve optimal fuel cell performance. This water balance depends on different factors: (1) the water entering and exiting from the fuel cell by the humidified feed gas streams, (2) the water being produced by the electrochemical reaction at the cathode, (3) the water being carried from anode to cathode within the solvate layer of the protons, i.e. the electro-osmotic drag and (4)

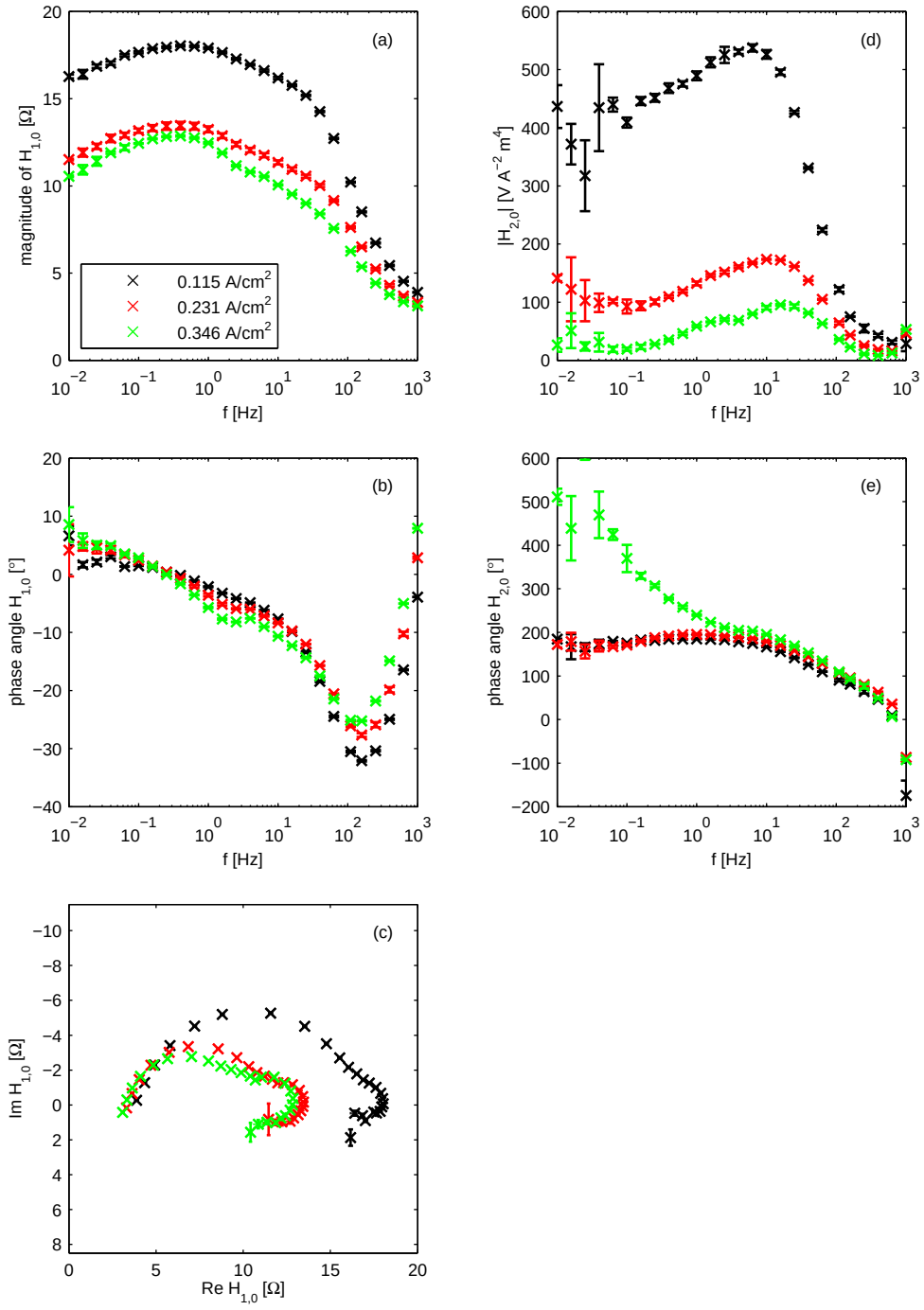

Figure 5.1: NFRA spectra under normal conditions at 3 different working points. (a)–(c) first order frequency response function $H_{1,0}$, (d)–(e) second order frequency response function $H_{2,0}$. Error bars indicate the standard deviation of 3 measurements.

the water being carried by back-diffusion from cathode to anode. Shortage of water leads to dehydration of the polymer electrolyte, whereas excess of water leads to the formation of excess liquid water, i.e. fuel cell flooding.

Since the ionic conductivity of the membrane is directly related to its water content (e.g. [16, 65]) dehydration leads to a higher ionic resistance of the membrane and catalyst layer and therefore a decrease in performance. Additionally, insufficient humidification results in a decrease of the oxygen electrocatalysis due to dehydration of the Nafion® within the catalyst layer [16, 65].

Under dehydration conditions, the first order FRF increases in magnitude over the whole frequency range for all working points, i.e. activation controlled region at j=0.115 A cm^{-2} (Figure 5.2a), linear region at j=0.236 A cm^{-2} (Figure 5.3a) and mass transport controlled region at j=0.346 A cm^{-2} (Figure 5.4a). The phase angle remains nearly unchanged at all working points over the whole frequency range, except of a very small increase at high frequencies (Figure 5.2b, 5.3b and 5.4b). This behaviour is in accordance with classic EIS results [197–199]. The Nyquist plot (Figures 5.2c, 5.3c and 5.4c) shows a shift of the spectra in the real axis, which can be attributed to the increased membrane resistance. Also, the first arc increases, which can be attributed to an increased polarisation resistance caused by dehydration of the Nafion® in the catalyst layer leading to a decrease in active surface area, as observed by [16, 65].

The second order FRF $H_{2,0}$ provides additional information: the magnitude of $H_{2,0}$ increases, especially in the middle and low frequencies, for all working points, i.e. activation controlled (Figure 5.2d), linear (Figure 5.3d) and mass transport controlled region (Figure 5.4d). The phase shows a plateau which decreases with dehydration at higher currents (see Figures 5.2e, 5.3e and 5.4e).

An excess of liquid water leads to flooding of the catalyst layer, gas diffusion media and/or the gas channels of the flow field. It occurs preferentially on the cathode, because there the water from the electrochemical reaction is produced. Additionally the electro-osmotic drag creates a water profile over the membrane from anode to cathode. Flooding in the catalyst layer may reduce the effective pore size, leading to Knudsen diffusion and may also force the dissolution and diffusion of the oxygen into the liquid water. Flooding in the gas diffusion layer leads to two-phase flow hindering the oxygen transport to the catalyst sites (e.g. [65, 195]). Macroscopic water layers in the gas channels can result in preferential flow through alternative channels, thus reducing the partial pressure of oxygen in the blocked channel [242, 243]. Finally, whole channels can be completely blocked by a liquid water plug, making this channel inactive for electrochemical reaction.

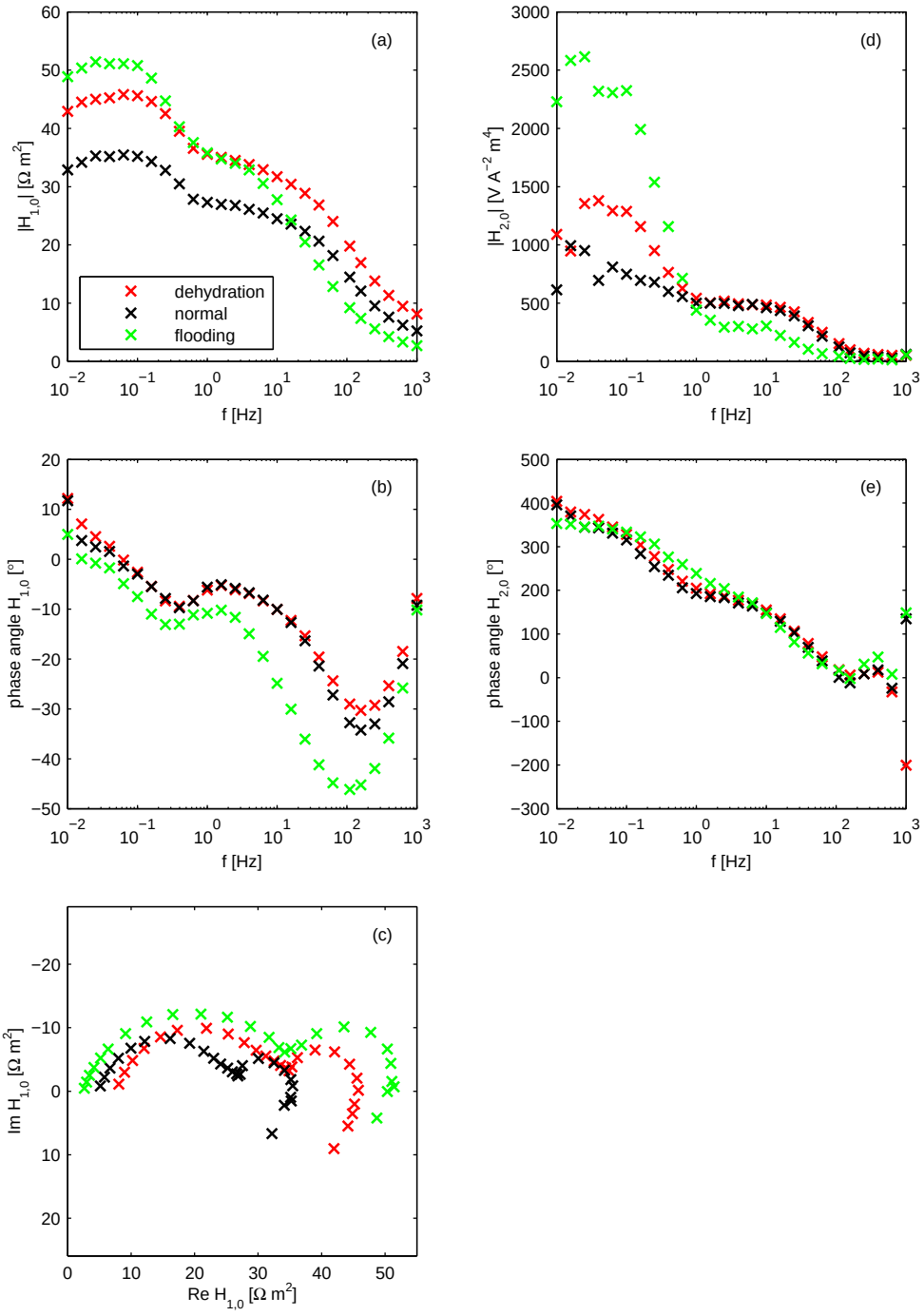

Figure 5.2: NFRA spectra at a current density of j=0.115 A cm^{-2} under dehydrated, normal and flooded conditions. (a)–(c) first order frequency response function $H_{1,0}$, (d)–(e) second order frequency response function $H_{2,0}$.

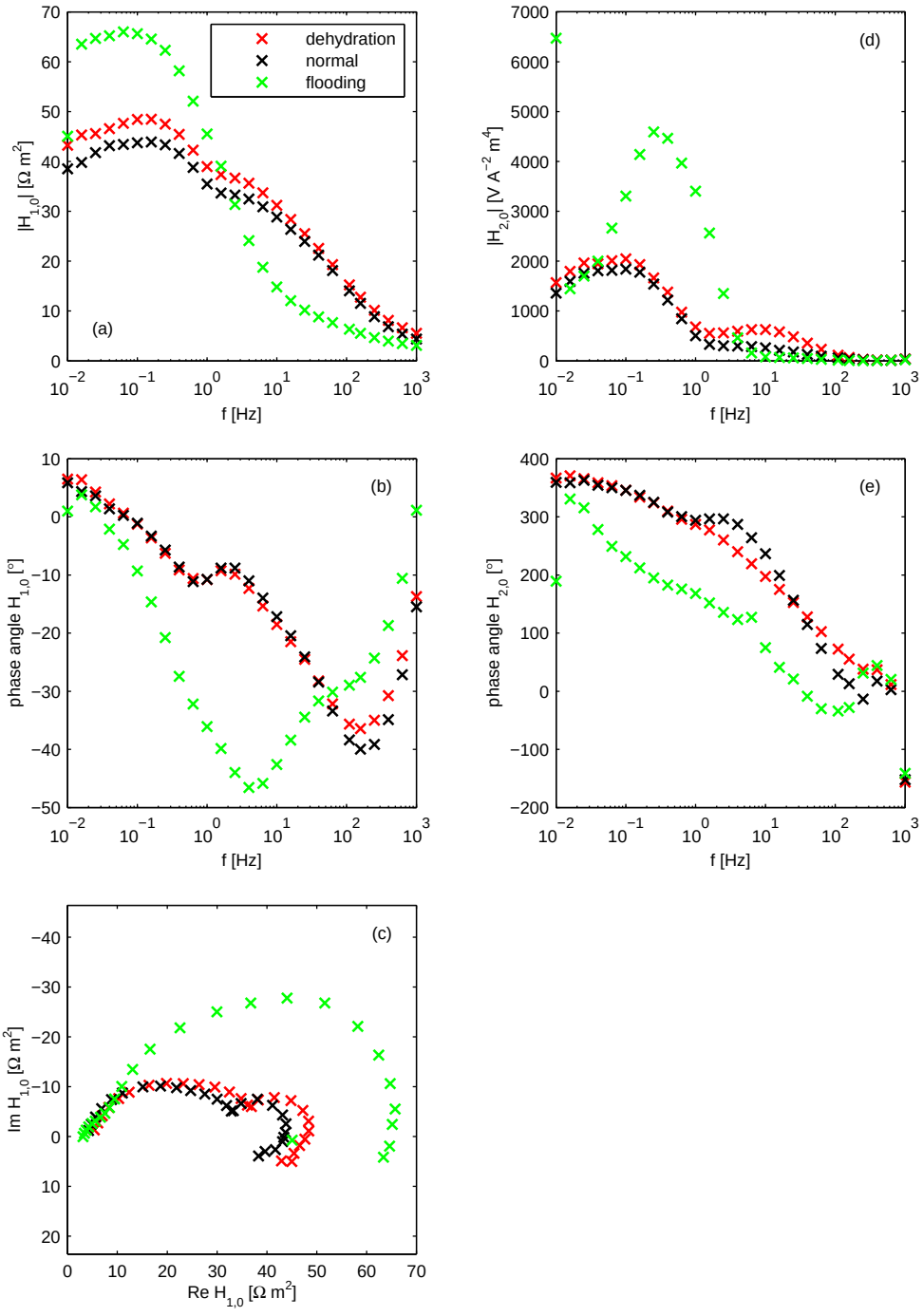

Figure 5.3: NFRA spectra at a current density of j=0.231 A cm^{-2} under dehydrated, normal and flooded conditions. (a)–(c) first order frequency response function $H_{1,0}$, (d)–(e) second order frequency response function $H_{2,0}$.

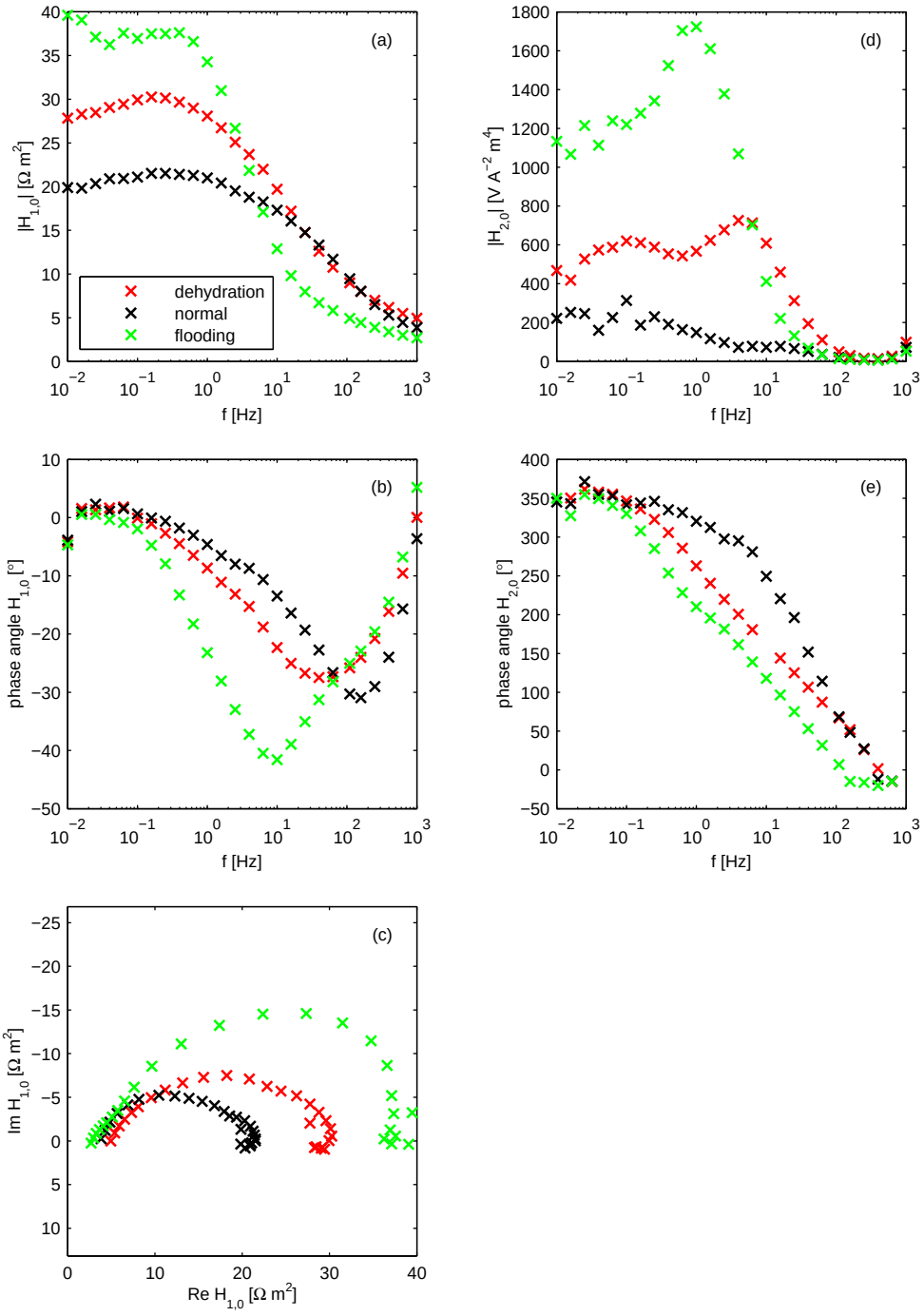

Figure 5.4: NFRA spectra at a current density of j=0.346 A cm^{-2} under dehydrated, normal and flooded conditions. (a)–(c) first order frequency response function $H_{1,0}$, (d)–(e) second order frequency response function $H_{2,0}$.

In the flooded cell, at all working points an increase of the magnitude of $H_{1,0}$ at low frequencies occurs (see Figures 5.2a, 5.3a and 5.4a), which can be attributed to an increased mass transport resistance [65]. The impedance at high frequencies is determined by losses in the catalyst layer [65] and is decreasing further under flooding conditions, because the Nafion® electrolyte in the catalyst layer becomes more humidified. Under these conditions, the first order frequency response function is sufficient to distinguish between dehydration and flooding, which is in agreement with the conclusions of Fouquet et al. [198].

As will be shown later, it is necessary to take into account the nonlinear behaviour of the system in order to distinguish dehydration and flooding from CO poisoning. The second order FRF shows an increase in magnitude at low frequencies during flooding. This increase is shifting towards higher frequencies with increasing current (compare Figures 5.2d, 5.3d and 5.4d). The phase of $H_{2,0}$ (Figures 5.2e, 5.3e and 5.4e) shows a linear decrease with increasing frequencies, similarly as discussed for the case of dehydration. During flooding, the phase of $H_{2,0}$ is decreased and even lower than in the case of dehydration, especially at higher current densities.

5.3 CO-Poisoning

Even small amounts of CO in the feed gases decrease the performance of a fuel cell considerably by decreasing the catalytic activity of the electrode [75,78]. This happens due to adsorption of CO onto the active sites of the platinum catalyst which on the one hand prevents H_2 adsorption by site exclusion [13, 215] and on the other hand lowers the reactivity of the remaining uncovered sites through dipole interactions and electron capture [13].

Figures 5.5 to 5.7 show the NFRA spectra under anode poisoning with 10 ppm CO. It can be noticed that the magnitude of the first order FRF increases, especially at low frequencies, for all working points, i.e. activation controlled region (Figure 5.5a), linear region (Figure 5.6a) and mass transport controlled region (Figure 5.7a). This is in agreement with classic EIS spectra from literature [196,199,215]. The phase of $H_{1,0}$ decreases slightly in the mid- to high frequency range (Figures 5.5b, 5.6b and 5.7b), similarly to the results of Andreaus [196]. This behaviour is explained by an increase of the polarisation resistance induced by CO-adsorption [214]. A pseudo-inductive behaviour as reported in literature [13, 215] is not clearly seen in the present measurements, because it occurs at larger CO concentrations than used here. Additionally,

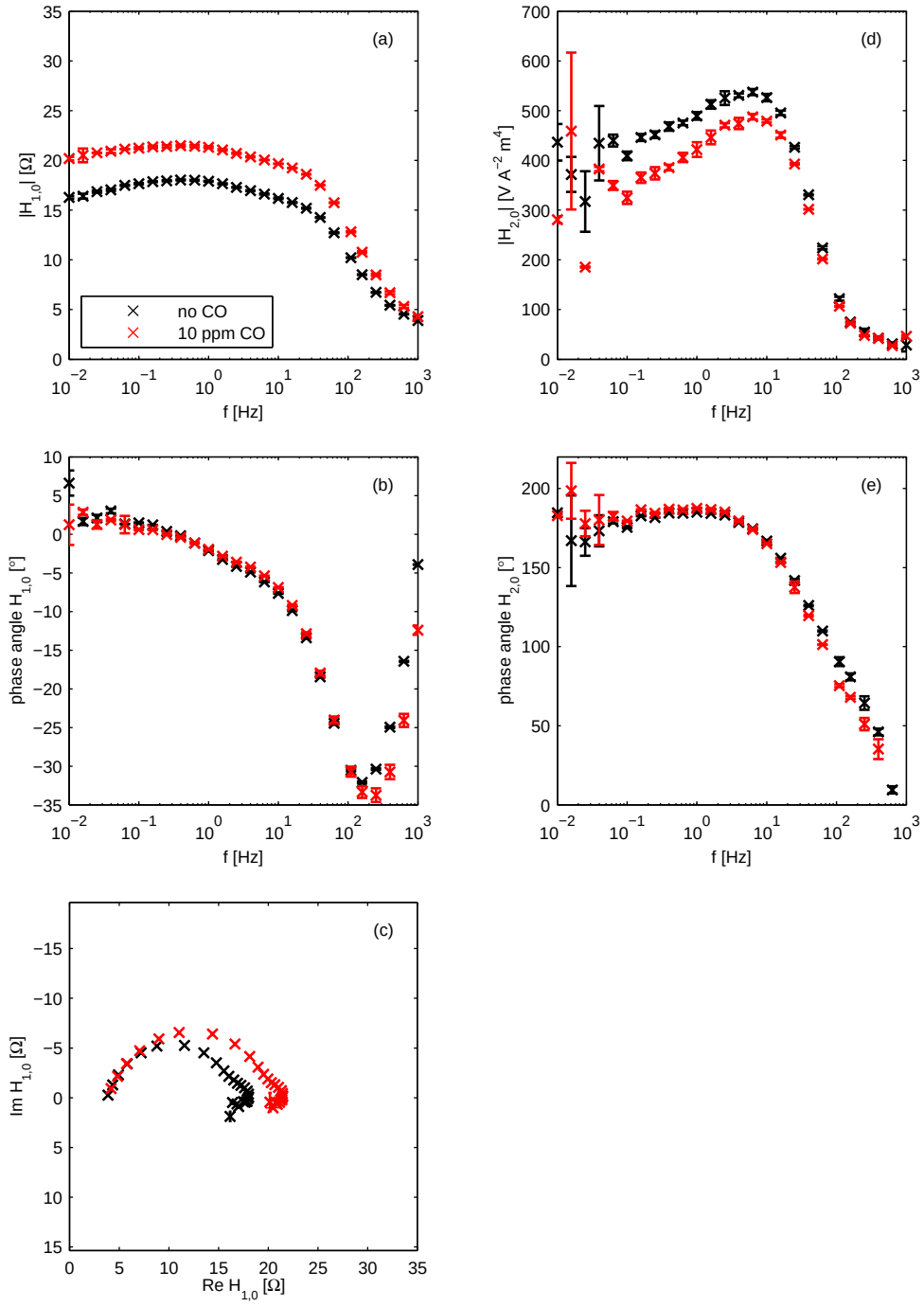

Figure 5.5: NFRA spectra at a current density of j=0.115 A cm^{-2} under normal conditions and anodic poisoning with 10 ppm CO. (a)–(c) first order frequency response function $H_{1,0}$, (d)–(e) second order frequency response function $H_{2,0}$.

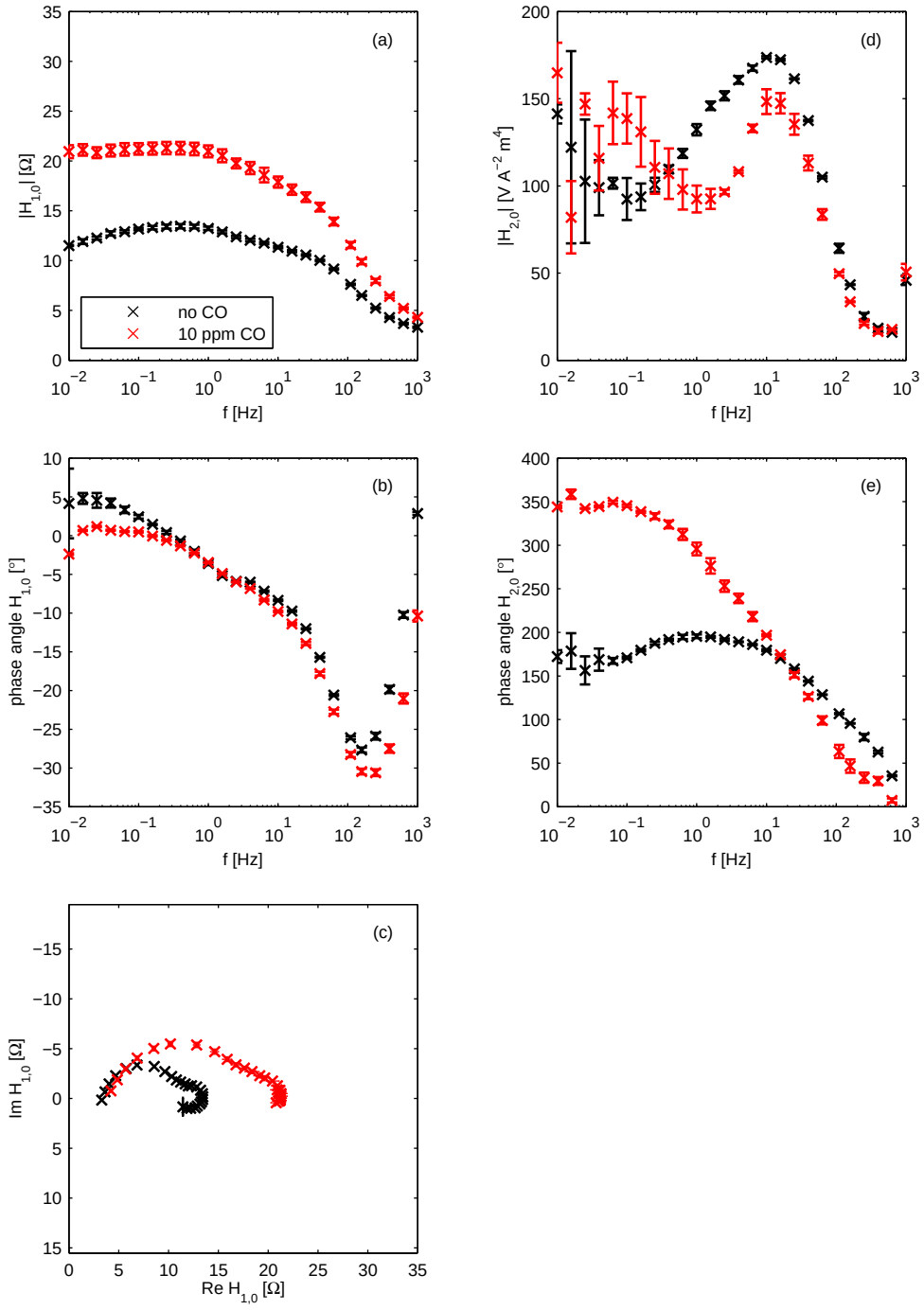

Figure 5.6: NFRA spectra at a current density of j=0.231 A cm^{-2} under normal conditions and anodic poisoning with 10 ppm CO. (a)–(c) first order frequency response function $H_{1,0}$, (d)–(e) second order frequency response function $H_{2,0}$.

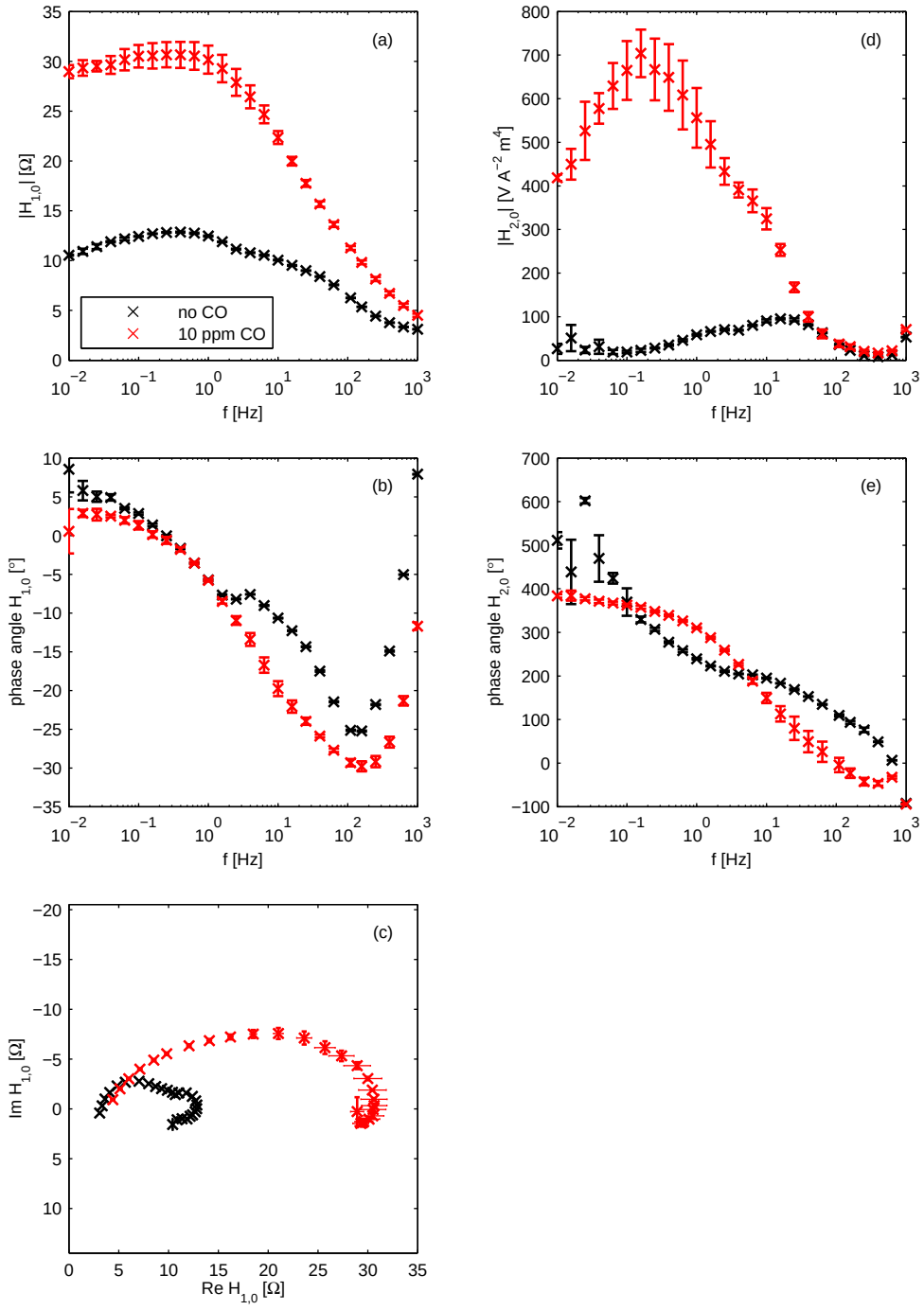

Figure 5.7: NFRA spectra at a current of density of j=0.346 A cm^{-2} under normal conditions and anodic poisoning with 10 ppm CO. (a)–(c) first order frequency response function $H_{1,0}$, (d)–(e) second order frequency response function $H_{2,0}$.

a small pseudo-inductive behaviour would be masked by the observed inductive behaviour resulting from water transport in the anode side of the membrane [239, 240] and/or peroxide production at the cathode [241] as discussed above. All in all, the behaviour of the first order FRF of the CO poisoned PEMFC is similar to the behaviour under dehydrated conditions. Therefore, the second order FRF is taken into consideration to separate CO poisoning from the other effects.

The second order FRF shows a decrease in magnitude and a higher slope of the phase response for all working points, j=0.115 A cm^{-2} i.e. activation controlled region (Figure 5.5d–e), j=0.236 A cm^{-2} i.e. linear region (Figure 5.6d–e) and j=0.346 A cm^{-2} i.e. mass transport controlled region (Figure 5.7d–e), respectively. This is an interesting feature, because in the case of flooding and dehydration, the second order FRF is increasing. With this, it is possible to unambiguously distinguish CO poisoning qualitatively from the other effects.

5.4 Conclusions

In these first preliminary experiments, the useability of NFRA for the unambiguous diagnosis of dehydration, flooding or CO poisoning was analysed in a PEMFC of technically relevant size and dimensions. In a first step, it was experimentally validated that NFRA provides similar results as classic EIS as well as additional nonlinear information about the investigated system. It was seen that the first order frequency response function $H_{1,0}$ corresponds to classic EIS, whereas higher order frequency response functions are obtained that contain additional information about the nonlinearity of the system. This can be helpful to distinguish between effects that cannot be separated by classic EIS (see e.g. [198, 199, 218, 219]).

In the following, three different PEMFC failures, i.e. dehydration, flooding and CO poisoning, were analysed on the basis of the first and second order FRFs. The first order FRFs behaved as expected from classic EIS analysis. It was seen that using only those linear spectra, the phenomena of dehydration and CO poisoning cannot be distinguished clearly. However, the analysis of higher order frequency response functions showed that the second order FRF $H_{2,0}$ provided sufficient information to distinguish CO poisoning from other effects, whereas dehydration and flooding could be clearly distinguished by the first order FRF $H_{1,0}$. It has been shown that from a phenomenological point of view it is worthwhile to take into account the nonlinear behaviour of the PEMFC in form of the higher order frequency response functions.

However, it is still unclear why the linear $H_{1,0}$ spectra show qualitatively similar behaviour under CO poisoning and dehydration. Additionally, it cannot be concluded that the behaviour of the $H_{2,0}$ spectra under CO poisoning and dehydration is clearly caused by the main mechanisms of those processes alone. There might be more complex behaviour involved resulting for example from spatial effects like concentration gradients or from unwanted interactions of side-processes with the process under investigation. Additionally, the slow cathode kinetics might have a masking effect, especially during operation with air as in the present measurements.

Therefore, in the next two chapters the cases of CO poisoning and dehydration are analysed in detail with the help of a specially developed experimental approach which excludes as many of those unwanted processes and effects as possible. Additionally, this experimental approach allows a simplified modelling, which can be used to derive the NFRA spectra numerically. The comparison of experimental and numerical NFRA spectra makes it possible to validate the main features of the NFRA spectra under CO poisoning and dehydration. Thus, it can be proven if those features make a discrimination of CO poisoning and dehydration possible and can be used for an unambiguous diagnosis.

Chapter 6

CO poisoning in the Differential H_2/H_2 Cell

In the last chapter it was seen that dehydration and CO poisoning are two interesting phenomena for NFRA diagnosis because the linear frequency response (i.e. EIS or $H_{1,0}$ spectra) shows similar qualitative behaviour under these conditions but the behaviour of the nonlinear spectra is different and might be used for discrimination. In order to find out why this is the case, in the next two chapters the two critical states CO poisoning and dehydration are investigated in detail. In order to do so, a special experimental approach was developed: a fuel cell with a differential design and H_2/H_2 operation as described in Chapter 4.2.

With this setup, a detailed analysis of the anode processes is possible because masking effects are eliminated. Slow cathodic oxygen reduction kinetics are avoided by operating the cell with hydrogen at the cathode, a well established method in literature [12–14]. Land-channel effects like starvation of oxygen under the ribs of the cathode as observed by Schneider et al. [15] are avoided in such an operation mode, because the oxygen consumption reaction is replaced by the hydrogen evolution reaction. Furthermore, undesired side-reactions of molecular oxygen (e.g. H_2O_2 formation) are avoided. Additionally, along-the channel effects like concentration gradients, fuel gas starvation or CO accumulation are prevented by a cell design with differentially short channels.

In a first step, the steady-state behaviour of the differential H_2/H_2 cell under CO poisoning is preliminarily analysed by polarisation curve measurements. In these experiments, the aim is to determine a suitable working point for the intended NFRA measurements. During these polarisation curve measurements, autonomous potential

oscillations were found in galvanostatic operation. Although these kind of oscillations are known from literature, they have not been observed in a normal fuel cell with a Pt anode before. In the following, the oscillations are investigated in detail in order to understand their nature and occurence. This is necessary for finding a working point that lies relieably in the non-oscillatory region. Otherwise the autonomous oscillations could interfere with the applied oscillations of the NFRA method. This would lead to a much more complex behaviour and would require a much more complicated analysis.

Additionally, the analysis of the oscillations demonstrates the advantages of the differential H_2/H_2 cell approach, because the oscillations are usually not observed in a fuel cell in normal operation. The reason for this is explained in the next section and the analysis of the oscillations is discussed. As a result of this analysis, a suitable working point for NFRA is determined in Section 6.2 and measured NFRA spectra under anode CO poisoning are analysed. Finally, in Section 6.3 it is discussed that the differential H_2/H_2 cell allows a simplified modelling approach, which makes it possible to calculate NFRA spectra numerically. Thus simulated spectra under CO poisoning are reviewed and compared to the experimental results. Additionally, the main "fingerprint" of CO poisoning in the NFRA spectra is collected which might be useful for an unambiguous diagnosis.

6.1 Autonomous Potential Oscillations at the Pt Anode of a PEM Fuel Cell under CO Poisoning

An interesting phenomenon occurring during the galvanostatic operation of Pt-alloy fuel cell electrodes with H_2+CO gas mixtures is the occurrence of autonomous potential oscillations. Intensive studies of these oscillations have been carried out on PtRu electrodes [98, 99, 244–246] and recently on PtPd electrodes [100]. From a non-linear system theory point of view the oscillations result from an interplay between the anode overpotential and the CO coverage. From an engineering point of view each cycle can be considered as a CO adsorption phase followed by a CO oxidation phase [95] forming a cyclic self cleaning process of the anode. The oscillations in galvanostatic mode enhance the CO oxidation compared to the potentiostatic mode, where oscillations are suppressed [97–100]. As a consequence, the system is presently investigated as a potential process for deep CO removal from reformate gas [95, 247].

So far, no oscillations in PEMFCs with pure Pt electrodes were reported in the literature. However, autonomous potential oscillations have been found during elec-

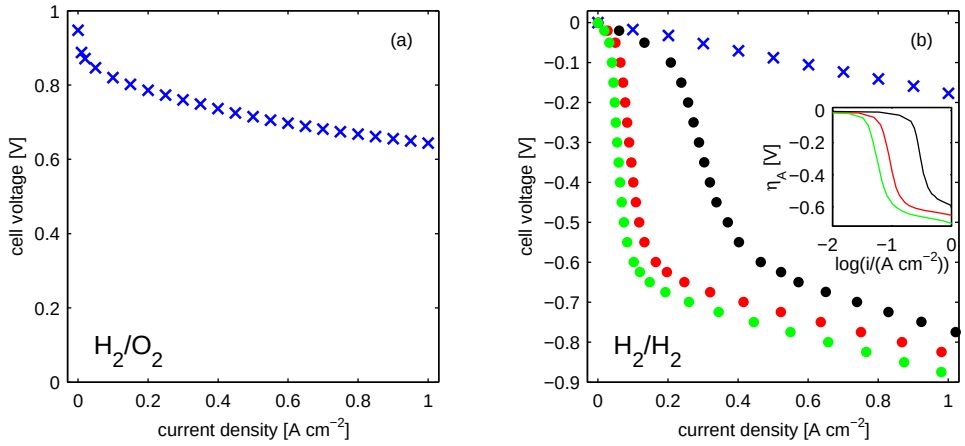

Figure 6.1: Polarisation curve of cell 1 in potentiostatic operation at 80°C (a) in H_2/O_2 operation without CO (b) in H_2/H_2 operation with different anode CO content (blue = no CO; black = 20 ppm CO; red = 100 ppm CO; green = 200 ppm CO). Inset in (b): Tafel plot of anode overpotential at different CO content.

trochemical H_2+CO oxidation in Pt rotating disc electrode (RDE) experiments (for an overview see [248]) and in 3-electrode experiments at Pt gas diffusion electrodes with H_2SO_4 electrolyte (independently by Deibert et al. [249] and Szpak [250]).

Since oscillations have been found in Pt model electrodes but not in technical Pt PEM fuel cells, in this section the possibility and conditions for the occurrence of oscillations is investigated. In the experiments, oscillations were found during galvanostatic operation when the Pt anode was poisoned with CO. The influence of CO content and cell temperature on the behaviour of the oscillations was investigated. Finally, the same fuel cell was operated in H_2/O_2 operation and oscillations were found, too.

Results and Discussion

In order to minimise degradation effects (as described in Chapter 2.1.1), two cells were used to investigate the influence of the CO mole fraction (Cell "1") and the temperature (Cell "2"). In Figure 6.1a the polarisation curve of cell 1 in H_2/O_2 operation is shown. Cathode activation losses can be seen in the low current density region followed by a linear voltage decrease caused by membrane and other ohmic resistances. In order to minimize the influence of the cathode, the cell was operated in H_2/H_2 operation. Respective polarisation curves are shown in Figure 6.1b. The open circuit voltage is

nearly 0 V. In the absence of CO, ohmic behaviour dominates the whole current range, i.e. activation losses are insignificant. The polarisation curves shown in Figure 6.1 clearly show that the intended experimental simplifications of no along-the-channel-distribution and negligible cathode overpotential are successfully achieved.

A first measurement series investigated the influence of CO content in the feed gas on the anode performance. The polarisation curves in potentiostatic operation (Figure 6.1b) show features well known from literature [207,208]. The typical S-shape profiles have especially been discussed by Camara et al. [209] and shall only briefly be sketched here for the case of 20 ppm CO. At low current densities a small voltage loss is observed. It is caused by the preferential adsorption of CO, which reduces the active area available for the hydrogen oxidation reaction (HOR). When the current is increased, a limiting current of the Tafel reaction is reached, apparent by the steep voltage decline. The anode overpotential increases, until the onset potential for the CO oxidation reaction is reached. The CO oxidation sets CO covered Pt sites free and increases the number of active sites available for the HOR. The equilibrium between CO and hydrogen oxidation decreases the curve slope into a mainly ohmic decrease, which is caused by membrane and ohmic resistances. At higher CO concentrations, the CO adsorption is accelerated, more active sites are blocked and the limiting current, at which the voltage decrease occurs, is lower. Additionally, the equilibrium between CO and hydrogen oxidation is shifted towards CO oxidation (i.e. higher overpotentials). The cell voltage levels off into a slightly lower plateau at high current densities.

When the polarisation curve under CO poisoning was measured galvanostatically instead of potentiostatically, potential oscillations began to arise once the current density exceeded a critical level. In Figure 6.2, measured time series of the cell voltage at different current densities are shown. With increasing current, the amplitude of the oscillations increased, the frequency of the oscillation decreased and the oscillations became more and more nonlinear (i.e. lost their sinusoidal shape). The oscillations are similar in shape and frequency to oscillations observed in PEMFCs with PtRu [244] and PtPd catalyst [100] and those found in three electrode measurements in H_2SO_4 solution at Pt electrodes [251] and Pt gas diffusion electrodes [249, 250] under CO poisoning.

In Figure 6.3 the polarisation curves of the anode overpotential (i.e. the difference between the cell voltage with and without CO poisoning) in potentiostatic and galvanostatic operation are compared. Both curves are identical up to the bifurcation point where the oscillations begin in galvanostatic operation. In the galvanostatic curve, the amplitude of the oscillations, i.e. the difference between minimum and maximum

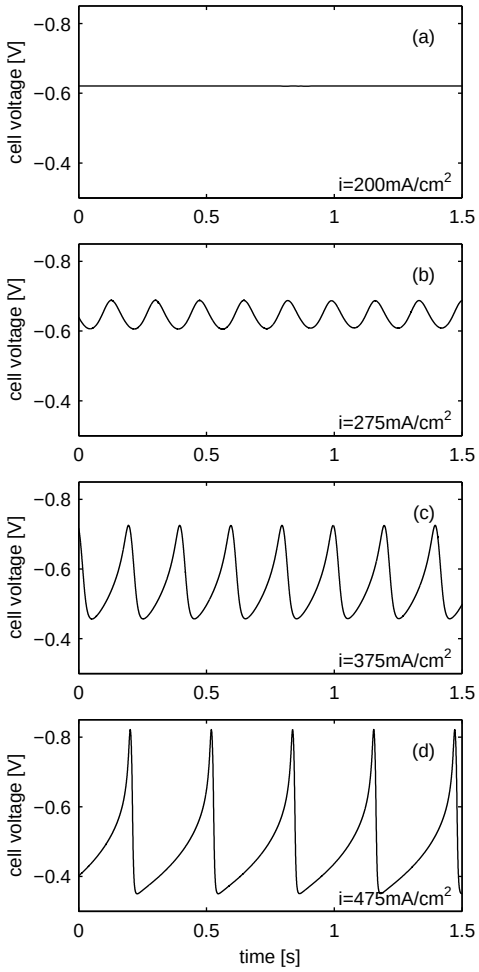

Figure 6.2: Time series of the cell voltage in H_2/H_2 operation with 100 ppm CO at 80°C. Current density of (a) 0.2 A cm^{-2} (b) 0.275 A cm^{-2} (c) 0.375 A cm^{-2} (d) 0.475 A cm^{-2}

.

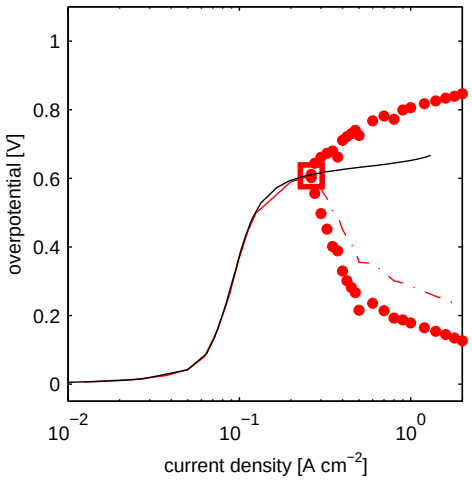

Figure 6.3: Anode overpotential in H_2/H_2 operation with 100 ppm CO at 80°C. Black line marks potentiostatic operation (non-oscillatory) and red lines mark galvanostatic operation (oscillatory); solid lines = stable part; □ = bifurcation point; • = min and max values of oscillations and dash-dotted line = mean value of oscillations.

overpotential, increases with increasing current density.

The influence of CO concentration on the galvanostatic polarisation curve and on the behaviour of the oscillations can be seen in Figure 6.4. With increasing CO concentration the bifurcation shifts to lower current densities and higher overpotentials due to the increased CO adsorption (Figure 6.4a).

In Figure 6.4b it can be seen that the fundamental frequency of the oscillations is high near the bifurcation point but decreases steeply until it reaches a nearly constant value at high current densities. With increased CO concentration, the oscillation frequencies are higher, both at the high frequency end near the bifurcation point and at the low frequency plateau at higher currents. This is caused by higher CO adsorption rates, which, according to the explanation of Hanke-Rauschenbach et al. [95], leads to shorter CO adsorption phases of the oscillation cycle.

In Figure 6.4c the distortion factor of the oscillation is shown. The distortion factor specifies the content of higher harmonics in the signal and is a simple measure for the nonlinearity of the oscillation. At the bifurcation point the distortion factor is 0, representing a nearly sinusoidal oscillation. When the current is increased the distortion factor increases, too (see time series in Figure 6.2 for comparison). The distortion factor increases more weakly with higher CO concentrations, i.e. the oscillations change more smoothly from the sinusoidal to a nonlinear shape, but converges to the same

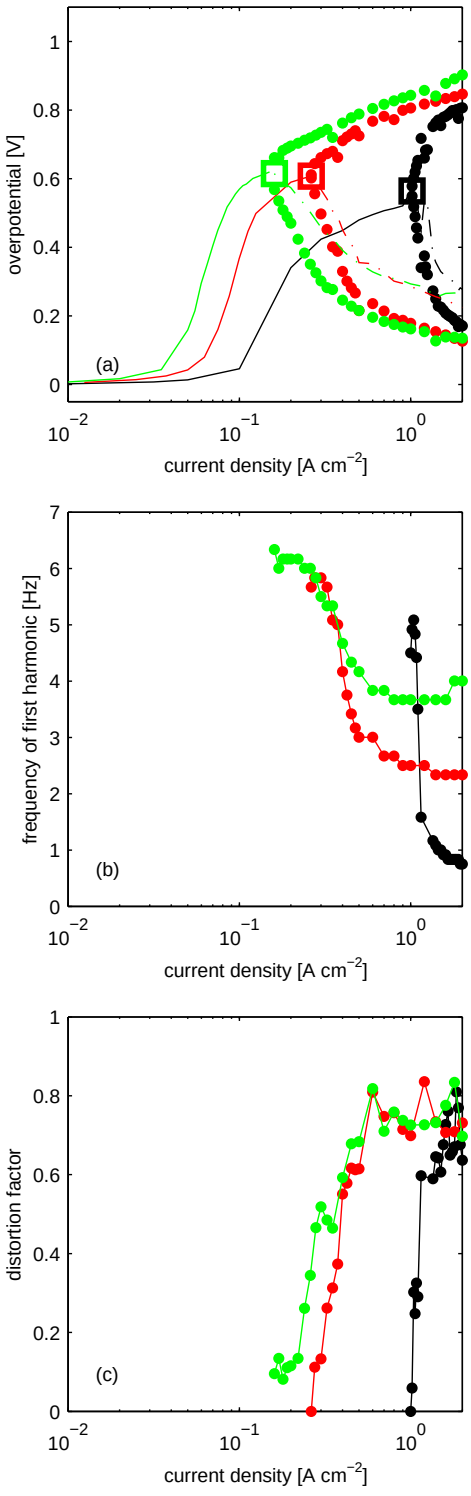

Figure 6.4: Influence of CO mole fraction (black = 20 ppm; red = 100 ppm; green = 200ppm) at 80°C: (a) galvanostatic bifurcation diagrams (solid line = stable part; □ = bifurcation point; ● = min and max value of oscillations; dash-dotted line = mean value of oscillations), (b) oscillation frequency, (c) distortion factor.

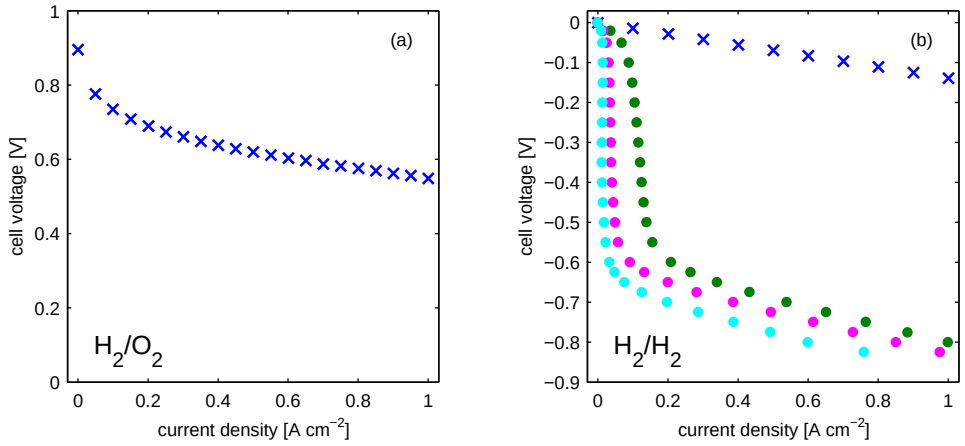

Figure 6.5: Polarisation curve of cell 2 (a) in H_2/O_2 operation without CO at 80°C (b) in H_2/H_2 operation at different cell temperatures (blue = no CO at 80°C; green = 100 ppm CO, 80°C; magenta = 100 ppm CO, 60°C; cyan = 100 ppm CO, 40°C)

maximum value for all CO concentrations.

In a second measurement series the influence of the operation temperature on the oscillation behaviour was investigated in cell 2. In this series, the CO concentration in the wet gas and the relative humidity were kept constant. In Figure 6.5 the potentiostatic polarisation curves in H_2/O_2 (a) and H_2/H_2 operation (b) are shown. In general, the limiting current of the Tafel reaction, at which the steep voltage decline occurs, decreases with declining temperature. This effect might be explained by the increased CO adsorption at lower temperatures [252], which leads to a higher blockage of the catalyst sites by CO.

In the galvanostatic operation in Figure 6.6, it can be seen that the current density at the bifurcation point declines with lower temperatures. In contrast, the overpotential at the bifurcation point does not significantly dependent on temperature. Therefore, the largest effect is the "shift" of the polarisation curves along the current axis due to the temperature dependent constants for CO and H_2 adsorption and hydrogen oxidation.

The frequencies of the oscillations grow with increasing temperature (Figure 6.6a). Following the argumentation of Zhang and Datta [244], the oscillation frequency f is proportional to an effective rate constant of a determining process. The temperature dependency of this effective rate constant (and with it the temperature dependency of the frequency) can be described with the Arrhenius equation:

$$f = C \exp\left(-\frac{E_a}{RT}\right) \tag{6.1}$$

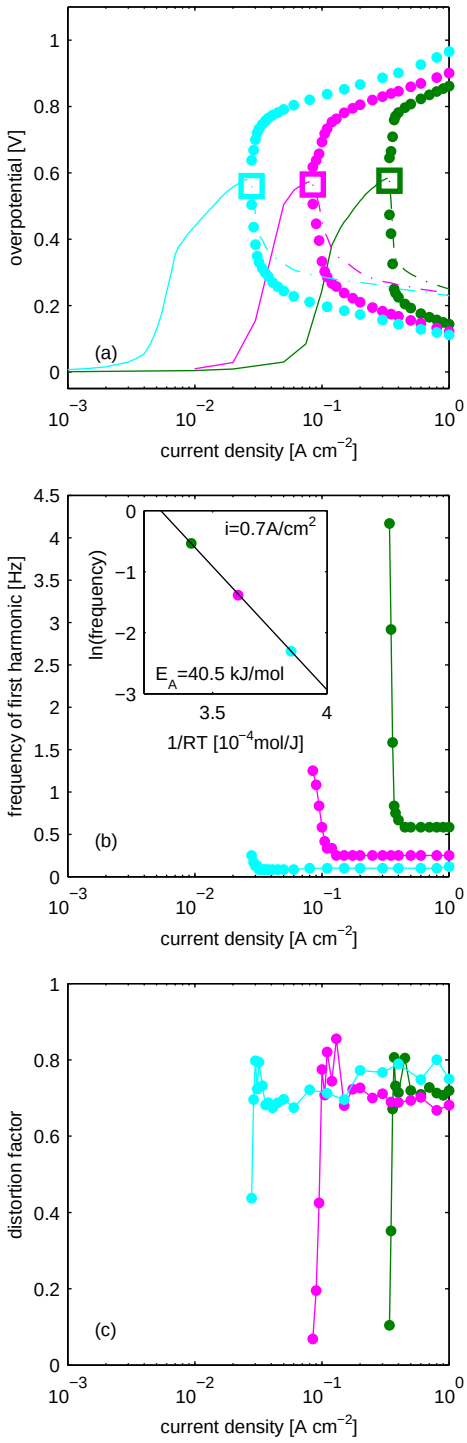

Figure 6.6: Influence of cell temperature (green = 80 °C; magenta = 60 °C; cyan = 40 °C) in H_2/H_2 operation with 100 ppm CO: (a) galvanostatic bifurcation diagrams (solid line = stable part, □ = bifurcation point, • = min and max value of oscillations, dash-dotted line = mean value of oscillations), (b) oscillation frequency, (c) distortion factor. Inset in (b): Arrhenius plot showing the temperature dependency of the oscillation frequency.

where C is an unknown pre-exponential factor and E_a is the activation energy. From the Arrhenius plot in Figure 6.6b the activation energy of 40.5±0.6 kJ mol^{-1} can be determined. This value for the Pt catalyst is smaller than the reported value of 60.9 kJ mol^{-1} for PtRu [244]. In order to relate this activation energy to a specific process each oscillation cycle is considered as consisting of two phases (as shown in [95]). In the first phase (marked by the long increase of overpotential) CO adsorbs on the catalyst, in the second phase (marked by an overshoot of η_{a} above the CO oxidation potential) CO is oxidised. As the overshoot takes only little time compared to the long potential increase (e.g. Figure 6.2d), it is reasonable to assume that CO adsorption determines the oscillation period and accordingly the frequency. During the first phase the CO coverage Θ_{CO} develops according to [10, 244]:

$$\frac{\mathrm{d}\Theta_{CO}}{\mathrm{d}t} = \frac{r_{\mathrm{CO,ad}}}{C_{cat}} \tag{6.2}$$

$$r_{\mathrm{CO,ad}} = k_{CO,ad}\Theta_0 x_{CO} p \tag{6.3}$$

where C_{cat} is the number of catalyst sites and $r_{CO,ad}$ and $k_{CO,ad}$ are the rate and rate constant of CO adsorption, respectively. With this, the time for the CO adsorption $t_{CO,ad}$ can be calculated. Therefore, Equation 6.3 is inserted into Equation 6.2 and the resulting equation is integrated from the minimum CO coverage $\Theta_{CO}^{\min}$ to the next maximum CO coverage $\Theta_{CO}^{\max}$. After permutation one achieves

$$\frac{1}{t_{CO,ad}} \approx f \approx \frac{k_{CO,ad}\left(T\right)\overline{\Theta_0}\left(T\right)x_{CO}p}{C_{cat}\left(\Theta_{CO}^{\max}\left(T\right)-\Theta_{CO}^{\min}\left(T\right)\right)} \tag{6.4}$$

where $\overline{\Theta_0}$ marks the average number of free surface sites. However, not only the constant for CO adsorption $k_{CO,ad}$ depends on temperature, but also $\overline{\Theta_0}$ and $\Theta_{CO}^{\max}-\Theta_{CO}^{\min}$. Consequently, the activation energy derived by the Arrhenius fit cannot be related to the CO adsorption constant alone. Nevertheless, Baschuk et al. found 47.3 kJ mol^{-1} for the activation energy of the CO adsorption at Pt electrodes [253], too.

Figure 6.6c shows that the change in the distortion factor is independent from temperature, it increases with comparable slope and reaches a unique limiting value at all temperatures.

After the discussion of the oscillation characteristics, the question remains why oscillations have never before been observed in fuel cells with a Pt catalyst. This paragraph tries to give an answer. First of all Figure 6.7 collects results of cell 2 during H_2/O_2 operation. It can be seen that the oscillations are indeed obtained in normal fuel cell operation. However, the Hopf bifurcation occurs at relatively small cell voltages (100 mV). In a cell with a less active cathode (or with fuel starvation) and a membrane

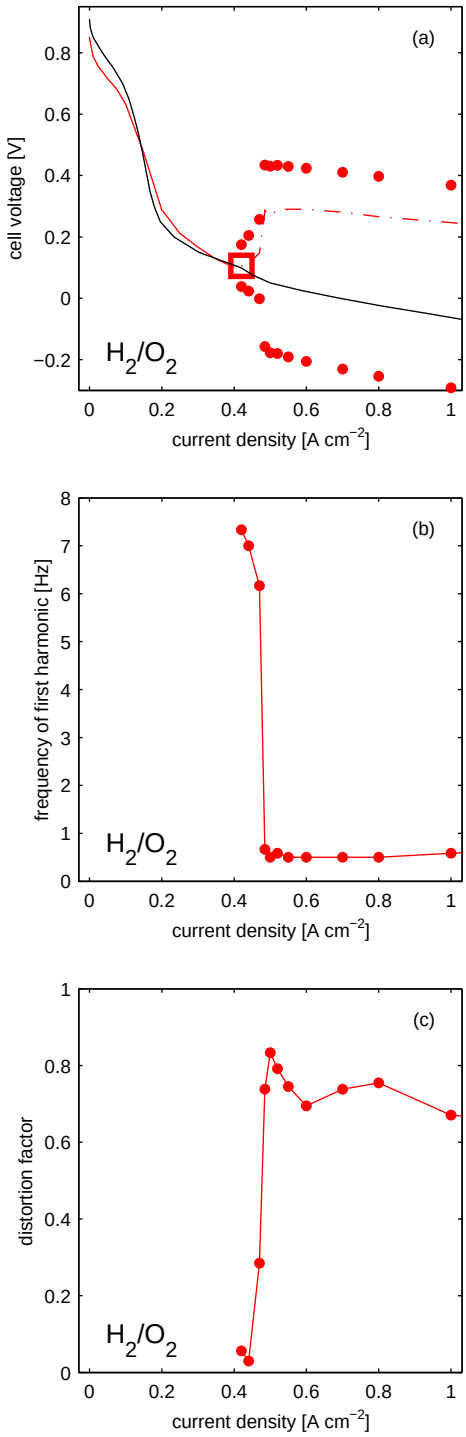

Figure 6.7: Oscillations in H_2/O_2 operation with 100 ppm CO at 80 °C: (a) galvanostatic bifurcation diagrams (black = potentiostatic; red = galvanostatic where solid line = stable part; □ = bifurcation point; ● = min and max value of oscillations; dash-dotted line = mean value of oscillations), (b) oscillation frequency, (c) distortion factor.

with higher resistance, the additional losses would push the Hopf bifurcation below the abscissa and accordingly out of the operation range of passive loads. Calculating the anode overpotential at the Hopf bifurcation in Figure 6.7a by subtracting other losses (Figure 6.5a), the anode overpotential is again approximately 600 mV (compare with Figure 6.6). Therefore, oscillations can only be found in Pt systems under passive load operation if losses additional to the anode overpotential are small.

As consequently expected, the characteristics of the oscillations are similar to previous characteristics obtained in the H_2/H_2 experiments (Figure 6.7b,c); starting from the bifurcation point the frequency of the oscillations decreases and the distortion factor increases, i.e. the oscillations change from sinusoidal to nonlinear shape.

Finally, some attention is paid to another interesting, yet not referenced feature. In the non-oscillating branch of some galvanostatic polarisation curves a change in Tafel-slope occurs at medium overpotentials ($\approx$350 mV; e.g. Figure 6.6). Comparable polarisation curves have been found earlier [210, 254–257] and are widely related to the occurrence of an additional, potential dependent H_2 adsorption mechanism, the so-called Heyrovský mechanism, at higher anode overpotentials. Dual-pathway kinetics, adding the Heyrovský mechanism to the HOR, were considered by Vilekar et al. [257] and seem to reproduce experimental results well.

However, some doubts related to this hypothesis remain as none of the potentiostatic polarisation curves exhibit a second Tafel slope (e.g. inset in Figure 6.1b). Despite the explanation of too few data points in order to resolve the effect, a second hypothesis might have the potential to explain the differences in potentiostatic and galvanostatic operation: in galvanostatic operation, there could in principal be a spatial anode overpotential distribution over the catalyst area (e.g. because of land-channel effects). This could lead to the formation of zones in which H_2 oxidation takes place (e.g. under the ribs) while other areas are still blocked by CO due to better transport (e.g. under the channel). In contrast, potentiostatic operation sets up a uniform distribution of the anode overpotential (as long as other losses are relatively small).

Additionally, a phenomenon known from conventional electrochemical three electrode experiments with liquid electrolyte might be responsible on first sight. Indeed, the formation of islands during CO electro-oxidation was observed in galvanostatic mode with the help of Fourier Transform Infra Red Spectroscopy (FTIRS) [258, 259]. Two distinct kinds of areas are present at the electrode. While one part of the surface was almost totally covered with CO, the other part of the surface was completely free of CO. However, such a clustering was observed only in the presence of an S-NDR instability, which requires a sufficient CO transport resistance. But compared to liq-

uid electrolytes, the gas phase transport in a PEMFC is several orders of magnitude greater due to higher diffusivities and dominant convective transport. Furthermore, the experiments were performed under very large flow rates, so that a transport resistance should be very small. Another inconsistency is that the formation of islands in liquid electrolytes has recently been found also in potentiostatic mode [260], which is not the case in the present work.

6.2 Experimental NFRA Spectra of a Differential H_2/H_2 Cell under CO Poisoning

In the previous section, the differential H_2/H_2 cell setup was validated and the anodic CO poisoning was preliminarily investigated in order to chose a suitable working point for the NFRA analysis in this section. Therefore, the steady-state behaviour of the cell under CO was analysed by polarisation curve measurements under potentiostatic (non-oscillatory) and galvanostatic (oscillatory) operation. Having understood the occurence and nature of the autonomous potential oscillations, the working point for the NFRA analysis could be chosen such that it lies relieably in the non-oscillatory region. This is necessary because otherwise the autonomous oscillations would interfere with the applied perturbation oscillation of the NFRA method. Additionally, the chosen working point lies in the low current region, where the limiting current for hydrogen oxidation is not yet reached but the active area for this reaction is decreased by preferential adsorption of CO. This scenario represents the case of beginning CO poisoning before severe performance decrease is reached and is highly relevant for diagnosis.

At this working point of 0.1 A cm^{-2}, EIS spectra were measured and are shown in Figure 6.8. In the Nyquist plot in Figure 6.8c it can be seen that the arc attributed to the Tafel Volmer reaction of hydrogen increases dramatically with increasing CO content. This increase in reaction resistance is caused by the decrease in active area available for the hydrogen oxidation reaction. This observation is in congruence with the experiments in Chapter 5.3 and with results from other groups [13, 199, 214, 215, 261, 262].

The measured NFRA spectra are shown in Figure 6.9. The first order frequency response function $H_{1,0}$ represents the linear behaviour of the cell. According to the mathematical background of the NFRA this function should be identical to the EIS spectra measured in the linear range with a small amplitude. This congruence is seen

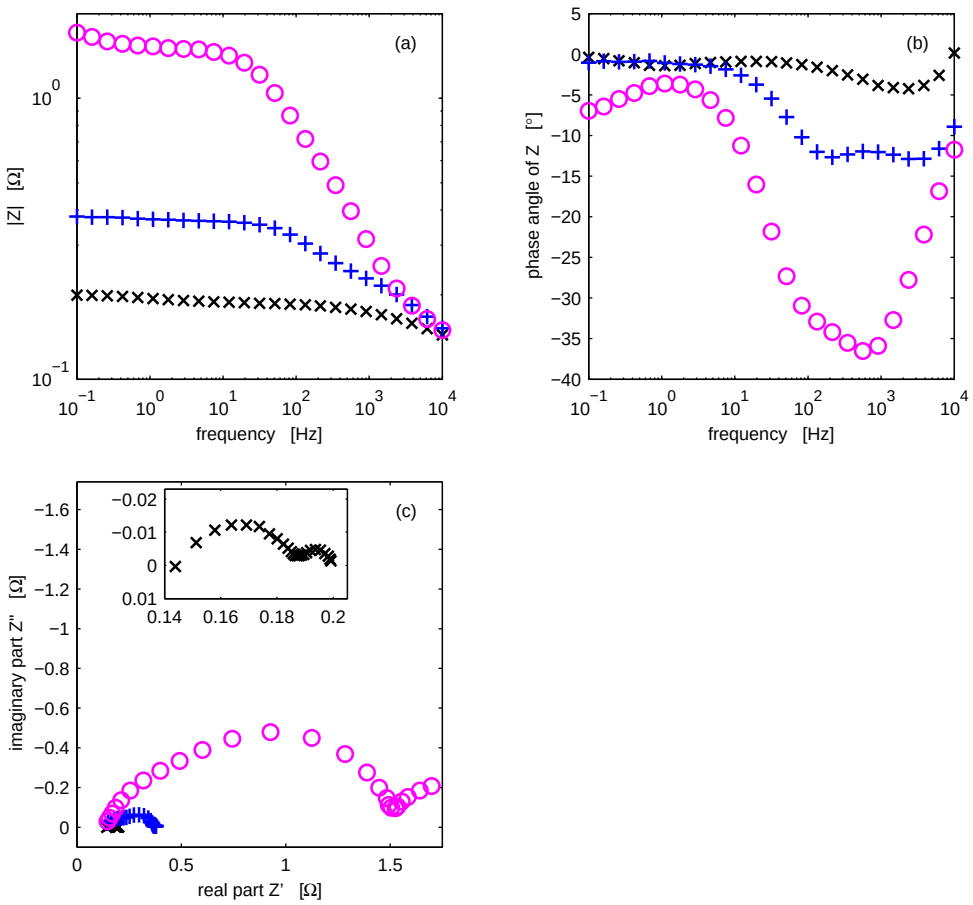

Figure 6.8: Measured EIS spectra in H_2/H_2 operation with various anode CO content ($\times$ = no CO, $+$ = 20 ppm CO, $\circ$ = 100 ppm CO). (a) Magnitude, (b) Phase angle, (c) Nyquist plot of Impedance, inset in (c) is a zoom of the spectrum without CO.

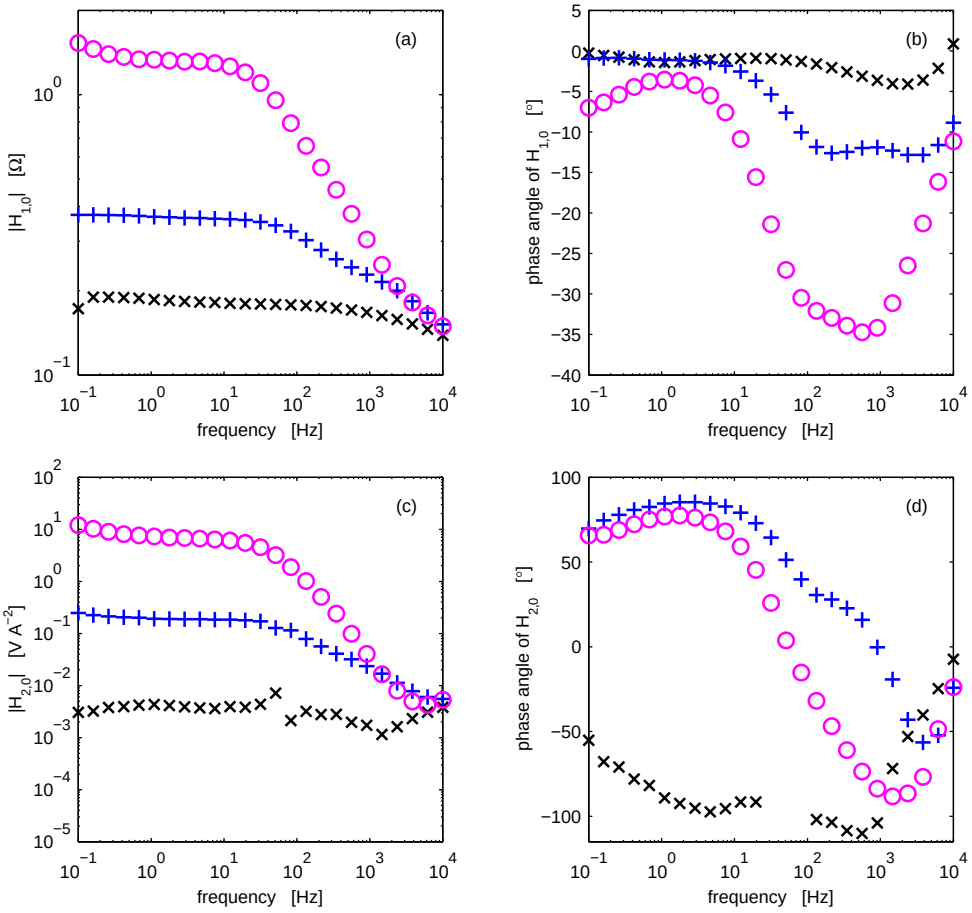

Figure 6.9: Measured NFRA spectra in H_2/H_2 operation with various anode CO content ($\times$ = no CO, $+$ = 20 ppm CO, $\circ$ = 100 ppm CO). (a) Magnitude of first order FRF $H_{1,0}$, (b) Phase angle of first order FRF $H_{1,0}$, (c) Magnitude of second order FRF $H_{2,0}$, (d) Phase angle of second order FRF $H_{2,0}$

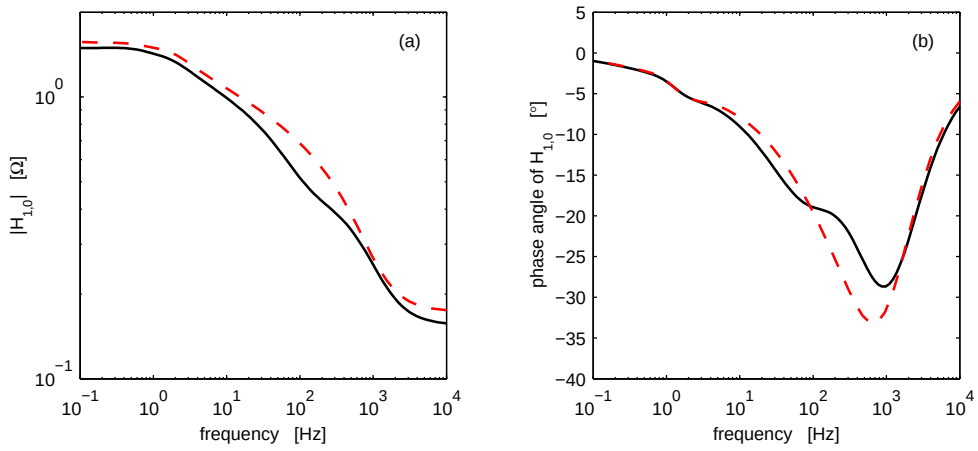

Figure 6.10: Comparison simulated NFRA spectra in H_2/H_2 operation with 100 ppm CO of the full model (solid line) and under the assumption of fast CO adsorption (dashed line). (a) Magnitude of first order FRF $H_{1,0}$, (b) Phase angle of first order FRF $H_{1,0}$

when comparing $H_{1,0}$ in Figures 6.9a+b with the EIS spectra in Figures 6.8a+b.

The $H_{1,0}$ spectrum of the H_2/H_2 cell without CO poisoning shows two time constants, which can be best identified in the Bode plot of the phase angle (Figure 6.9b). As has been discussed by Ciureanu et al. [13, 213, 263], the first time constant in the range of 1 s (f=1 Hz) can been attributed to the hydrogen chemisorption step of the Tafel Volmer mechanism. The second time constant lies in the range of 1 ms (f=1 kHz) and can be attributed to the oxidation of the chemisorbed hydrogen, i.e. the Volmer step.

In the $H_{1,0}$ spectra under CO poisoning the high frequency time constant of the Volmer mechanism splits up into two time constants. The time constant at the highest frequency is caused by the fast Volmer step on a CO covered surface. At this high frequency, slower steps like adsorption cannot follow the fast change of the input signal and the impedance is exclusively related to the electro-oxidation step on a surface at steady state CO coverage. But the change of the electrooxidation rate leads to a corresponding change in the surface coverage of hydrogen. When the frequency is decreased, the CO adsorption can follow this change in surface coverage. Thus, the hydrogen electro-oxidation reaction takes place on a periodically changing surface area. This effect leads to the second time constant in the spectra. This explanation can also be supported by simulations from the model wich will be explained in the next section. In Figure 6.10 the derivative of the CO coverage is set to zero in Equation 6.15, i.e. the

CO coverage is assumed to be fast and always in steady state. With this assumption, the second time constant disappears and both time constants merge into one.

In the spectrum of 100 ppm, an additional arc can be seen in the lower frequency end. This can be related to beginning CO oxidation, which frees the surface and a new equilibrium coverages can be reached. Since the reaching of the equilibrium coverage due to the competing hydrogen and CO adsorption is the slowest process, this arc is seen in the lower frequency range.

In addition to the linear spectra, the second order function $H_{2,0}$ contains information about the nonlinearities of the cell. In Figure 6.9c it can be seen that in the absence of CO the magnitude of $H_{2,0}$ is very low and not changing much. If the cell is poisoned by CO the magnitude increases in the low and middle frequency range. At high frequencies, the magnitude is decreasing and the decrease is steeper the higher the CO content is. The magnitude of the 100 ppm curve is even dropping below the 20 ppm curve. At the highest frequencies, all curves level off in the same limiting value. The phase angle of $H_{2,0}$ in Figure 6.9d shows a large change in the phase angle compared to the reference case without CO.

These features of the NFRA spectra might be used for a diagnosis of CO poisoning in PEMFCs. In case of CO poisoning, the first harmonic shows a significant increase in magnitude and an enlargement of the semicircle attributed to the charge transfer reaction. Unfortunately, the same feature is seen in the case of dehydration, too [217]. This is because in both cases the active area available for the hydrogen oxidation reaction decreases, either by blockage due to CO or by partly inactivation of the catalyst by drying out of the Nafion network in the catalyst layer. Therefore, the increase of the linear reaction impedance is a necessary but not sufficient condition for the presence of CO poisoning. For a sufficient distinction between CO poisoning and dehydration, the second harmonic $H_{2,0}$ might be used. In case of CO poisoning, the most remarkable qualitative and quantitative feature of $H_{2,0}$ is the change of the phase angle towards lower frequencies.

6.3 Modeling and Simulation of NFRA Spectra of a Differential H_2/H_2 Cell under CO Poisoning

In this section, the experimental approach and the measurement results of the previous section shall be verified. To do so, a simple and well established model is taken from literature with its original parameters [83]. Using this model, the higher order fre-

quency response functions are simulated and compared to the measurements. In these simulations, the original parameters were not changed or fitted in order to validate the NFRA method. Also, the model was kept as simple as possible, on the one hand in order to preserve the possibility of an analytical derivation of the higher order frequency response functions. On the other hand, the simplicity of the model leads to spectra in which the main mechanisms are clearly visible even though not every subprocess and intermediate step is represented in detail. Therefore, at the end of this chapter the model is reviewed critically and possibilities for refinement and extensions are given.

In this analysis a fuel cell with a differentially short channel length was used, in which along-the-channel distributions could be neglected. Therefore, the along-the-channel coordinate was neglected. Furthermore, the electrode was considered to be thin, mass transport resistances were neglected and isothermal conditions were assumed. Thus, a spatially lumped model was used. The cell voltage was calculated from anode and cathode overpotential and the voltage drop of the membrane. Anode and cathode overpotential were modelled with charge balance equations and reaction kinetics taken from literature [83]. The membrane was assumed to behave as an ohmic resistance.

Springer et al. [83, 207] suggested the following anode reaction scheme for a cell with CO poisoning:

$$H_2 + 2Pt \underset{b_{fh} \cdot k_{fh}(\Theta_{CO})}{\overset{k_{fh}(\Theta_{CO})}{\rightleftharpoons}} 2\,(H - Pt) \tag{6.5}$$

$$(H - Pt) \xrightarrow{k_{eh}} Pt + H^+ + e^- \tag{6.6}$$

$$CO + Pt \underset{b_{fc}(\Theta_{CO}) \cdot k_{fc}}{\overset{k_{fc}}{\rightleftharpoons}} CO - Pt \tag{6.7}$$

$$CO - Pt + H_2O \xrightarrow{k_{ec}} Pt + CO_2 + 2H^+ + 2e^- \tag{6.8}$$

At the cathode, the hydrogen reduction reaction takes place:

$$H^+ + e^- \quad \overset{k_{eh}}{\rightarrow} \quad 1/2\, H_2 \tag{6.9}$$

The electrical behaviour is described by charge balance equations for anode and cathode overpotential η_A and η_C, which are combined by Kirchhoff's voltage law to result in the cell voltage U_{cell}:

$$C_{dl,a}\frac{d\eta_a}{dt} = -F \cdot r_H^{ox} - F \cdot 2 \cdot r_{CO}^{ox} + \frac{i}{\epsilon} \tag{6.10}$$

$$C_{dl,c}\frac{d\eta_c}{dt} = F \cdot r_H^{red} - \frac{i}{\epsilon} \tag{6.11}$$

$$U_{cell} = -\eta_a + \eta_c - i \cdot R_m \tag{6.12}$$

where $C_{dl,a}$ and $C_{dl,c}$ are anodic and cathodic double layer capacity in F m_{act}^{-2}, r_H^{ox} and r_{CO}^{ox} are the reaction rates of hydrogen and CO oxidation per active area in mol m_{act}^{-2} s^{-1}. Therefore, the current i is also normalised to the active area of the cell by means of a roughness factor ϵ in m_{act}^2 m_{geom}^{-2}. By this normalisation, the model is independent of the internal active surface area, a value which could not be controlled exactly because of the inaccuracies of the preparation method. The original kinetic parameters of Springer [83] could be used with the help of the conversion equations in Table 6.2. The differences in active surface area between the current experiments and those of Springer were fixed by fitting the roughness factor ϵ in the model.

The membrane resistance R_m is determined from the relative humidity of the gases according to [64]:

$$R_m = \frac{d_m}{\kappa_m\left(a_{H_2O}\right)} = \frac{d_M}{1.3 \cdot 10^{-5} \exp\left(14 \cdot a_{H_2O}^{0.2}\right)} \tag{6.13}$$

where d_m is the thickness of the membrane and a_{H_2O} is the activity of the water vapour, i.e. the relative humidity as a value between 0 and 1.

The anode reaction kinetics are functions of the surface coverage of the platinum catalyst with hydrogen and carbon monoxide, Θ_H and Θ_{CO}. Material balances describe the temporal evolution of these surface coverages:

$$C_{cat}\frac{d\Theta_H}{dt} = r_H^{ads} - r_H^{des} - r_H^{ox} \tag{6.14}$$

$$C_{cat}\frac{d\Theta_{CO}}{dt} = r_{CO}^{ads} - r_{CO}^{des} - r_{CO}^{ox} \tag{6.15}$$

$$\Theta_{Pt} = 1 - \Theta_H - \Theta_{CO} \tag{6.16}$$

where ρ is the number of active reaction sites per geometric area in mol m_{act}^{-2} and $r_{H/CO}^{ads/des}$ are adsorption and desorption rates of hydrogen and carbon monoxide in mol m_{act}^{-2} s^{-1}. To describe the reaction rates at anode and cathode, Butler-Volmer kinetics with α=0.5 were assumed for hydrogen oxidation and Tafel kinetics were assumed for CO oxidation, according to [83]:

$$r_H^{ox} = \Theta_H k_{eh} 2 \sinh\left(\frac{\eta_a}{b_h}\right) \tag{6.17}$$

$$r_{CO}^{ox} = \Theta_{CO} k_{ec} \exp\left(\frac{\eta_a}{b_c}\right) \tag{6.18}$$

$$r_H^{red} = k_{eh} 2 \sinh\left(\frac{\eta_c}{b_h}\right) \tag{6.19}$$

where b_h and b_c are the Tafel slope for hydrogen and CO oxidation, respectively. The hydrogen adsorption can be described with a Langmuir isotherm [83,253]. The CO adsorption is described by a Temkin isotherm, according to [82, 264] and used in several modelling works [83, 253, 265].

$$r_H^{ads} = k_{fh} \cdot x_H \cdot p_a \cdot \Theta_{Pt}^2 \tag{6.20}$$

$$r_H^{des} = k_{fh} \cdot b_{fh} \cdot \Theta_H^2 \tag{6.21}$$

$$r_{CO}^{ads} = k_{fc} \cdot x_{CO} \cdot p_a \cdot \Theta_{Pt} \tag{6.22}$$

$$r_{CO}^{des} = k_{fc} \cdot b_{fc} \cdot \Theta_{CO} \tag{6.23}$$

where x_H and x_{CO} are the mole fraction of hydrogen gas and CO, p_a is the overall pressure of the anode. The CO adsorption-to-desorption ratio b_{fc} and hydrogen adsorption rate constant k_{fh} are a function of CO coverage [83]:

$$b_{fc}(\Theta_{CO}) = b_{fc0} \exp\left(\Theta_{CO} \frac{\delta(\Delta G_{CO})}{RT}\right) \tag{6.24}$$

$$k_{fh}(\Theta_{CO}) = k_{fh0} \exp\left[-\frac{\delta(\Delta E_H)}{RT}\left\{1 - \exp\left(-\frac{N_{ns}\,\Theta_{CO}}{1-\Theta_{CO}}\right)\right\}\right] \tag{6.25}$$

where $\delta(\Delta G_{CO})$ is the difference in adsorption free energy between Θ_{CO}=1 and Θ_{CO}=0; $\delta(\Delta E_H)$ is the increase of the activation energy for dissociative chemisorption of H_2 if the neighbouring Pt catalyst site is covered with CO; N_{ns} is the number of neighbouring Pt active sites. See Appendix B of [83] for further explanation and derivation of the Temkin adsorption behaviour.

The parameters used for the modelling are provided in Tables 6.1 and 6.2. The model has been implemented and solved in Matlab® Version 7.1.0.183. The NFRA spectra were simulated by Matlab® routines programmed in-house, which simulated

Table 6.1: General cell parameters used in the model

	used value	reference
a_{H_2O}	0.5445	
$C_{dl,a}$	984 $\cdot 10^{-6}$ F m_{act}^{-2}	fitted
$C_{dl,c}$	984 $\cdot 10^{-6}$ F m_{act}^{-2}	assumed
d_m	88.9$\cdot 10^{-6}$ m	
p_a	101325 Pa	
T	358 K	
C_{cat}	0.01042 mol m_{act}^{-2}	[265]
ϵ	0.663	fitted

Table 6.2: Kinetic parameters of Springer et al. [83] and conversions used (asterisk in the conversion equations marks the original values)

	used value	conversion	original value
b_c	0.06 V	no conversion	0.06 V
b_h	0.032 V	no conversion	0.032 V
b_{fc0}	1.53$\cdot 10^{-3}$ Pa	unit conversion	1.51$\cdot 10^{-8}$ atm
b_{fh}	5.0662$\cdot 10^{4}$ Pa	unit conversion	0.5 atm
k_{ec}	5.1821$\cdot 10^{-10}$ mol m_{act}^{-2} s^{-2}	$k_{ec} = k_{ec}^*/(\epsilon^* 2F)$	10^{-8} A cm^{-2}
k_{eh}	0.4146 mol m_{act}^{-2} s^{-2}	$k_{eh} = k_{eh}^*/(\epsilon^* F)$	4 A cm^{-2}
k_{fc}	1.0229$\cdot 10^{-5}$ mol m_{act}^{-2} s^{-2}	$k_{eh} = k_{eh}^*/(\epsilon^* F)$	10 A cm^{-2} atm^{-1}
k_{fh0}	4.0915$\cdot 10^{-3}$ mol m_{act}^{-2} s^{-2}	$k_{eh} = k_{eh}^*/(\epsilon^* F)$	4000 A cm^{-2} atm^{-1}
N_{ns}	5	no conversion	5
$\delta(\Delta G_{CO})/RT$	6.8	no conversion	6.8
$\delta(\Delta E_H)/RT$	4.6	no conversion	4.6

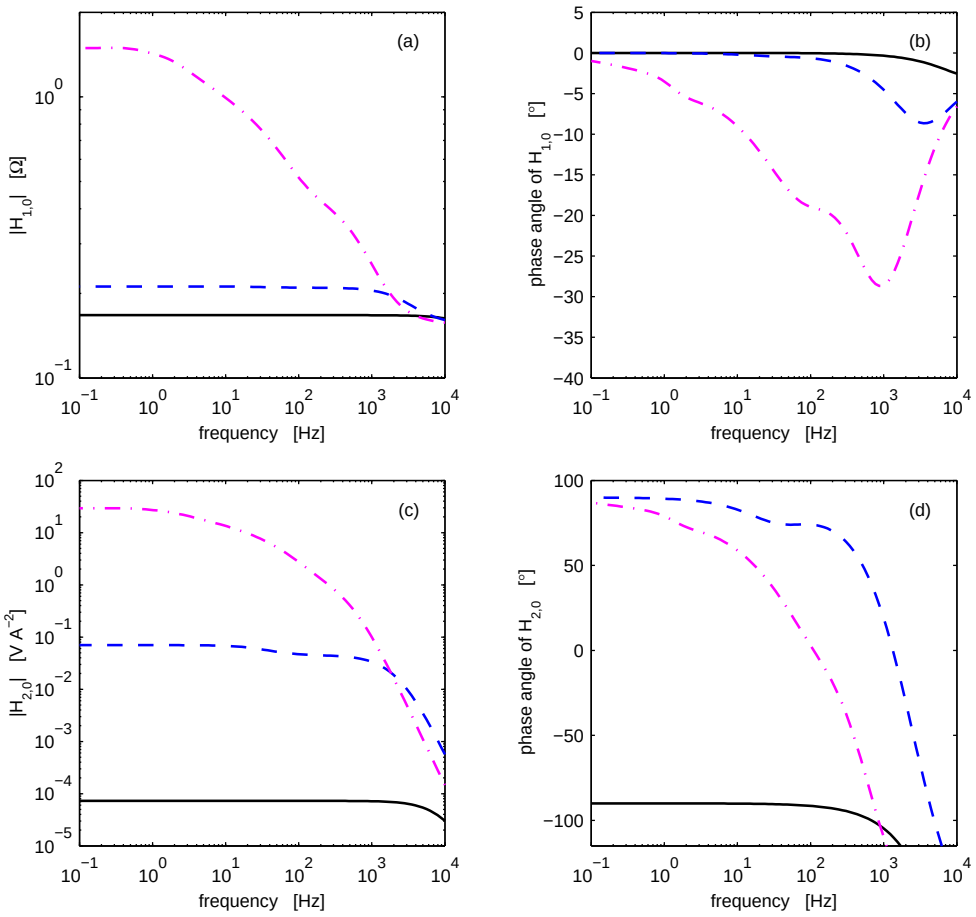

Figure 6.11: Simulated NFRA spectra in H_2/H_2 operation with various anode CO content (solid line = no CO, dashed line = 20 ppm CO, dash dotted line = 100 ppm CO). (a) Magnitude of first order FRF $H_{1,0}$, (b) Phase angle of first order FRF $H_{1,0}$, (c) Magnitude of second order FRF $H_{2,0}$, (d) Phase angle of second order FRF $H_{2,0}$

the quasi-frequency response and calculated the HFRF in the same fashion as in the experiments, according to Equations 3.27 and 3.28.

From Figure 6.11 it can be seen that the model describes the qualitative behaviour of the cell very well when compared to the measured spectra in Figure 6.9. This shows that the model is valid in the dynamic and nonlinear range and might be used to derive NFRA spectra at different operation conditions.

Because of the simplicity of the model, on the one hand the NFRA spectra can be determined numerically and a screening of parameters can be used to analyse the influence of each parameter or process on the NFRA spectra. On the other hand, an analytical solution of the NFRA spectra can be derived. These can be analysed

mathematically on the one hand to find out which parameters have a strong influence on the spectra and which are the governing processes. On the other hand, domains in the spectra can be found which are sensitive towards single processes. These domains might allow an unambiguous diagnosis of performance lowering processes.

Nevertheless, the model strongly simplifies the anode and cathode reactions. At the anode, the CO oxidation (Equation 6.8) is modelled as one overall electro-oxidation reaction via water, although several elementary steps could be possible [84, 96, 244, 266]:

$$CO - Pt + H_2O - Pt \rightarrow CO_2 + H_2 + 2Pt \tag{6.26}$$

$$CO - Pt + O - Pt \rightarrow CO_2 + H_2 + 2Pt \tag{6.27}$$

$$CO - Pt + OH - Pt \rightarrow CO_2 + H^+ + e^- + 2Pt \tag{6.28}$$

$$H_2O + Pt \rightleftharpoons OH - Pt + H^+ + e^- \tag{6.29}$$

Equation 6.27 describes the water-gas-shift (WGS) reaction, which might be neglected at low temperatures in PEMFCs. Equation 6.28 describes the direct oxidation of CO with oxygen either present in the fuel gas ("air-bleed") [84] or from diffusion from the cathode side through the membrane [244]. This reaction can be excluded because in the current experiments in H_2/H_2 operation no molecular oxygen is present. Therefore, the dominating reaction for CO oxidation is probably the electro-oxidation of CO with adsorbed OH (Equation 6.29) stemming from a water dissociation step (Equation 6.29) [267]. Note that although the water dissociation reaction (Equation 6.29) was originally proposed for PtRu catalyst, in Chapter 6.1 the analysis of autonomous oscillations showed that this step is also likely to take place at pure Pt in PEMFCs but at higher overpotentials (see also [10]).

Additionally, the hydrogen oxidation mechanism of the model might not be sufficient for all operation conditions. At high overpotentials the Heyrovský reaction [268], i.e. an electrochemical hydrogen adsorption step, is likely to take place [255]:

$$H_2 + Pt \rightarrow Pt - H + H^+ + e^- \tag{6.30}$$

This reaction becomes dominating when most of the surface is blocked by CO ($\Theta_{CO} > 0.6$ [256]) and the overpotential reaches high values. Nevertheless, the current measurements were carried out at low overpotentials in a scenario of beginning CO poisoning, as explained in Section 6.2. If the high potential region should be included, dual pathway kinetic models as suggested in Literature [255, 257] might be used.

The cathode is modeled in a very simple way in order to keep the model as simple

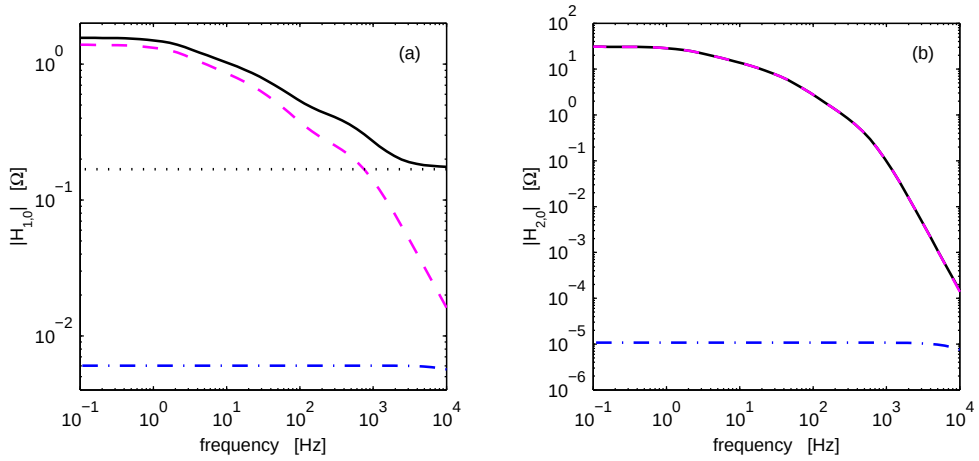

Figure 6.12: Simulated NFRA spectra at 0.1 A and 100ppm CO of the whole cell (grey), anode (dashed line), cathode (dash-dotted line) and membrane and ohmic resistances (dotted line). (a) Magnitude of first order FRF $H_{1,0}$ (logarithmic scale), (b) Magnitude of second order FRF $H_{2,0}$ (logarithmic scale). Note that in Figure (b) the spectra of the whole cell and of the anode overlap and that the values of the membrane and ohmic resistances are below 10^{-15}, i.e. in the range of numerical noise and practically zero.

as possible. Because of the large exchange current density of the cathodic hydrogen evolution reaction, the cathode can be seen as a pseudo-reference electrode of nearly constant potential [269]. Therefore, the cathode has no significant influence on the determined spectra. This can be additionally seen in Figure 6.12, where the fraction of anode, cathode and membrane on the first and second harmonic are shown; the fraction of the cathode on first and second harmonic are negligibly small.

6.4 Conclusions

In the previous chapter, it was found that electrochemical impedance is not always a sufficient indicator for the diagnosis of dehydration and CO poisoning in PEM fuel cells because there are operating conditions under which EIS spectra show similar and inconclusive behaviour. With the help of NFRA, these two cases could be discriminated by taking the nonlinear behaviour of the fuel cell into account in form of higher order frequency response functions. It could be seen that the second order function $H_{2,0}$ showed features which could be used for the discrimination. This result gave the motivation to investigate the influence of carbon monoxide on the NFRA spectra of a

PEMFC in a tailored experimental setup. Therefore, in this chapter a differential fuel cell design was used to avoid spatial distributions along the channel. H_2/H_2 operation eliminated the masking effect of the cathode and avoided possible sidereactions of molecular oxygen.

The advantages of this setup were demonstrated during investigations of the behaviour of a PEMFC with Pt anode under CO poisoning. In galvanostatic operation, potential oscillations were observed. These are known from literature to occur in PEMFCs with PtRu catalyst [244] but have not been observed in PEMFCs with Pt electrodes before. In order to elucidate this, detailed measurements were discussed in Section 6.1.

In a first measurement series, the influence of CO concentration on the behaviour of the oscillations was analysed. Higher CO concentrations were found to increase the oscillation frequency because of enhanced CO adsorption [95].

In a second measurement series, the influence of the cell temperature was investigated. By means of activation energy analysis, a different influence of the temperature on the oscillation frequency has been found for Pt catalyst (E_a = 40.5$\pm$0.6 kJ mol^{-1}) compared to the previously reported case at PtRu (E_a = 60.9 kJ mol^{-1}) [244]

Additionally, oscillations were found in H_2/O_2 operation, too. They occur if the anode overpotential is forced to increase until the onset potential for CO oxidation is reached. Nevertheless, in technical fuel cells operated with passive loads, the anode overpotential does usually not reach such high values, because a large fraction of the cell overpotential is caused by cathodic and ohmic losses.

As an additional side effect, an increase in Tafel slope at $\eta_A \approx 350$ mV was observed in some of the galvanostatic polarisation curves. Two hypotheses for the occurrence of a second Tafel slope were drawn: on the one hand, the Heyrovský mechanism could enhance hydrogen adsorption at higher overpotentials; on the other hand, spatial distributions of the overpotential could lead to local CO oxidation and thus to enhanced hydrogen oxidation in parts of the reactor (e.g. under the ribs, where CO transport could be diffusion limited).

After the analysis of the CO oscillations, a suitable working point for the intended NFRA measurement could be determined. A working point was found that lies reliably in the non-oscillatory region and simulates a scenario of beginning CO poisoning. At this working point, the influence of carbon monoxide on the NFRA spectra of a PEMFC was measured. The main features of the NFRA spectra during CO poisoning could be identified. Those features can be useful for the discriminate CO poisoning from other effects and will be used in Chapter 7.3 to develop a specific strategy for an unambiguous diagnosis.

Finally, the NFRA approach was complemented by a simplified model from literature [83]. Simulations using the original model parameters resulted in NFRA spectra in reasonably good agreement with the measured spectra. On the one hand, this comparison validated the experimental approach as well as the theoretical simplifications of the model. On the other hand the model was simple enough so that an analytical derivation of the NFRA spectra and a theoretical evaluation of these would be possible. Nevertheless, the model was reviewed critically and simplifications and limitations were explained and validated. Suggestions for refinement and extensions of the model were given.

Chapter 7

Dehydration Phenomena in the Differential H_2/H_2 Cell

After the detailed analysis of CO poisoning, in this chapter dehydration phenomena are investigated in the differential H_2/H_2 cell setup. The aim is to gain a complete and thorough understanding of the preliminary observations made in Chapter 5. Therefore, in the next section experimental NFRA spectra of the differential cell under dehydration are discussed. It is seen that dehydration does not only lead to an increase of the electrolyte resistance in the membrane as expected but also to a strong increase of the reaction resistance caused by the decreased proton conductivity in the catalyst layer. Modeling work described in Section 7.2 is used to obtain further understanding of the observed dehydration phenomena. Finally, the NFRA spectra of dehydration and CO are compared in Section 7.3 and key features which can be used as a "fingerprint" for diagnosis are identified.

7.1 Experimental Results

In the following, the experimental NFRA spectra, which were obtained with the differential H_2/H_2 cell described in Chapter 4.2, are presented and discussed. In Figure 7.1, the first order frequency response function $H_{1,0}$ measured at different fuel gas humidities is shown. $H_{1,0}$ represents the linear frequency response of the system and therefore is identical to the classic electrochemical impedance spectrum (EIS) [9, 217].

In principal, the EIS spectra of a differential H_2/H_2 cell consist of 2 arcs, which can be attributed to the hydrogen adsorption step (Tafel step) at low frequencies of about 1 Hz and to the charge transfer reaction (Volmer step) at high frequencies of several

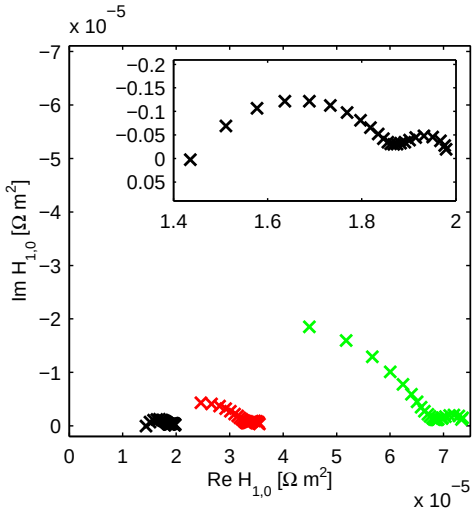

Figure 7.1: Nyquist plot of measured first order FRF $H_{1,0}$ at various gas humidification levels (black = 55% rh, red = 35% rh, green = 22% rh).

kHz, as discussed by Ciureanu et al. [13, 213, 263]. The high frequency limit of the impedance, i.e. the intersection of the Nyquist plot with the real axis, represents the sum of electrolyte and ohmic resistance of the cell [194].

The most expected change visible in the EIS spectra in Figure 7.1 is the increase of the electrolyte resistance, because the protonic resistance of the Nafion membrane strongly decreases at lower humidification of the fuel gas [41, 64, 270]. Nevertheless, the increase of the electrolyte resistance has only a minor impact compared to the strong increase of the charge transfer reaction resistance, which is visible as the diameter of the first arc of Nyquist plot in Figure 7.1. Additionally, the smaller low frequency arc of the Tafel step is slightly increasing. These changes are not intuitively understandable. A hypothesis is that dehydration leads to a strong decrease of the proton conductivity of the Nafion phase within the catalyst layer. With this, the protonic connection of the catalyst sites to the membrane is decreased. Especially active sites with a long protonic path to the membrane are affected and might become inactive. This effectively leads to a loss of the active area of the catalyst. Therefore, the charge transfer reaction resistance increases, which becomes visible in the EIS spectrum.

Because the increase of the reaction resistance is the most interesting feature, in the following all $H_{1,0}$ spectra will be shown in an iR-corrected form, in which the reaction resistance is better visible and directly comparable between different measurements. Additionally, iR-correction is typically used in EIS because the information

of the phase angle is more pronounced and better visible [193]. The iR-correction is calculated according to:

$$H_{1,0}^{iR-corrected}(\omega) \quad = \quad H_{1,0}^{measured}(\omega) - R_{\Omega} \tag{7.1}$$

where R_{Ω} is the sum of membrane and ohmic resistances. It is determined from the high frequency resistance of the impedance. Since R_{Ω} is a linear resistance, the iR-correction affects only the linear spectra of $H_{1,0}$ but does not influence the higher order spectra like $H_{2,0}$.

In Figures 7.2a–c the magnitude, phase angle and Nyquist plot of the iR corrected NFRA spectra of $H_{1,0}$ are shown. The key features caused by dehydration phenomena are the increase of the magnitude of $H_{1,0}$ over the whole frequency range and the increase of the reaction resistance visible in the Nyquist plot.

Next, the spectra of $H_{2,0}$ shown in Figures 7.2d–f are discussed. The magnitude of $H_{2,0}$ under dehydration (Figure 7.2d) shows an increase over the whole frequency range, while the phase angle (Figure 7.2e) increases in the low frequency range, is constant in the mid frequency and decreases slightly in the high frequency range. The plot of imaginary vs. real part of $H_{2,0}$ in Figure 7.2f shows a spiral in clockwise direction with increasing frequency through the fourth, third and second quadrant of the plot ending into the point of origin at high frequencies. The diameter of the spiral increases under dehydration conditions. Note that the data of $H_{2,0}$ are rather noisy, because the magnitude of $H_{2,0}$ is only small in all cases of dehydration.

7.2 Simulation of Dehydration Phenomena in the Catalyst Layer

In this section, a model is developed for describing the key features of the experimental NFRA spectra under dehydration operating conditions. The goal is to keep the model as simple as possible in order to be able to efficiently calculate the interesting NFRA spectra. As described in Chapter 6.3, a simple 0D Model was able to explain the key features of NFRA spectra under CO poisoning. This model was taken as the basis to describe the electrochemical hydrogen oxidation reaction and the hydrogen adsorption and desorption processes.

In order to model the observed main effect of dehydration, i.e. the increase of the reaction resistance as discussed in Section 7.1, the proton transport within the catalyst layer was included. This led to a 1D model with a spatial coordinate in sandwich

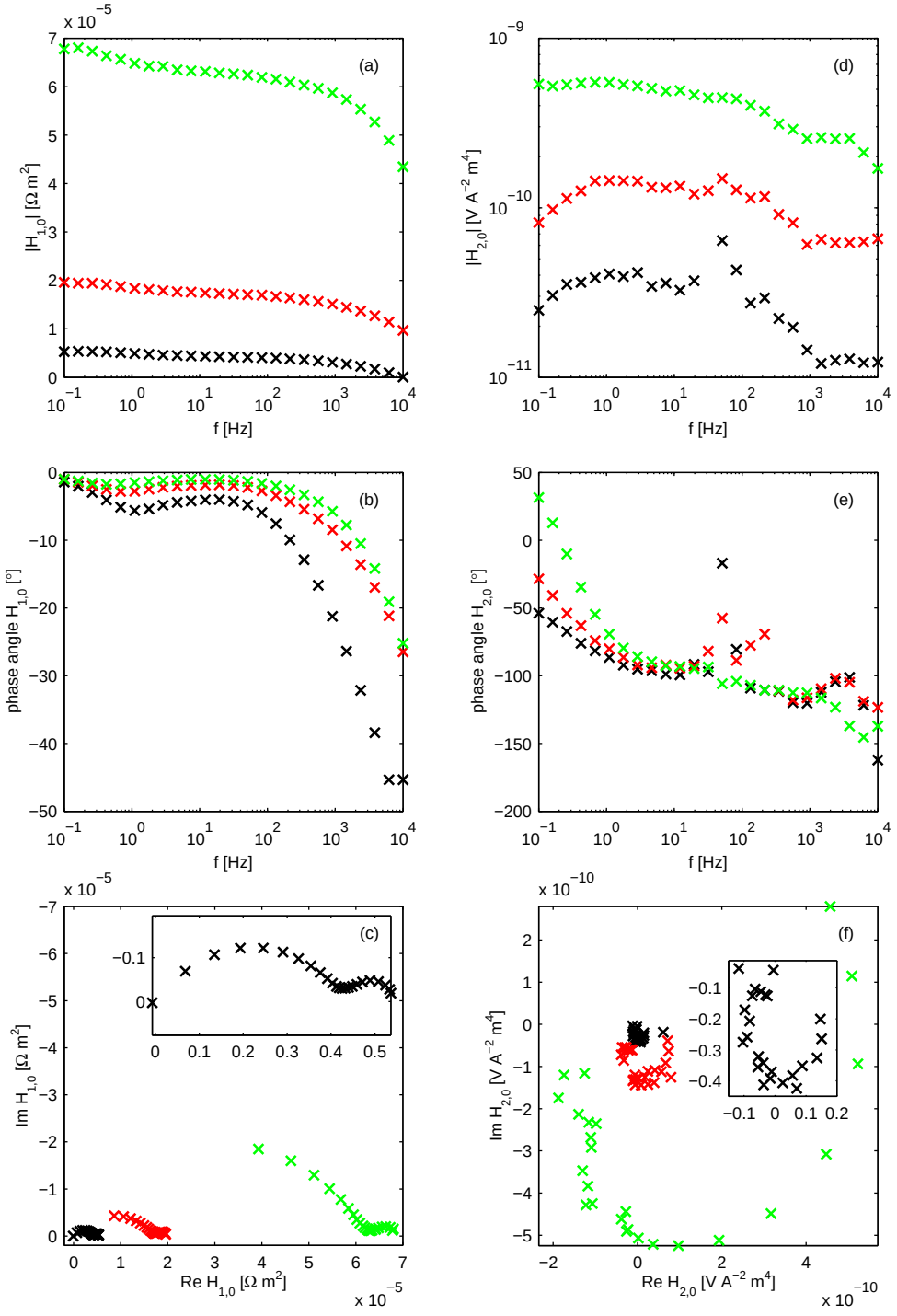

Figure 7.2: Experimental NFRA spectra at various gas humidification levels (black = 55% rh, red = 35% rh, green = 22% rh). (a)–(c) measured and iR corrected first order FRF $H_{1,0}$, (d)–(f) measured second order FRF $H_{2,0}$. (a)+(d) magnitude, (b)+(e) phase angle, (c)+(f) Nyquist plot.

direction. With this, the model is able to explain and reproduce the main processes leading to the key features of the NFRA spectra, although it is not a comprehensive fuel cell model.

Model Equations

In the following, the reaction scheme of the model will be explained. Anode charge balance equations for the electron and proton conducting phases and the electrochemical double layer are given. A surface material balance is necessary to describe the hydrogen adsorption and desorption processes. Subsequently, the kinetic equations for hydrogen oxidation, adsorption and desorption are given. Finally, the equations for cathode and membrane overpotential and the cell voltage are explained.

Springer et al. [83,207] suggested the following anode hydrogen oxidation reaction network:

$$\frac{1}{2}H_2 + Pt \underset{r_H^{des}}{\overset{r_H^{ads}}{\rightleftharpoons}} (H-Pt) \tag{7.2}$$

$$(H-Pt) \xrightarrow{r_H^{ox}} Pt + H^+ + e^- \tag{7.3}$$

where r_H^{ads}, r_H^{des} and r_H^{ox} are the rates of hydrogen adsorption, desorption and oxidation.

This reaction network consists of the potential independent hydrogen adsorption (Tafel reaction, Equation 7.2) and the subsequent hydrogen oxidation (Volmer reaction, Equation 7.3). These two reactions are known to describe the HOR well at small overpotentials. Nevertheless, at potentials above ≈100 mV a potential dependent hydrogen adsorption (Heyrovský reaction) becomes important [255, 257]:

$$H_2 + Pt \rightarrow Pt - H + H^+ + e^- \tag{7.4}$$

Such high anode overpotentials can be reached for example in case of CO poisoning with surface coverages higher than $\Theta_{CO} > 0.6$ [256]. However, the current analysis of dehydration without the presence of CO focuses on the low overpotential region, therefore the Heyrovský reaction is neglected. If necessary, it could be included using dual pathway kinetic models as suggested in [255, 257].

On the cathode, the hydrogen evolution reaction takes place:

$$H^+ + e^- \quad \overset{r_H^{red}}{\rightarrow} \quad \frac{1}{2} H_2 \tag{7.5}$$

Since it is known that the symmetry factor for the Volmer reaction is about 0.5, the rate constant for the backward reaction is assumed to have the same value as the forward reaction (Equation 7.3). Additionally, the hydrogen desorption step is neglected at the cathode, since the hydrogen desorption rate constant is about 1000 times higher than the hydrogen oxidation rate constant [83].

After the discussion of the reaction scheme, the anode balance equations for charges and materials shall be explained. The charge balance in the Nafion phase of the catalyst layer can be described under the assumption of electroneutrality as follows:

$$0 = -\frac{\partial}{\partial z} \underbrace{\left(-\kappa_l^{eff} \frac{\partial \phi_l}{\partial z} \right)}_{i_l} + a \cdot \iota \tag{7.6}$$

where ϕ_l is the potential in the Nafion phase, κ_l^{eff} is the effective conductivity of the Nafion phase in S m^{-1}, ι is the charge flux in A m$_{act}^{-2}$ and a is the internal active surface area in m$_{act}^2$ m^{-3}.

The boundary conditions to solve this equation under galvanostatic or potentiostatic operation are given by:

$$\left. \frac{\partial \phi_l}{\partial z} \right|_{z=0} = 0 \qquad \forall\, t \tag{7.7}$$

$$\left. -\kappa_l^{eff} \frac{\partial \phi_l}{\partial z} \right|_{z=L} = i_{cell}(t) \qquad \forall\, t \qquad (\text{galvanostatic}) \tag{7.8}$$

$$\phi_l(z = L, t) = \phi_{m,a}(t) \qquad \forall\, t \qquad (\text{potentiostatic}) \tag{7.9}$$

were i_{cell} is the cell current density in A m$_{geom}^{-2}$ and $\phi_{m,a}$ is the anode potential at the catalyst-membrane interface, i.e. the cell voltage minus the cathode and membrane overpotential.

The potential distribution inside the electron conducting phase is neglected, because of the high electronic conductivity compared to the protonic conductivity. A uniform potential is assumed:

$$\phi_s(z, t) = 0 \qquad \forall\, z, t \tag{7.10}$$

If the electron conducting phase shall be taken into account, the following formulation

might be used instead:

$$0 = -\frac{\partial}{\partial z}\underbrace{\left(-\kappa_s^{eff}\frac{\partial \phi_s}{\partial z}\right)}_{i_s} + a \cdot \iota \tag{7.11}$$

Boundary conditions:

$$\left.\frac{\partial \phi_s}{\partial z}\right|_{z=L} = 0 \qquad \forall\, t \tag{7.12}$$

$$\phi_s\,(z=0,t) = 0 \qquad \forall\, t \tag{7.13}$$

The charge balance for the anode double layer is given as:

$$C_{dl,a}\frac{\partial \Delta\phi_a}{\partial t} = \iota - F r_H^{ox} \tag{7.14}$$

with:

$$\phi_l = \phi_s - \Delta\phi_a \tag{7.15}$$

$$\eta_a = \Delta\phi_a - \Delta\phi_a^{0,ref} \tag{7.16}$$

where η_a is the anode overpotential in V and $C_{dl,a}$ is the double layer capacity in F m_{act}^{-2}.

Since the oxidation rate of hydrogen r_H^{ox} is dependent on the catalyst surface coverage Θ_H, a material balance for hydrogen is used to describe the coverage:

$$aC_{cat}\frac{\partial \Theta_H}{\partial t} = a\left(r_H^{ad} - r_H^{des} - r_H^{ox}\right) \tag{7.17}$$

There, the adsorption rate r_H^{ad} is dependent on the hydrogen concentration in the gas pores. Since the pore gas transport had no significant influence on the spectra, it was assumed to be fast. Therefore the hydrogen concentration in the gas pores was assumed to be identical with the bulk concentration in the channel:

$$c_{H_2}\,(z,t) = c_{H_2}^{\infty}\,(t) \qquad \forall\, z,t \tag{7.18}$$

Alternatively, a more rigorous mass transport model based on the Stefan-Maxwell approach can be used. Therefore, instead of assuming constant concentrations across the catalyst layer, Equation 7.18 can be replaced by:

$$\epsilon\frac{\partial c_{H2}}{\partial t} = -\epsilon\frac{\partial}{\partial z}g_{H2} + \sigma_{H2}a \tag{7.19}$$

with:

$$\sigma_{H2} = -(r_{H2}^{ads} - r_{H2}^{des}) \tag{7.20}$$

$$\tag{7.21}$$

Boundary condition:

$$g_{H2}(z = L, t) = 0 \qquad \forall\, t \tag{7.22}$$

$$c_{H2}(z = 0, t) = c_{H2}^{\infty} \qquad \forall\, t \tag{7.23}$$

The water concentration profile follows from:

$$c_{H_2O} = \frac{p}{RT} - c_{H_2} \tag{7.24}$$

The overall flux follows from the total mass balance (constant pressure and temperature is assumed):

$$0 = -\epsilon \frac{\partial}{\partial z} g_t + a\sigma_{H2} \tag{7.25}$$

Boundary condition:

$$g_t(z = L, t) = 0 \qquad \forall\, t \tag{7.26}$$

Maxwell-Stefan mass transport kinetics:

$$0 = -\frac{\partial x_{H2}}{\partial z} - \frac{x_{H_2O} g_{H2} - x_{H2} g_{H_2O}}{c_t D_{H2H_2O}^{eff}} \tag{7.27}$$

$$0 = \sum_{\alpha} g_\alpha - g_t \tag{7.28}$$

$$x_{H2} = c_{H2}/c_t \tag{7.29}$$

$$c_t = p/RT \tag{7.30}$$

This approach has been used to verify the previous assumption of fast mass transport in the gas pores.

For the hydrogen oxidation (Equation 7.3), a Butler-Volmer kinetic equation with $\alpha = 0.5$ was assumed according to [83]:

$$r_H^{ox} = \Theta_H k_{eh} 2 \sinh\left(\frac{\eta_a}{b_h}\right) \tag{7.31}$$

Note that the sinh formulation of Equation 7.31 is not an exact mathematical conversion of the Butler-Volmer equation:

$$r_H^{ox} = k_{eh}\left(\Theta_H \exp\left(\frac{\alpha n F}{RT}\eta_a\right) - b_{eh}\Theta_0 \exp\left(-\frac{(1-\alpha)\, nF}{RT}\eta_a\right)\right) \tag{7.32}$$

where an additional parameter b_{eh} would be necessary. To avoid this, the hyperbolic sine is used as an approximation (similar to the Tafel equation). With the sinh, an error in the second term is made, i.e. the backward reaction is taken into account with a wrong prefactor of Θ_H, a value between 0 and 1. Therefore, the error is between

0 and 100% of the backward reaction, which is a better approximation than the Tafel equation, which always neglects the backward reaction to 100%. An additional advantageous qualitative feature is that the sinh function is zero at zero overpotential, whereas the Tafel equation gives a current flow even at zero overpotential.

The hydrogen adsorption and desorption rates can be described with a Langmuir isotherm [83, 253]:

$$r_H^{ads} = k_{fh} \cdot c_{H_2} \cdot RT \cdot (1 - \Theta_H)^2 \tag{7.33}$$

$$r_H^{des} = k_{fh} \cdot b_{fh} \cdot \Theta_H^2 \tag{7.34}$$

Since the focus of the current work lies on the anode processes, the cathode is modelled in a very simple way in order to keep the model as simple as possible. Because of the large exchange current density of the cathodic hydrogen evolution reaction, the cathode can be seen as a pseudo-reference electrode of nearly constant potential [269]. Therefore, the cathode has no significant influence on the determined spectra. A charge balance is used to describe the electrical behaviour:

$$C_{dl,c}\frac{d\Delta\phi_c}{dt} = \frac{-i_{cell}}{a \cdot L_c} + F r_H^{red} \tag{7.35}$$

where L_c is the thickness of the cathode catalyst layer. The hydrogen reduction rate is described with a Butler-Volmer equation similar to the anode, but under the assumption that the hydrogen desorption step is fast and negligible compared to the reaction step. Therefore, the concentration dependence is neglected. Note that in this case the Butler-Volmer equation can be mathematically correctly combined to the sinh function:

$$r_H^{red} = k_{eh} 2 \sinh\left(\frac{\eta_c}{b_h}\right) \tag{7.36}$$

$$\eta_c = \Delta\phi_c - \Delta\phi_c^{0,ref} \tag{7.37}$$

The membrane voltage drop is described by the membrane conductivity according to [64]:

$$\Delta\phi_m = \frac{d_m}{\kappa_m} i_{cell} \tag{7.38}$$

$$\kappa_m = 1.3 \times 10^{-5} \exp\left(14 \cdot {a_{H_2O}}^{0.2}\right) \tag{7.39}$$

With this, the cell voltage can be calculated from the anode, cathode and membrane overpotential:

$$\begin{aligned} U_{cell} &= \Delta\phi_c - \Delta\phi_m - \Delta\phi_a \\ &= \Delta\phi_c - \Delta\phi_m - (0 - \phi_{m,a}) \end{aligned} \tag{7.40}$$

Table 7.1: Kinetic parameters of Springer et al. [83] and conversions used (asterisk in the conversion equations marks the original values)

	used value	conversion	original value
b_c	0.06 V	no conversion	0.06 V
b_h	0.032 V	no conversion	0.032 V
b_{fc0}	1.53×10^{-3} Pa	unit conversion	1.51×10^{-8} atm
b_{fh}	5.0662×10^{4} Pa	unit conversion	0.5 atm
k_{ec}	5.1821×10^{-10} mol m_{act}^{-2} s^{-2}	$k_{ec} = k_{ec}^*/(\epsilon^* 2F)$	10^{-8} A cm^{-2}
k_{eh}	0.4146 mol m_{act}^{-2} s^{-2}	$k_{eh} = k_{eh}^*/(\epsilon^* F)$	4 A cm^{-2}
k_{fc}	1.0229×10^{-5} mol m_{act}^{-2} s^{-2}	$k_{eh} = k_{eh}^*/(\epsilon^* F)$	10 A cm^{-2} atm^{-1}
k_{fh0}	4.0915×10^{-3} mol m_{act}^{-2} s^{-2}	$k_{eh} = k_{eh}^*/(\epsilon^* F)$	4000 A cm^{-2} atm^{-1}
p	5	no conversion	5
$\delta(\Delta G_{CO})/RT$	6.8	no conversion	6.8
$\delta(\Delta E_H)/RT$	4.6	no conversion	4.6
w_{Nafion}	0.1	according to preparation	
ϵ	0.7	assumed	
τ	2	[271]	

Model Results

In Figure 7.3 numerical simulations of NFRA spectra with the original parameter set of Springer et al. [83], summarised in Table 7.1, are shown. In these simulations, the effective proton conductivity of the polymer phase in the catalyst layer κ_l^{eff} was calculated from the protonic conductivity of bulk Nafion according to Equation (7.39), as well as from the Nafion content of the catalyst w_{Nafion}, the porosity of the catalyst layer ϵ and the tortuosity factor τ:

$$\kappa_l^{eff} = \kappa_m w_{Nafion}(1-\epsilon)/\tau \tag{7.41}$$

With this parameter set, the model is able to describe the key features of dehydration qualitatively well, although a further parameter refinement as discussed later is necessary for a quantitative agreement of experiments and simulation. In Figures 7.3a–c the linear $H_{1,0}$ spectra under dehydration are shown. The key feature is the increase of the reaction resistance, visible as increasing diameter of the Nyquist plot in Figure 7.3c and as increase of the magnitude of $H_{1,0}$ (Figure 7.3a) in the whole frequency range.

Additionally, the key features of the second order FRF $H_{2,0}$ under dehydration are described by the model as well. The magnitude is increasing over the whole frequency range (Figure 7.3d) and the phase angle changes in the high frequency region from

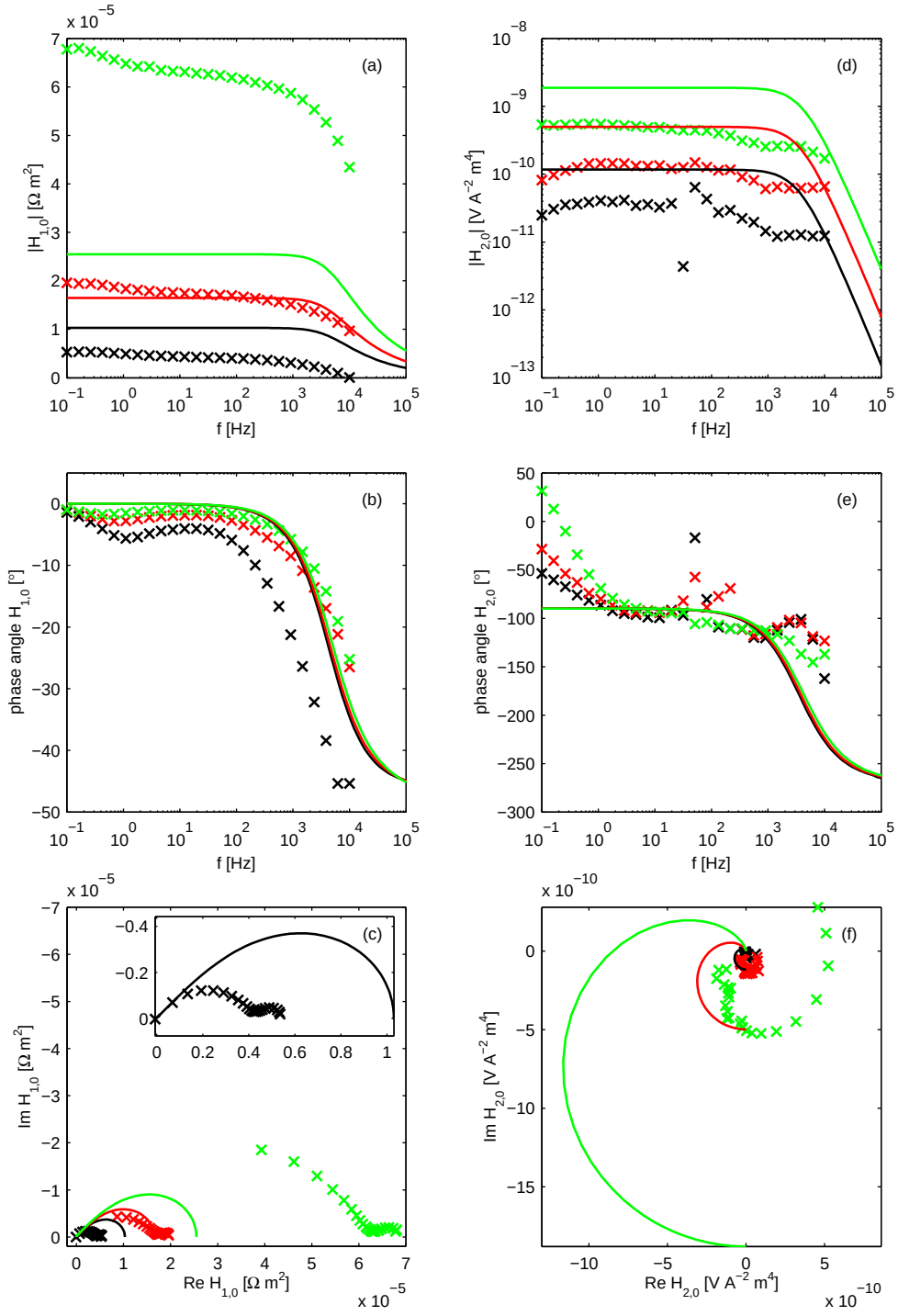

Figure 7.3: Simulated and iR corrected NFRA spectra with the original parameter set given in Table 6.1 at various gas humidification levels (black = 55% rh, red = 35% rh, green = 22% rh). (a)–(c) first order FRF $H_{1,0}$, (d)–(f) second order FRF $H_{2,0}$. (a)+(d) magnitude, (b)+(e) phase angle, (c)+(f) Nyquist plot, i.e. imaginary part vs. real part. Inset in (c) is a zoom of the spectrum at 55% rh.

Table 7.2: Fitting factors for dehydration

parameter	70 °C	60 °C	50 °C
$C_{cat}\,[pre-factor]$	1.5	15	700
$k_{fh}[pre-factor]$	2.05×10^{-4}	1.7×10^{-3}	4.0×10^{-2}

-90° to -270° (Figure 7.3e). Thus, the model describes the high frequency end of the Nyquist plot of $H_{2,0}$ (Figure 7.3f) well, i.e. the path of the spiral through the third and second quadrant into the point of origin.

As mentioned, the model quantitatively underestimates the increase of the reaction resistance (compare Figure 7.3c and 7.2c). This might be caused by neglecting the water transport in the polymer phase of the catalyst layer, which would lead to an additional dehydration of the Nafion network and to a distribution of the protonic conductivity. This would result in a much smaller effective protonic conductivity κ_l^{eff} than estimated with Equations (7.39) and (7.41).

A first attempt to fix this problem was done by fitting the value of κ_l^{eff} (see Figure 7.4). Therefore, κ_l^{eff} was multiplied by a fitting factor of 7, 0.35 and 0.085 for the cases of 55% rh, 35% rh and 22% rh, respectively. Thus, the model provides the correct diameter of the Nyquist plot of $H_{1,0}$ (Figure 7.4a) and the magnitude of $H_{1,0}$ is fitted well in the mid to high frequency region (Figure 7.4a). $H_{2,0}$ does not change qualitatively, but fits quantitatively better in the case of high and medium hydration (see Figure 7.4d–e), i.e. 55% rh and 35% rh respectively.

Additionally, there is a small misestimation of the hydrogen adsorption rate constant k_{fh} in the original parameter set. The hydrogen adsorption step is visible as the additional small arc in the Nyquist plot of $H_{1,0}$ (Figure 7.2c) and the path of the $H_{2,0}$ spiral (Figure 7.2f) from 0° to -90°. In the original model, were anodic CO poisoning is included, k_{fh} is dependent on the CO coverage (Temkin isotherm). In the presence of CO, the value of k_{fh} decreases strongly. This decrease might be slightly overestimated, which is counterbalanced by a very high initial value of k_{fh} in the absence of CO.

To illustrate this aspect, in Figure 7.5, a NFRA spectrum with fitted k_{fh} value is shown exemplarily for the case of high dehydration (22% rh). Note that a change of k_{fh}, i.e. a decrease of the hydrogen adsorption rate constant, has to be counterbalanced by the corresponding dynamic parameters in order to keep the time constants of the processes constant. Therefore, the fit of k_{fh} led to the parameter set shown in Table 7.2. When k_{fh} is adjusted, the second arc in the linear spectrum of $H_{1,0}$ is mod-

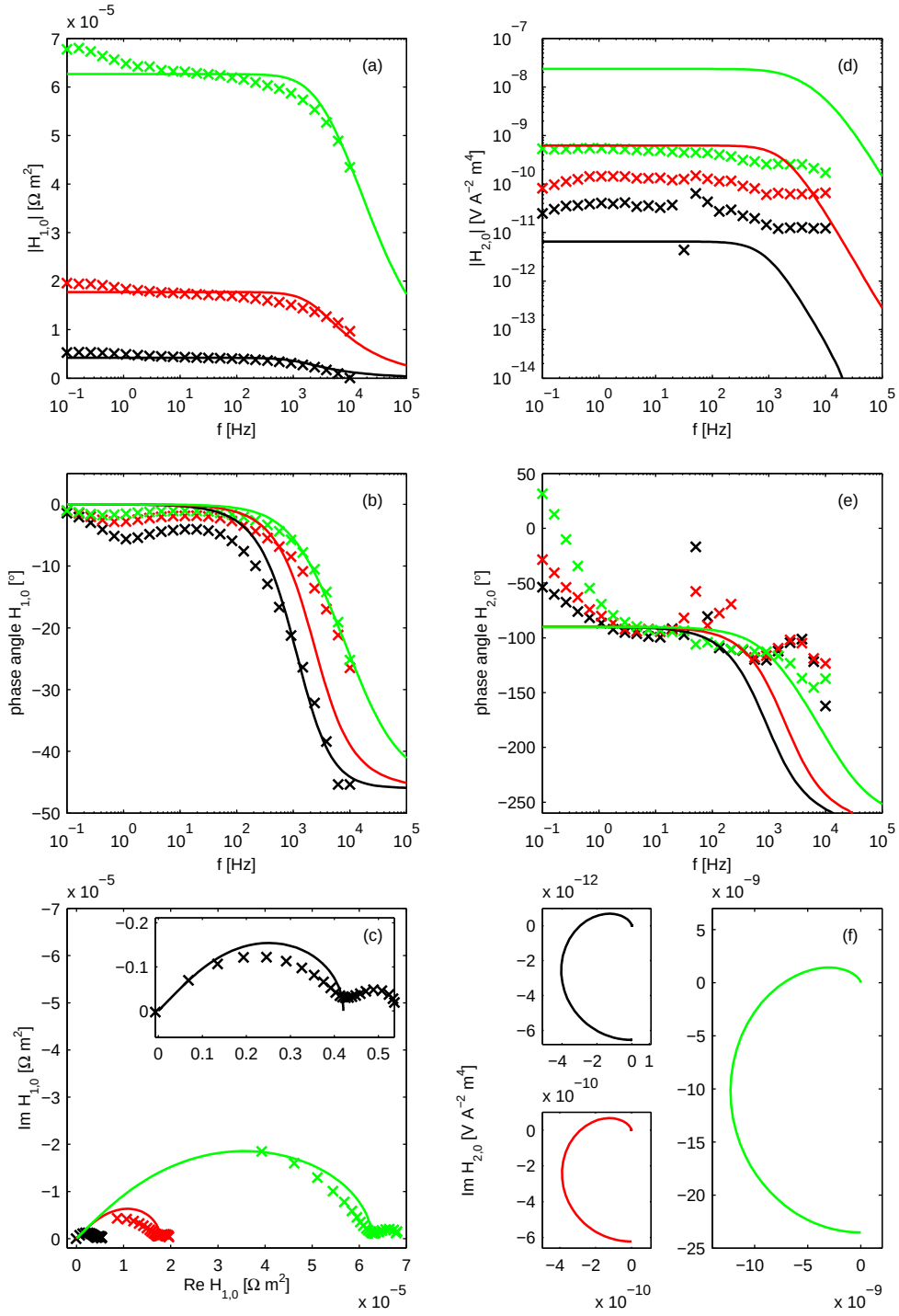

Figure 7.4: NFRA spectra with fitted κ_l^{eff} at various gas humidification levels (black = 55% rh, red = 35% rh, green = 22% rh). (a)-(c) Fitted and iR corrected first order FRF $H_{1,0}$, (d)-(f) fitted second order FRF $H_{2,0}$. (a)+(d) magnitude, (b)+(e) phase angle, (c)+(f) Nyquist plot. Inset in (c)+(f) is a zoom of the spectrum at 55% rh.

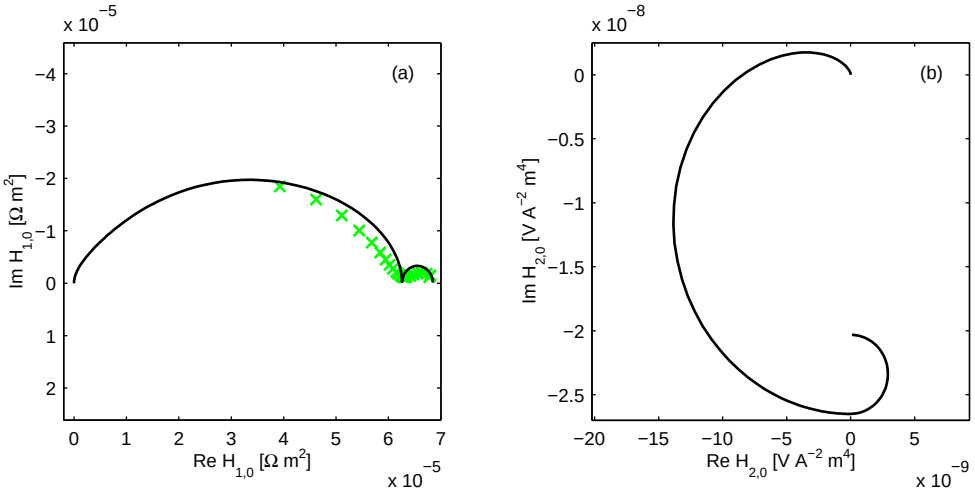

Figure 7.5: Simulated NFRA spectra at dehydration (22% rh) with fitted κ_l^{eff} and fitted k_{fh} . (a) Nyquist plot of iR corrected first order FRF $H_{1,0}$, (b) Nyquist plot of second order FRF $H_{2,0}$

eled well and magnitude and phase of $H_{1,0}$ fit well in the low frequency region (see Figure 7.5a). With the adjustment of k_{fh} also $H_{2,0}$ is described qualitatively better (see Figure 7.5b), because the spiral is extended in the low frequency region with a 90° turn through the fourth quadrant of the Nyquist plot. Although the magnitude of this additional turn does not fit quantitatively, it is qualitatively better described. Adjustment of additional parameters and the inclusion of water transport in the catalyst layer would probably lead to a quantitative improvement. To do so, the determination of additional parameters from further experiments would be necessary.

7.3 Comparison of Key Features of NFRA Spectra under CO Poisoning and Dehydration

For sake of completeness, the measurements of NFRA spectra of the H_2/H_2 cell under CO poisoning from Chapter 6.2 were iR-corrected and are shown in Figure 7.6. The linear spectra of $H_{1,0}$ show an increase in magnitude over the whole frequency range and an increase of the reaction resistance in the Nyquist plot, similar to the spectrum under dehydration. A slight difference to the spectra under dehydration is the splitting of the high frequency arc of the hydrogen oxidation reaction into two arcs with slightly different time constants. The additional time constant also becomes visible in the plot

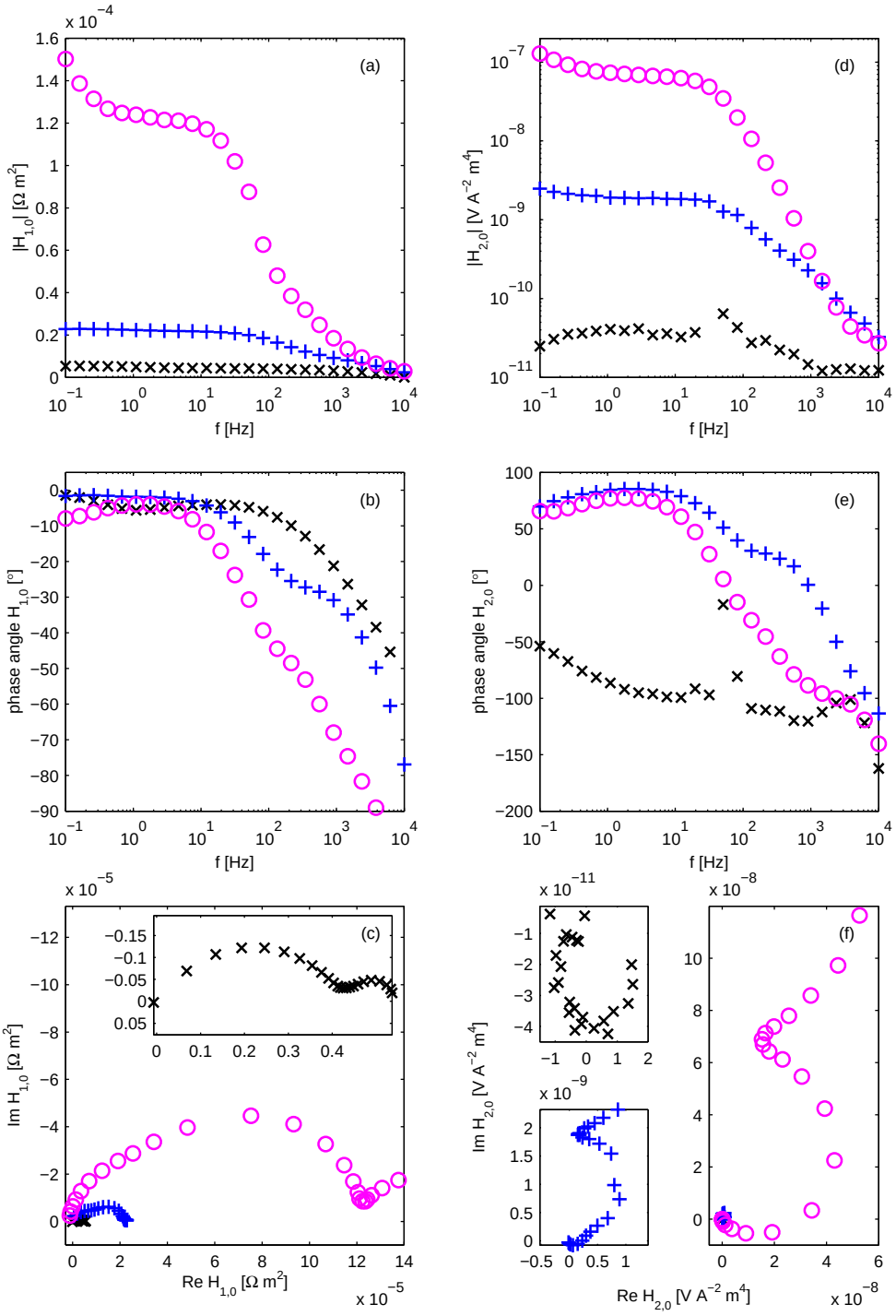

Figure 7.6: Measured and iR corrected NFRA spectra at various anode CO content (black = 0 ppm CO, blue = 20 ppm CO, magenta = 100 ppm CO) and constant relative humidity of 55% rh. (a)–(c) iR corrected first order FRF $H_{1,0}$, (d)–(f) second order FRF $H_{2,0}$. (a)+(d) magnitude, (b)+(e) phase angle, (c)+(f) Nyquist plot.

of the iR-corrected phase plot (Figure 7.6b), where a slight plateau occurs. The first time constant at high frequencies can be attributed to the HOR taking place at surface under steady-state CO coverage. The second time constant at lower frequencies corresponds to the HOR taking place at a surface with dynamically changing CO coverage. This hypothesis was supported by modeling work in Chapter 6.3. However, the two time constants are very close to each other and are barely visible in the spectra because they strongly merge into each other. Therefore, this feature is very difficult to use for diagnosis.

Nevertheless, the second order frequency response function $H_{2,0}$ shows additional features, which might be useful for the discrimination between CO poisoning and dehydration. The magnitude of $H_{2,0}$ in Figure 7.6d increases over the whole frequency range, qualitatively similar to the case of dehydration. However, the quantitative increase of the magnitude of $H_{2,0}$ in relation to the magnitude of $H_{1,0}$ is stronger in case of CO poisoning than in case of dehydration. Compare for example the change from 0 ppm to 20 ppm CO (black and blue curves in Figures 7.6a and 7.6d) with the change from 55 % relative humidity to 35 % (black and red curve in Figures 7.2a and 7.2d). In both cases, the first harmonic changes in magnitude from 0.6×10^{-5} Ωm^{-2} to 2×10^{-5} Ωm^{-2}, i.e. the performance loss is about equal. But the second harmonic changes about two orders of magnitude in the case of CO poisoning but less then one order of magnitude in the case of dehydration.

In addition to this quantitatively different behaviour of the magnitude of $H_{2,0}$, the phase angle shows a clear qualitative change: while under normal or dehydrated conditions the phase angle starts at small negative values and decreases further, in case of CO poisoning the phase angle undergoes a change from positive values at about 90° at low frequencies until it reaches the same negative values as in the case without CO poisoning. Therefore, in the Nyquist plot, the spiral has an additional 90° turn. It starts in the first quadrant and runs clockwise through first, fourth, third and second quadrant. Therefore, in comparison to dehydration, the spiral does not only increase its diameter but also significantly increases the phase angle through which it runs.

7.4 Conclusions

In this chapter, the influence of dehydration phenomena on the NFRA spectra of a PEM fuel cell was investigated in a tailored experimental setup. A differential fuel cell design was used in order to avoid spatial distributions along the channel. H_2/H_2

operation eliminated the masking effect of the cathode and avoided water production within the cell.

With this setup, NFRA spectra were measured at different fuel gas humidification levels. The measured linear $H_{1,0}$ spectra are equal to classic EIS spectra. Under dehydration, those $H_{1,0}$ spectra showed not only an increase in the membrane resistance as expected but also a strong increase in the reaction resistance. A hypothesis was that dehydration leads to a strong decrease of the proton conductivity of the Nafion phase within the catalyst layer. As a result, the protonic connection of the catalyst sites to the membrane is decreased. Especially active sites with a long protonic path to the membrane are affected and become inactive. This leads to a loss in active area of the catalyst and with this to an increase of the charge transfer reaction resistance.

This explanation was supported by the results of the modelling work, in which the proton transport within the catalyst layer was incorporated into the 0D model of the differential H_2/H_2 cell in Chapter 6.3. It was seen that the decreasing protonic conductivity within the catalyst layer leads to an increase of the reaction resistance in the linear spectra. Additionally, the qualitative behaviour of the second order FRF $H_{2,0}$, i.e. an increase in magnitude over the whole frequency range, was described by the model as well. Nevertheless, the estimated decrease of the effective protonic conductivity caused by the decreased gas humidification was not sufficient to quantitatively explain the increase of the reaction resistance. A further decrease of the effective protonic conductivity of the polymer phase was necessary to fit the experimental data. This additional loss in protonic conductivity might be caused by the electro-osmotic water transport in the catalyst layer, which further decreases the water content of the polymer phase and thus the protonic conductivity.

Finally, the key features of the NFRA spectra under dehydration were compared to those of CO poisoning from Chapter 6.2. It could be seen that on the one hand the linear $H_{1,0}$ spectra, i.e. the electrochemical impedance, shows similar features. Therefore, EIS spectra are difficult to use for an unambiguous diagnosis of dehydration and CO poisoning. On the other hand, the second order frequency response function $H_{2,0}$ shows qualitative as well as quantitative differences between both cases. Especially the phase angle of $H_{2,0}$ in the low and mid-frequency range changes strongly under CO, whereas it is constant under dehydration. Additionally, the magnitude of $H_{2,0}$ in relation to the magnitude of $H_{1,0}$ changes much stronger in case of CO poisoning than under dehydration.

These nonlinear features of the second order FRF can be used for a discrimination between CO poisoning and dehydration in the course of an unambiguous diagnosis of

PEMFCs.

Chapter 8

Summary and Conclusions

In this work, the suitability of nonlinear frequency response analysis for the diagnosis of PEM fuel cells has been investigated. NFRA is a promising approach because it is applicable in-situ and during operation and can be easily implemented. In the current work, NFRA has been applied for the analysis of fuel cells for the first time. With NFRA, it is possible to diagnose critical states of fuel cells which might lead to performance loss, increased degradation or even damage of the cell. Especially, reversible critical states are of interest because they can be counteracted by a change of the operating conditions. Therefore, this work focused on the most important reversible critical states resulting from defective water management, i.e. dehydration and flooding, and from fuel gas impurities, especially CO poisoning.

For a diagnosis of such critical states, NFRA uses a sinusoidal perturbation to analyse the electrical input-output behaviour of the system under investigation. In contrast to classic methods like EIS, which use a small perturbation amplitude to analyse the system in a quasi-linear range, NFRA uses elevated amplitudes to analyse the linear as well as the nonlinear input-output behaviour of the system. The additional nonlinear information obtained with NFRA is useful for model discrimination, parameter estimation and diagnosis.

In the first preliminary experiments of the current work, NFRA spectra were measured in a PEMFC under dehydration, flooding and CO poisoning conditions. A simplified mathematical NFRA approach with a carefully chosen perturbation amplitude was used. With this approach, it was possible to determine first and second order frequency response functions ($H_{1,0}$ and $H_{2,0}$) simultaneously in one measurement with the same experimental effort as classic EIS. With those measurements, it was validated that the first order FRFs $H_{1,0}$ are identical with the EIS spectra, as expected from the-

ory. Under flooding conditions, these first order spectra showed clear features (i.e. an increase in mass transport resistance) which can be used to identify flooding. However, for dehydration and CO poisoning it was found that under certain operating conditions these linear spectra show similar qualitative changes. Therefore, the linear spectra are not sufficient for an unambiguous diagnosis. Nevertheless, the second order FRF $H_{2,0}$ showed different qualitative changes under dehydration and CO poisoning conditions. This gave the hint that $H_{2,0}$ might be used for the discrimination of these two states. Thus, an unambiguous diagnosis would be possible.

These observations motivated a further and more detailed analysis of the cases of CO poisoning and dehydration. The aim was on the one hand to clarify why the linear spectra showed similar behaviour in both cases and on the other hand to analyse the possible use of the second order spectra for a discrimination in more detail. To do so, a combined experimental and modelling approach was developed. For this, a special experimental setup was designed: the differential H_2/H_2 cell. In this approach, H_2/H_2 operation was used to avoid the masking effects of the slow cathodic reaction by exchanging it with the hydrogen evolution reaction. Furthermore, the differential cell design avoided along-the-channel effects and concentration gradients. This experimental setup made a simplified modelling approach possible, which allowed the numerical calculation of the NFRA spectra.

The differential H_2/H_2 cell was used to measure NFRA spectra under CO poisoning conditions. For these measurements, a working point was chosen that simulates a scenario of beginning CO poisoning, which is most relevant for diagnosis. The influence of the CO content in the fuel gas on the first and second order NFRA spectra ($H_{1,0}$ and $H_{2,0}$) was investigated. Finally, key features of CO poisoning in the NFRA spectra have been identified.

In addition to the experimental investigations of CO poisoning, a simplified model from literature could be used to simulate NFRA spectra under CO poisoning numerically. These simulated NFRA spectra were in reasonably good agreement with the experimental spectra. It was seen that the experimentally observed key features of the NFRA spectra under CO poisoning are based on the main mechanism of CO poisoning, i.e. preferential adsorption of CO to the active catalyst sites, which leads to site exclusion and decrease in catalytic activity for the hydrogen oxidation reaction. However, small discrepancies between experimental and numerical spectra were discussed and could be attributed to model simplifications and parameter inaccuracies. Unfortunately, within the scope of this work these problems could not be fixed on the basis of the experimental NFRA data alone. However, suggestions for refinement and

extensions of the model were discussed.

Finally, dehydration phenomena were analysed with the NFRA approach in the differential H_2/H_2 cell. At first, NFRA spectra were measured at different levels of fuel gas humidification. Under dehydration conditions, an increase in the membrane resistance was expected and observed. However, this increase was negligibly small compared to the observed increase of the reaction resistance, which caused the main losses under dehydration conditions. A hypothesis for this behaviour was that dehydration decreases the proton conductivity of the polymer electrolyte phase within the catalyst layer. This leads to a decrease of the protonic connection of the catalyst sites to the membrane. Especially active sites with a long protonic path to the membrane are affected and become inactive. This results in a loss of active area and thus to an increase of the reaction resistance.

To confirm this hypothesis, a modelling approach was used. Therefore, a model of the differential H_2/H_2 cell which included the proton transport in the catalyst layer was developed. With this model, NFRA spectra were simulated numerically for different levels of fuel gas humidification. It was seen that the decreasing protonic conductivity in the catalyst layer leads to an increase in reaction resistance in the linear spectra, as observed previously in the measurements. Additionally, the simulated second order spectra of $H_{2,0}$ showed the same qualitative changes as in the measurements. However, although the model could explain the key features of the NFRA spectra during dehydration qualitatively, it was not sufficient to represent quantitatively the increase of the reaction resistance. This was because the estimation of the decrease of the effective proton conductivity on the basis of the decreased gas humidification alone was not sufficient. A further decrease of the effective proton conductivity was necessary to fit the experimental data. This additional loss in proton conductivity might be caused by the electroosmotic water transport in the catalyst layer, which decreases the water content in the polymer electrolyte further than estimated from the humidification level alone.

Finally, the key features of the NFRA spectra under dehydration and CO poisoning in the differential H_2/H_2 cell were compared. It was seen that in both cases the linear $H_{1,0}$ spectra show similar features (i.e. an increased reaction resistance caused by a decreased active area). Therefore, the $H_{1,0}$ spectra are difficult to use for an unambiguous diagnosis. However, the second order frequency response function $H_{2,0}$ shows quantitative as well as qualitative differences which might principally be used for a discrimination between CO poisoning and dehydration in the course of an unambiguous diagnosis in PEMFCs.

Nevertheless, in conclusion it has to be mentioned that the practical measurement and determination of the HFRF and the correct interpretation of the NFRA spectra is a complex and difficult task. Even in the very simplified system of the differential H_2/H_2 cell, a careful experimental procedure for measuring the NFRA spectra is necessary, especially with regard to the determination of the correct amplitude, noise and reproducibility of the measurement.

In the modelling work, it was seen that especially the higher order FRF are more prone to parameter inaccuracies. Additionally, with more complex models the effort for the analytical and numerical determination of the NFRA spectra increases strongly. Finally, the higher order frequency response functions show much more complex behaviour and cannot be directly related to physical effects, which makes their interpretation difficult and less comprehensible.

In addition to the main topic of NFRA for diagnosis of PEMFCs, a second important side aspect was investigated in the current work. During the first experiments with the differential H_2/H_2 cell under CO poisoning, autonomous potential oscillations were observed for the first time at a Pt anode in a PEM fuel cell. In a first measurement series, the influence of CO concentration on the behaviour of the oscillations was analysed. Higher CO concentrations were found to increase the oscillation frequency because of enhanced CO adsorption. In a second measurement series, the influence of the cell temperature was investigated. By means of activation energy analysis, a different influence of the temperature on the oscillation frequency has been found for Pt catalyst (E_a = 40.5$\pm$0.6 kJ mol^{-1}) compared to the previously reported case at PtRu (E_a = 60.9 kJ mol^{-1}) [244]. Furthermore, oscillations were found in H_2/O_2 operation, too. They occur if the anode overpotential is forced to increase until the onset potential for CO oxidation is reached. Nevertheless, in technical fuel cells operated with passive loads, the anode overpotential does usually not reach such high values, because a large fraction of the cell overpotential is caused by cathodic and ohmic losses. However, using the differential H_2/H_2 cell approach these oscillations could be revealed.

Bibliography

[1] Intergovernmental Panel on Climate Change. *Fourth Assessment Report: Climate Change 2007*.

[2] International Energy Agency. *World Energy Outlook 2010*. 2010.

[3] VDI-Technologiezentrum / Bundesministerium für Verkehr, Bau und Stadtentwicklung. *Studie zur Entwicklung eines Markteinführungsprogramms für Brennstoffzellen in speziellen Märkten*. 2010.

[4] K. Kordesch and G. Simander. *Fuel Cells and Their Applications*. Wiley-VCH, 1996.

[5] J. Larmine and A. Dicks. *Fuel Cell Systems Explained*. Wiley, 2nd edition, 2003.

[6] R. O'Hayre, S.-W. Cha, W. Colella, and F. B. Prinz. *Fuel Cell Fundamentals*. Wiley, 2nd edition, 2009.

[7] F. Barbir. *PEM Fuel Cells: Theory and Practice*. Elsevier Academic Press, 2nd edition, 2011.

[8] W. Vielstich, A. Lamm, and H. A. Gasteiger. *Handbook of Fuel Cells – Fundamentals, Technology and Applications. (Parts 1–6)*. Wiley, 2003 – 2009.

[9] T. Kadyk, R. Hanke-Rauschenbach, and K. Sundmacher. Nonlinear frequency response analysis for the diagnosis of carbon monoxide poisoning in PEM fuel cell anodes. *J. Appl. Electrochem.*, in press, 2011.

[10] T. Kadyk, S. Kirsch, R. Hanke-Rauschenbach, and K. Sundmacher. Autonomous potential oscillations at the Pt anode of a PEM fuel cell under CO poisoning. *Electrochim. Acta*, in press, 2011.

[11] T. Kadyk, R. Hanke-Rauschenbach, and K. Sundmacher. Nonlinear frequency response analysis of polymer electrolyte membrane fuel cells under dehydration. *Submitted to J. Electroanal. Chem.*, 2011.

[12] N. Wagner, W. Schnurnberger, B. Müller, and M. Lang. Electrochemical impedance spectra of solid-oxide fuel cells and polymer membrane fuel cells. *Electrochim. Acta*, 43(24):3785–3793, 1998.

[13] M. Ciureanu and H. Wang. Electrochemical impedance study of electrode-membrane assemblies in PEM fuel cells I. Electro-oxidation of H_2 and H_2/CO mixtures on Pt-based gas-diffusion electrodes. *J. Electrochem. Soc.*, 146(11):4031–4040, 1999.

[14] O. Himanen, T. Hottinen, M. Mikkola, and V. Saarinen. Characterization of membrane electrode assembly with hydrogen-hydrogen cell and AC-impedance spectroscopy. Part I: Experimental. *Electrochim. Acta*, 52(1):206–214, 2006.

[15] I. A. Schneider, S. von Dahlen, A. Wokaun, and G. G. Scherer. A segmented microstructured flow field approach for submillimeter resolved local current measurement in channel and land areas of a PEFC. *J. Electrochem. Soc.*, 157(3):B338–B341, 2010.

[16] M. Ciureanu. Effects of Nafion® dehydration in PEM fuel cells. *J. Appl. Electrochem.*, 34(7):705–714, 2004.

[17] K. C. Neyerlin, H. A. Gasteiger, C. K. Mittelstaedt, J. Jorne, and W. Gu. Effect of relative humidity on oxygen reduction kinetics in a PEMFC. *J. Electrochem. Soc.*, 152(6):A1073–A1080, 2005.

[18] H. Gasteiger and T. Schmidt. Short course: Polymer electrolyte fuel cells. supplementary material to short course at 218th ECS Meeting, Las Vegas/USA, October 2010.

[19] C. K. Mittelstaedt and H. Liu. Conductivity, permeability and ohmic shortening of ionomeric membranes. In W. Vielstich, H. Yokokawa, and H. A. Gasteiger, editors, *Handbook of Fuel Cells*, volume 5, chapter 23, pages 345–359. Wiley, 2009.

[20] R. Borup, J. Meyers, B. Pivovar, Y. S. Kim, R. Mukundan, N. Garland, D. Myers, M. Wilson, F. Garzon, D. Wood, P. Zelenay, K. More, K. Stroh, T. Zawodzinski, J. Boncella, J. E. McGrath, M. Inaba, K. Miyatake, M. Hori, K. Ota, Z. Ogumi, S. Miyata, A. Nishikata, Z. Siroma, Y. Uchimoto, K. Yasuda, K. I. Kimijima, and N. Iwashita. Scientific aspects of polymer electrolyte fuel cell durability and degradation. *Chem. Rev.*, 107(10):3904–3951, 2007.

[21] T. Madden, M. Perry, L. Protsailo, M. Gummalla, S. Burlatsky, N. Cipollini, S. Motupally, and T. Jarvi. Proton exchange membrane fuel cell degradation: mechanisms and recent progress. In W. Vielstich, H. Yokokawa, and H. A. Gasteiger, editors, *Handbook of Fuel Cells*, volume 6, chapter 58, pages 861–880. Wiley, 2009.

[22] K. Heitner-Wirguin. Recent advances in perflourinated ionomer membranes: structure, properties and applications. *J. Membr. Sci.*, 120:1–33, 1996.

[23] M. Doyle and G. Rajendran. Perflourinated membranes. In W. Vielstich, H. A. Gasteiger, and A. Lamm, editors, *Handbook of Fuel Cells – Fundamentals, Technology and Applications*, volume 3, chapter 30, pages 364–395. John Wiley and Sons, Ltd., 2003.

[24] T. D. Gierke and W. Y. Hsu. Perflourinated ionomer membranes. Number 180, chapter 13, page 283. ACS Symposium Series, 1982.

[25] G. Pourcelly and C. Gavach. *Proton Conductors, Solids, Membranes and Gels – Materials and Devices*. Cabridge University Press, 1992.

[26] R. E. Fernandez. Perflourinated membranes. In *Polymer Data Handbook*, pages 233–236. Oxford University Press, 1999.

[27] K. A. Mauritz and R. B. Moore. State of understanding Nafion. *Chem. Rev.*, 104(10):4535–4585, 2004.

[28] E. Endoh, S. Terazono, H. Widjaja, and Y. Takimoto. Degradation study of MEA for PEMFCs under low humidity conditions. *Electrochem. Solid State Lett.*, 7(7):A209–A211, 2004.

[29] V. O. Mittal, H. R. Kunz, and J. M. Fenton. Membrane degradation mechanisms in PEMFCs. *ECS Transact.*, 3(1):507–517, 2006.

[30] V. O. Mittal, H. R. Kunz, and J. M. Fenton. Membrane degradation mechanisms in PEMFCs. *J. Electrochem. Soc.*, 154(7):B652–B656, 2007.

[31] A. B. LaConti, A. R. Fragala, and J. R. Boyack. Solid polymer electrolyte electrochemical cells: Electrode and other material consideration. In J. D. E. McIntyre, S Srinivasan, and F. G. Wills, editors, *Proceedings of the Symposium on Electrode Materials and Process for Energy Conversion and Storage*, volume 77, page 354, Princeton, NJ, 1977. The Electrochemical Society, Inc.

[32] M. LaConti, R. Hamadan, and R. C. McDonald. Mechanisms of membrane degradation. In W. Vielstich, H. Yokokawa, and H. A. Gasteiger, editors, *Handbook of Fuel Cells – Fundamentals, Technology and Application*, volume 3, chapter 49. John Wiley and Sons, Ltd., 2006.

[33] M. Inaba, H. Yamada, J. Tokunaga, K. Matsuzawa, A. Hatanaka, and A. Tasaka. Hydrogen peroxide formation as a degradation factor of polymer electrolyte fuel cells. *ECS Trans.*, 1:315, 2005.

[34] W. Liu and D. Zuckerbrod. In situ detection of hydrogen peroxide in PEM fuel cells. *J. Electrochem. Soc.*, 152(6):A1165–A1170, 2005.

[35] T. Kinumoto, M. Inaba, Y. Nakayama, K. Ogata, R. Umebayashi, A. Tasaka, Y. Iriyama, T. Abe, and Z. Ogumi. Durability of perfluorinated ionomer membrane against hydrogen peroxide. *J. Power Sources*, 158(2):1222–1228, 2006.

[36] A. Ohma, S. Suga, S. Yamamoto, and K. Shinohara. Phenomenon analysis of PEFC for automotive use. (1) Membrane degradation behavior during OCV hold test. *ECS Tans.*, 3(1):519 – 529, 2006.

[37] D. E. Curtin, R. D. Lousenberg, T. J. Henry, P. C. Tangeman, and M. E. Tisack. Advanced materials for improved PEMFC performance and life. *J. Power Sources*, 131(1-2):41–48, 2004.

[38] S. Hommura, K. Kawahara, T. Shimohira, and Y. Teraoka. Development of a method for clarifying the perfluorosulfonated membrane degradation mechanism in a fuel cell environment. *J. Electrochem. Soc.*, 155(1):A29–A33, 2008.

[39] A. Bosnjakovic and S. Schlick. Naflon perfluorinated membranes treated in Fenton media: radical species detected by ESR spectroscopy. *J. Phys. Chem. B*, 108(14):4332–4337, 2004.

[40] T. Xie and C. A. Hayden. A kinetic model for the chemical degradation of perfluorinated sulfonic acid ionomers: Weak end groups versus side chain cleavage. *Polymer*, 48(19):5497–5506, 2007.

[41] T. A. Zawodzinksi, C. Derouin, S. Radzinski, R. J. Sherman, V. T. Smith, T. E. Springer, and S. Gottesfeld. Water uptake by and transport through Nafion 117 membranes. *J. Electrochem. Soc.*, 140(4):1041 – 1047, April 1993.

[42] T. A. Zawodzinski, T. E. Springer, J. Davey, R. Jestel, C. Lopez, J. Valerio, and S. Gottesfeld. A comparative-study of water-uptake by and transport through ionomeric fuel-cell membranes. *J. Electrochem. Soc.*, 140(7):1981–1985, 1993.

[43] J. T. Hinatsu, M. Mizuhata, and H. Takenaka. Water-uptake of perfluorosulfonic acid membranes from liquid water and water-vapor. *J. Electrochem. Soc.*, 141(6):1493–1498, 1994.

[44] K. Broka and P. Ekdunge. Oxygen and hydrogen permeation properties and water uptake of Nafion 117 membrane and recast film for PEM fuel cell. *J. Appl. Electrochem.*, 27(2):117–123, 1997.

[45] C. A. Reiser, L. Bregoli, T. W. Patterson, J. S. Yi, J. D. L. Yang, M. L. Perry, and T. D. Jarvi. A reverse-current decay mechanism for fuel cells. *Electrochem. Solid State Lett.*, 8(6):A273–A276, 2005.

[46] J. H. Ohs, U. Sauter, S. Maass, and D. Stolten. Modeling hydrogen starvation conditions in proton-exchange membrane fuel cells. *J. Power Sources*, 196(1):255–263, 2011.

[47] L. M. Roen, C. H. Paik, and T. D. Jarvic. Electrocatalytic corrosion of carbon support in PEMFC cathodes. *Electrochem. Solid State Lett.*, 7(1):A19–A22, 2004.

[48] K. H. Kangasniemi, D. A. Condit, and T. D. Jarvi. Characterization of vulcan electrochemically oxidized under simulated PEM fuel cell conditions. *J. Electrochem. Soc.*, 151(4):E125–E132, 2004.

[49] B. Merzougui and S. Swathirajan. Rotating disk electrode investigations of fuel cell catalyst degradation due to potential cycling in acid electrolyte. *J. Electrochem. Soc.*, 153(12):A2220–A2226, 2006.

[50] M. Pourbaix. *Atlas of Electrochemical Equilibria in Aqueous Solution*. Pergamon Press, Oxford, 1966.

[51] K. Kinoshita, J. Lundquist, and P. Stonehart. Potential cycling effects on platinum electrocatalyst surfaces. *J. Electroanal. Chem. Interfacial. Electrochem.*, 48(2):157–166, 1973.

[52] T. W. Patterson and R. M. Darling. Damage to the cathode catalyst of a PEM fuel cell caused by localized fuel starvation. *Electrochem. Solid State Lett.*, 9(4):A183–A185, 2006.

[53] S. Mitsushima, S. Kawahara, K. I. Ota, and N. Kamiya. Consumption rate of Pt under potential cycling. *J. Electrochem. Soc.*, 154(2):B153–B158, 2007.

[54] G. Jerkiewicz, G. Vatankhah, J. Lessard, M. P. Soriaga, and Y. S. Park. Surface-oxide growth at platinum electrodes in aqueous H_2SO_4: Reexamination of its mechanism through combined cyclic-voltammetry, electrochemical quartz-crystal nanobalance, and Auger electron spectroscopy measurements. *Electrochim. Acta*, 49(9-10):1451–1459, 2004.

[55] M. Inaba and H. Yamada. Factors influencing ionomer degradation. In W. Vielstich, H. Yokokawa, and H. A. Gasteiger, editors, *Handbook of Fuel Cells – Fundamentals, Technology and Applications*, volume 5, chapter 25, pages 375 –385. John Wiley and Sons, Ltd., 2009.

[56] W. Y. Hsu and T. D. Gierke. Ion-transport and clustering in nafion perfluorinated membranes. *J. Membr. Sci.*, 13(3):307–326, 1983.

[57] T. D. Gierke, G. E. Munn, and F. C. Wilson. The morphology in Nafion perfluorinated membrane products, as determined by wide-angle and small-angle X-ray studies. *J. Polym. Sci. Pt. B-Polym. Phys.*, 19(11):1687–1704, 1981.

[58] H. L. Yeager and A. Steck. Cation and water diffusion in Nafion ion-exchange membranes: Influence of polymer structure. *J. Electrochem. Soc.*, 128(9):1880–1884, 1981.

[59] H. G. Haubold, T. Vad, H. Jungbluth, and P. Hiller. Nano structure of Nafion: a SAXS study. *Electrochim. Acta*, 46(10-11):1559–1563, 2001.

[60] S. J. Paddison, L. R. Pratt, and T. A. Zawodzinski. Conformations of perfluoroether sulfonic acid side chains for the modeling of Nafion. *J. New Mat.Electrochem. Syst.*, 2(3):183–188, 1999.

[61] M. Eikerling, A. A. Kornyshev, and U. Stimming. Electrophysical properties of polymer electrolyte membranes: A random network model. *J. Phys. Chem. B*, 101:10807–10820, 1997.

[62] K. Jiao and X. Li. Water transport in polymer electrolyte membrane fuel cells. *Progress in Energy and Combustion Science*, 37:221–291, 2011.

[63] T. A. Zawodzinski, Neeman M., L. O. Sillerud, and S. Gottesfeld. Determination of water diffusion coefficients in perflourosulfonate ionomeric membranes. *J. Phys. Chem.*, 95:6040–6044, 1991.

[64] C. Yang, S. Srinivasan, A. B. Bocarsly, S. Tulyani, and J. B. Benziger. A comparison of physical properties and fuel cell performance of Nafion and zirconium phosphate/Nafion composite membranes. *J. Membr. Sci.*, 237(1-2):145–161, 2004.

[65] T. E. Springer, T. A. Zawodzinski, M. S. Wilson, and S. Gottesfeld. Characterization of polymer electrolyte fuel cells using AC impedance spectroscopy. *J. Electrochem. Soc.*, 143(2):587–599, 1996.

[66] F. A. Uribe, T. E. Springer, and S. Gottesfeld. A microelectrode study of oxygen reduction at the platinum/recast-Nafion film interface. *J. Electrochem. Soc.*, 139(3):765–773, 1992.

[67] H. Xu, Y. Song, H. Kunz, and J. M. Fenton. Effect of elevated temperature and reduced relative humidity on ORR kinetics for PEM fuel cells. *J. Electrochem. Soc.*, 152(9):A1828–A1836, 2005.

[68] H. Li, Y. H. Tang, Z. W. Wang, Z. Shi, S. H. Wu, D. T. Song, J. L. Zhang, K. Fatih, J. J. Zhang, H. J. Wang, Z. S. Liu, R. Abouatallah, and A. Mazza. A review of water flooding issues in the proton exchange membrane fuel cell. *J. Power Sources*, 178(1):103–117, 2008.

[69] M. B. Ji and Z. D. Wei. A review of water management in polymer electrolyte membrane fuel cells. *Energies*, 2(4):1057–1106, 2009.

[70] N. Yousfi-Steiner, P. Mocoteguy, D. Candusso, D. Hissel, A. Hernandez, and A. Aslanides. A review on PEM voltage degradation associated with water management: Impacts, influent factors and characterization. *J. Power Sources*, 183(1):260–274, 2008.

[71] W. Dai, H. J. Wang, X. Z. Yuan, J. J. Martin, D. J. Yang, J. L. Qiao, and J. X. Ma. A review on water balance in the membrane electrode assembly of proton exchange membrane fuel cells. *Int. J. Hydrog. Energy*, 34(23):9461–9478, 2009.

[72] S. Kim and M. M. Mench. Investigation of temperature-driven water transport in polymer electrolyte fuel cell: Thermo-osmosis in membranes. *J. Membr. Sci.*, 328(1–2):113–120, 2009.

[73] R. Zaffou, J. S. Yi, H. R. Kunz, and J. M. Fenton. Temperature-driven water transport through membrane electrode assembly of proton exchange membrane fuel cells. *Electrochem. Solid State Lett.*, 9(9):A418–A420, 2006.

[74] R. Hanke-Rauschenbach, M. Mangold, and K. Sundmacher. Nonlinear dynamics of fuel cells: A review. *Rev. Chem. Eng.*, 27(1–2):23–52, 2011.

[75] X. Cheng, Z. Shi, N. Glass, L. Zhang, J. Zhang, D. Song, Z. Liu, H. Wang, and J. Shen. A review of PEM hydrogen fuel cell contamination: Impacts, mechanisms and mitigation. *J. Power Sources*, 165:739–756, 2007.

[76] H. F. Oetjen, V. M. Schmidt, U. Stimming, and F. Trila. Performance data of a proton exchange membrane fuel cell using H_2/CO as fuel gas. *J. Electrochem. Soc.*, 143(12):3838–3842, 1996.

[77] R. A. Lemons. Fuel-cells for transportation. *J. Power Sources*, 29:251–264, 1990.

[78] J. J. Baschuk and X. G. Li. Carbon monoxide poisoning of proton exchange membrane fuel cells. *Int. J. Energy Res.*, 25(8):695–713, 2001.

[79] W. Vogel, J. Lundquist, P. Ross, and P. Stonehart. Reaction pathways and poisonss – II: The rate controlling step for electrochemical oxidation of hydropen on Pt in acid and poisoning of the reaction by CO. *Electrochim. Acta*, 20:79–90, 1975.

[80] P. Stonehart and P. N. Ross. Commonality of surface processes in electrocatalysis and gas-phase heterogeneous catalysis. *Catal. Rev.-Sci. Eng.*, 12(1):1–35, 1975.

[81] P. Stonehart and G. Kohlmayr. Effect of poisons on kinetic parameters for platinum electrocatalyst sites. *Electrochim. Acta*, 17:369–382, 1972.

[82] H. P. Dhar, L. G. Christner, and A. K. Kush. Nature of CO adsorption during H_2 oxidation in relation to modelling for CO poisoning of a fuel-cell anode. *J. Electrochem. Soc.*, 134(12):3021–3026, 1987.

[83] T. E. Springer, T. Rockward, T. A. Zawodzinski, and S. Gottesfeld. Model for polymer electrolyte fuel cell operation on reformate feed - Effects of CO, H_2 dilution, and high fuel utilization. *J. Electrochem. Soc.*, 148(1):A11–A23, 2001.

[84] S. Gottesfeld and J. Pafford. A new approach to the problem of carbon-monoxide poisoning in fuel-cells operating at low temperatures. *J. Electrochem. Soc.*, 135(10):2651–2652, 1988.

[85] V. M. Schmidt, H.-F. Oetjen, and J. Divisek. Performance improvement of a PEMFC using fuels with CO by addition of oxygen-evolving compounds. *J. Electrochem. Soc.*, 144(9):L237–L238, 1997.

[86] J. Divisek, H. F. Oetjen, V. Peinecke, V. M. Schmidt, and U. Stimming. Components for PEM fuel cell systems using hydrogen and CO containing fuels. *Electrochim. Acta*, 43(24):3811–3815, 1998.

[87] J. H. Wee and K. Y. Lee. Overview of the development of CO-tolerant anode electrocatalysts for proton-exchange membrane fuel cells. *J. Power Sources*, 157:128–135, 2006.

[88] H. A. Gasteiger, N. Marković, P. N. Ross Jr., and E. J. Cairns. CO electrooxidation on well-characterized Pt-Ru alloys. *J. Phys. Chem.*, 98:617 – 625, 1994.

[89] H. A. Gasteiger, N. M. Marković, and P. N. Ross Jr. H_2 and CO electrooxidation on well-characterized Pt, Ru and Pt-Ru. 1. Rotating disk electrode studies of the pure gases including temperature effects. *J. Phys. Chem.*, 99:8290–8301, 1995.

[90] H. A. Gasteiger, N. M. Marković, and P. N. Ross Jr. H_2 and CO electrooxidation on well-characterized Pt, Ru and Pt-Ru. 2. Rotating disk electrode studies of CO/H_2 mixtures at 62°C. *J. Phys. Chem.*, 99:16757–16767, 1995.

[91] T. J. Schmidt, H. A. Gasteiger, and R. J. Behm. Rotating disk electrode measurements on the CO tolerance of a high-surface area Pt/Vulcan carbon fuel cell catalyst. *J. Electrochem. Soc.*, 146(4):1296–1304, 1999.

[92] F. B. de Mongeot, M. Scherer, B. Gleich, E. Kopatzki, and R. J. Behm. CO adsorption and oxidation on bimetallic Pt/Ru(0001) surfacesa combined STM and TPD/TPR study. *Surf. Sci.*, 411(3):249–262, 1998.

[93] L. Giorgi, A. Pozio, C. Bracchini, R. Giorgi, and S. Turtu. H_2 and H_2/CO oxidation mechanism on Pt/C, Ru/C and Pt-Ru/C electrocatalysts. *J. Appl. Electrochem.*, 31(3):325–334, 2001.

[94] E. Christoffersen, P. Liu, A. Ruban, H. L. Skriver, and J. K. Norskov. Anode materials for low-temperature fuel cells: A density functional theory study. *J. Catal.*, 199(1):123 – 131, 2001.

[95] R. Hanke-Rauschenbach, C. Weinzierl, M. Krasnyk, L. Rihko-Struckmann, H. Lu, and K. Sundmacher. Operating behavior and scale-up of an ECPrOx unit for CO removal from reformate for PEM fuel cell application. *J. Electrochem. Soc.*, 156(10):B1267–B1275, 2009.

[96] J. X. Zhang and R. Datta. Electrochemical preferential oxidation of CO in reformate. *J. Electrochem. Soc.*, 152(6):A1180–A1187, 2005.

[97] J. X. Zhang, J. D. Fehribach, and R. Datta. Mechanistic and bifurcation analysis of anode potential oscillations in PEMFCs with CO in anode feed. *J. Electrochem. Soc.*, 151(5):A689–A697, 2004.

[98] H. Lu, L. Rihko-Struckmann, R. Hanke-Rauschenbach, and K. Sundmacher. Dynamic behavior of a PEM fuel cell during electrochemical CO oxidation on a PtRu anode. *Top. Catal.*, 51(1-4):89–97, 2008.

[99] H. Lu, L. Rihko-Struckmann, R. Hanke-Rauschenbach, and K. Sundmacher. Improved electrochemical CO removal via potential oscillations in serially connected PEM fuel cells with PtRu anodes. *Electrochim. Acta*, 54(4):1184–1191, 2009.

[100] P. P. Lopes, E. A. Ticianelli, and H. Varela. Potential oscillations in a proton exchange membrane fuel cell with a Pd-Pt/C anode. *J. Power Sources*, 196:84 – 89, 2011.

[101] J. F. Wu, X. Z. Yuan, H. J. Wang, M. Blanco, J. J. Martin, and J. J. Zhang. Diagnostic tools in PEM fuel cell research: Part I Electrochemical techniques. *Int. J. Hydrog. Energy*, 33(6):1735–1746, 2008.

[102] J. F. Wu, X. Z. Yuan, H. J. Wang, M. Blanco, J. J. Martin, and J. J. Zhang. Diagnostic tools in PEM fuel cell research: Part II Physical/chemical methods. *Int. J. Hydrog. Energy*, 33(6):1747–1757, 2008.

[103] D. J. L. Brett, A. R. Kucernak, P. Aguiar, S. C. Atkins, N. P. Brandon, R. Clague, L. F. Cohen, G. Hinds, C. Kalyvas, G. J. Offer, B. Ladewig, R. Maher, A. Marquis, P. Shearing, and V. Vasileiadis, N. Vesovic. What happens inside a fuel cell? Developing an experimental functional map of fuel cell performance. *ChemPhysChem*, 11:2714–2731, 2010.

[104] A. Bazylak. Liquid water visualization on PEM fuel cells: A review. *Int. J. Hydrog. Energy*, 34:3845–3857, 2009.

[105] J. St Pierre. PEMFC in situ liquid-water-content monitoring status. *J. Electrochem. Soc.*, 154(7):B724–B731, 2007.

[106] D. Spernjak, A. K. Prasad, and S. G. Advani. Experimental investigation of liquid water formation and transport in a transparent single-serpentine PEM fuel cell. *J. Power Sources*, 170(2):334–344, 2007.

[107] K. Tüber, D. Pócza, and C. Hebling. Visualization of water buildup in the cathode of a transparent PEM fuel cell. *J. Power Sources*, 124(2):403–414, 2003.

[108] A. Hakenjos, H. Muenter, U. Wittstadt, and C. Hebling. A PEM fuel cell for combined measurement of current and temperature distribution, and flow field flooding. *J. Power Sources*, 131(1-2):213–216, 2004.

[109] J. B. Zhang, D. Kramer, R. Shimoi, Y. Ona, E. Lehmann, A. Wokaun, K. Shinohara, and G. G. Scherer. In situ diagnostic of two-phase flow phenomena in polymer electrolyte fuel cells by neutron imaging. Part B. Material variations. *Electrochim. Acta*, 51(13):2715–2727, 2006.

[110] D. A. McKay, W. T. Ott, and Stefanopoulou A. G. Modeling, parameter identification and validation of reactant water dynamics for a fuel cell stack. In *Proceedings of IMECE 2005 ASME International Mechanical Engineering Congress and Exposition*, Orlando, Florida, USA, November 5–11 2005.

[111] F. Y. Zhang, X. G. Yang, and C. Y. Wang. Liquid water removal from a polymer electrolyte fuel cell. *J. Electrochem. Soc.*, 153(2):A225–A232, 2006.

[112] A. Bazylak, D. Sinton, Z. S. Liu, and N. Djilali. Effect of compression on liquid water transport and microstructure of PEMFC gas diffusion layers. *J. Power Sources*, 163(2):784–792, 2007.

[113] X. Liu, H. Guo, and C. F. Ma. Water flooding and two-phase flow in cathode channels of proton exchange membrane fuel cells. *J. Power Sources*, 156(2):267–280, 2006.

[114] X. Liu, H. Guo, F. Ye, and C. F. Ma. Water flooding and pressure drop characteristics in flow channels of proton exchange membrane fuel cells. *Electrochim. Acta*, 52(11):3607–3614, 2007.

[115] S. Ge and C. Y. Wang. Liquid water formation and transport in the PEFC anode. *J. Electrochem. Soc.*, 154(10):B998–B1005, 2007.

[116] A. M. Lopez, F. Barreras, A. Lozano, J. A. Garcia, L. Valino, and R. Mustata. Comparison of water management between two bipolar plate flow-field geometries in proton exchange membrane fuel cells at low-density current range. *J. Power Sources*, 192(1):94–99, 2009.

[117] H. S. Kim and K. Min. Experimental investigation of dynamic responses of a transparent PEM fuel cell to step changes in cell current density with operating temperature. *J. Mech. Sci. Technol.*, 22(11):2274–2285, 2008.

[118] M. Yamauchi, K. Sugiura, I. Yamauchi, T. Taniguchi, and Y. Itoh. Proposal for an optimum water management method using two-pole simultaneous measurement. *J. Power Sources*, 193(1):1–8, 2009.

[119] I. S. Hussaini and C. Y. Wang. Vizualisation and quantification of cathode channel flooding in PEM fuel cells. *J. Power Sources*, 187:444—451, 2009.

[120] H. P. Ma, H. M. Zhang, J. Hu, Y. H. Cai, and B. L. Yi. Diagnostic tool to detect liquid water removal in the cathode channels of proton exchange membrane fuel cells. *J. Power Sources*, 162:469 – 473, 2006.

[121] J. Borrelli, S Kandlikar, T Trabold, and J. Owejan. Water transport visualization and two-phase pressure drop measurements in a simulated PEMFC cathode minichannel. In *Proceedings of the 3rd international Conference on Microchannels and Minichannels*, Toronto, Ontario, Canada, June 13-15 2005.

[122] K. Sugiura, M. Nakata, T. Yodo, Y. Nishiguchi, M. Yamauchi, and Y. Itoh. Evaluation of a cathode gas channel with a water absorption layer/waste channel in a PEFC by using visualization technique. *J. Power Sources*, 145(2):526–533, 2005.

[123] E. C. Kumbur, K. V. Sharp, and M. M. Mench. Liquid droplet behavior and instability in a polymer electrolyte fuel cell flow channel. *J. Power Sources*, 161(1):333–345, 2006.

[124] F. B. Weng, A. Su, C. Y. Hsu, and C. Y. Lee. Study of water-flooding behaviour in cathode channel of a transparent proton-exchange membrane fuel cell. *J. Power Sources*, 157(2):674–680, 2006.

[125] X. G. Yang, F. Y. Zhang, A. L. Lubawy, and C. Y. Wang. Visualization of liquid water transport in a PEFC. *Electrochem. Solid State Lett.*, 7(11):A408–A411, 2004.

[126] A. Theodorakakos, T. Ous, A. Gavaises, J. M. Nouri, N. Nikolopoulos, and H. Yanagihara. Dynamics of water droplets detached from porous surfaces of relevance to PEM fuel cells. *J. Colloid Interface Sci.*, 300(2):673–687, 2006.

[127] S. Litster, D. Sinton, and N. Djilali. Ex situ visualization of liquid water transport in PEM fuel cell gas diffusion layers. *J. Power Sources*, 154(1):95–105, 2006.

[128] A. Bazylak, D. Sinton, and N. Djilali. Dynamic water transport and droplet emergence in PEMFC gas diffusion layers. *J. Power Sources*, 176(1):240–246, 2008.

[129] E. Kimball, T. Whitaker, Y. G. Kevrekidis, and J. B. Benziger. Drops, slugs, and flooding in polymer electrolyte membrane fuel cells. *AICHE J.*, 54(5):1313–1332, 2008.

[130] Z. Lu, S. G. Kandlikar, C. Rath, M. Grimm, W. Domigan, A. D. White, M. Hardbarger, J. P. Owejan, and T. A. Trabold. Water management studies in PEM fuel cells, Part II: Ex situ investigation of flow maldistribution, pressure drop and two-phase flow pattern in gas channels. *Int. J. Hydrog. Energy*, 34(8):3445–3456, 2009.

[131] B. Gao, T. S. Steenhuis, Y. Zevi, J. Y. Parlange, R. N. Carter, and T. A. Trabold. Visualization of unstable water flow in a fuel cell gas diffusion layer. *J. Power Sources*, 190(2):493–498, 2009.

[132] S. Basu, H. Xu, M. W. Renfro, and B. M. Cetegen. In situ optical diagnostics for measurements of water vapor partial pressure in a PEM fuel cell. *J. Fuel Cell Sci. Technol.*, 3(1):1–7, 2006.

[133] S. Basu, M. W. Renfro, H. Gorgun, and B. M. Cetegen. In situ simultaneous measurements of temperature and water partial pressure in a PEM fuel cell under steady state and dynamic cycling. *J. Power Sources*, 159(2):987–994, 2006.

[134] S. Basu, M. W. Renfro, and B. M. Cetegen. Spatially resolved optical measurements of water partial pressure and temperature in a PEM fuel cell under dynamic operating conditions. *J. Power Sources*, 1662:286–293, 2006.

[135] S. Basu, D. E. Lambe, and R. Kumar. Water vapor and carbon dioxide species measurements in narrow channels. *Int. J. Heat Mass Transf.*, 53(4):703–714, 2010.

[136] R. Sur, T. J. Boucher, M. W. Renfro, and B. M. Cetegen. In situ measurements of water vapor partial pressure and temperature dynamics in a PEM fuel cell. *J. Electrochem. Soc.*, 157(1):B45–B53, 2010.

[137] R. Sur, T. J. Boucher, M. W. Renfro, and B. M. Cetegen. Technique of laser calibration for wavelength-modulation spectroscopy with application to proton exchange membrane fuel cell measurements. *Appl. Optics*, 49(1):61–70, 2010.

[138] K. Fushinobu, K. Shimizu, N. Miki, and K. Okazaki. Optical measurement technique of water contents in polymer membrane for PEFCs. *J. Fuel Cell Sci. Technol.*, 3(1):13–17, 2006.

[139] S. Morita, Y. Jojima, Y. Miyata, and K. Kitagawa. Near-infrared imaging of water in a polymer electrolyte membrane during a fuel cell operation. *Anal. Chem.*, 82(22):9221–9224, 2010.

[140] M. M. Mench, Q. L. Dong, and C. Y. Wang. In situ water distribution measurements in a polymer electrolyte fuel cell. *J. Power Sources*, 124(1):90–98, 2003.

[141] Q. Dong, J. Kull, and M. M. Mench. Real-time water distribution in a polymer electrolyte fuel cell. *J. Power Sources*, 139(1-2):106–114, 2005.

[142] Q. Dong, M. M. Mench, S. Cleghorn, and U. Beuscher. Distributed performance of polymer electrolyte fuel cells under low-humidity conditions. *J. Electrochem. Soc.*, 152(11):A2114–A2122, 2005.

[143] G. A. Schuler, A. Wokaun, and F. N. Buchi. Local online gas analysis in PEFC using tracer gas concepts. *J. Power Sources*, 195(6):1647–1656, 2010.

[144] H. Nishikawa, R. Kurihara, S. Sukemori, T. Sugawara, H. Kobayasi, S. Abe, T. Aoki, Y. Ogami, and A. Matsunaga. Measurements of humidity and current distribution in a PEFC. *J. Power Sources*, 155(2):213–218, 2006.

[145] G. Hinds, M. Stevens, J. Wilkinson, M. de Podesta, and S. Bell. Novel in situ measurements of relative humidity in a polymer electrolyte membrane fuel cell. *J. Power Sources*, 186(1):52–57, 2009.

[146] N. A. David, P. M. Wild, J. Jensen, T. Navessin, and N. Djilali. Simultaneous in situ measurement of temperature and relative humidity in a PEMFC using optical fiber sensors. *J. Electrochem. Soc.*, 157(8):B1173–B1179, 2010.

[147] O. Herrera, W. Merida, and D. P. Wilkinson. Sensing electrodes for failure diagnostics in fuel cells. *J. Power Sources*, 190(1):103–109, 2009.

[148] S. J. C. Cleghorn, C. R. Derouin, M. S. Wilson, and S. Gottesfeld. A printed circuit board approach to measuring current distribution in a fuel cell. *J. Appl. Electrochem.*, 28(7):663–672, 1998.

[149] L. C. Perez, L. Brandao, J. M. Sousa, and A. Mendes. Segmented polymer electrolyte membrane fuel cells - A review. *Renew. Sust. Energ. Rev.*, 15(1):169–185, 2011.

[150] J. R. Claycomb, A. Brazdeikis, M. Le, R. A. Yarbrough, G. Gogoshin, and J. H. Miller. Nondestructive testing of PEM fuel cells. *IEEE Trans. Appl. Supercond.*, 13(2):211–214, 2003.

[151] Candusso D, B. Poirot-Crouvezier, J. P. andBador, E. Rulliere, R. Soulier, and J. Y. Voyant. Determination of current density distribution in proton exchange membrane fuel cells. *Eur. Phys. J. Appl. Phys.*, 25:67–74, 2004.

[152] K. H. Hauer, R. Potthast, T. Wuster, and D. Stolten. Magnetotomography: A new method for analysing fuel cell performance and quality. *J. Power Sources*, 143(1-2):67–74, 2005.

[153] S. Tsushima, K. Teranishi, and S. Hirai. Magnetic resonance imaging of the water distribution within a polymer electrolyte membrane in fuel cells. *Electrochem. Solid State Lett.*, 7(9):A269–A272, 2004.

[154] S. Tsushima, K. Teranishi, K. Nishida, and S. Hirai. Water content distribution in a polymer electrolyte membrane for advanced fuel cell system with liquid water supply. *Magn. Reson. Imaging*, 23(2):255–258, 2005.

[155] K. Teranishi, S. Tsushima, and S. Hirai. Analysis of water transport in PEFCs by magnetic resonance imaging measurement. *J. Electrochem. Soc.*, 153(4):A664–A668, 2006.

[156] K. Teranishi, S. Tsushima, and S. Hirai. Study of the effect of membrane thickness on the performance of polymer electrolyte fuel cells by water distribution in a membrane. *Electrochem. Solid State Lett.*, 8(6):A281–A284, 2005.

[157] S. Tsushima, S. Hirai, K. Kitamura, M. Yamashita, and S. Takasel. MRI application for clarifying fuel cell performance with variation of polymer electrolyte membranes: Comparison of water content of a hydrocarbon membrane and a perflourinated membrane. *Appl. Magn. Reson.*, 32(1-2):233–241, 2007.

[158] J. C. Perrin, S. Lyonnard, A. Guillermo, and P. Levitz. Water dynamics in ionomer membranes by field-cycling NMR relaxometry. *J. Phys. Chem. B*, 110:5439–5444, 2006.

[159] K. W. Feindel, L. P. A. LaRocque, D. Starke, S. H. Bergens, and R. E. Wasylishen. In situ observations of water production and distribution in an operating H_2/O_2 PEM fuel cell assembly using H-1 NMR microscopy. *J. Am. Chem. Soc.*, 126(37):11436–11437, 2004.

[160] K. W. Feindel, S. H. Bergens, and R. E. Wasylishen. The use of H-1 NMR microscopy to study proton-exchange membrane fuel cells. *ChemPhysChem*, 7(1):67–75, 2006.

[161] K. Feindel, S. Bergens, and R. Wasylishen. Insights into the distribution of water in a self-humidifying H_2/O_2 proton-exchange membrane fuel cell using H NMR microscopy. *J. Amer. Chem. Soc.*, 128:14192–14199, 2006.

[162] K. Feindel, S. Bergens, and R. Wasylishen. The influence of membrane electrode assembly water content on the performance of a polymer electrolyte membrane fuel cell as investigated by H NMR microscopy. *Phys. Chem. Chem. Phys.*, 9:1850–1857, 2007.

[163] K. Feindel, S. Bergens, and R. Wasylishen. Use of hydrogen-deuterium exchange for contrast in ^{1}H NMR microscopy investigations of an operating PEM fuel cell. *J. Power Sources*, 173(1):86–95, 2007.

[164] Paul D. Majors Li-Qiong Wang Minard Kevin R., Vilayanur V. Viswanathan and Peter C. Rieke. Magnetic resonance imaging (MRI) of PEM dehydration and gas manifold flooding during continuous fuel cell operation. *Journal of Power Sources*, in press:on press, 2006.

[165] I. Manke, C. Hartnig, M. Grunerbel, W. Lehnert, N. Kardjilov, A. Haibel, A. Hilger, J. Banhart, and H. Riesemeier. Investigation of water evolution and transport in fuel cells with high resolution synchrotron X-ray radiography. *Appl. Phys. Lett.*, 90(17):1–3, 2007.

[166] V. R. Albertini, B. Paci, A. Generosi, S. Panero, M. A. Navarra, and M. di Michiel. In situ XRD studies of the hydration degree of the polymeric membrane in a fuel cell. *Electrochem. Solid State Lett.*, 7(12):A519–A521, 2004.

[167] A. Isopo and R. Albertini. An original laboratory X-ray diffraction method for in situ investigations on the water dynamics in a fuel cell proton exchange membrane. *J. Power Sources*, 184:23–28, 2008.

[168] P. K. Sinha, P. Halleck, and C. Y. Wang. Quantification of liquid water saturation in a PEM fuel cell diffusion medium using X-ray microtomography. *Electrochem. Solid State Lett.*, 9(7):A344–A348, 2006.

[169] S. J. Lee, N. Y. Lim, S. Kim, G. G. Park, and C. S. Kim. X-ray imaging of water distribution in a polymer electrolyte fuel cell. *J. Power Sources*, 185(2):867–870, 2008.

[170] T. Mukaide, S. Mogi, J. Yamamoto, A. Morita, S. Koji, K. Takada, K. Uesugi, K. Kajiwara, and T. Noma. In situ observation of water distribution and behaviour in a polymer electrolyte fuel cell by synchrotron X-ray imaging. *J. Synchrot. Radiat.*, 15:329–334, 2008.

[171] C. Hartnig, I. Manke, R. Kuhn, N. Kardjilov, J. Banhart, and W. Lehnert. Cross-sectional insight in the water evolution and transport in polymer electrolyte fuel cells. *Appl. Phys. Lett.*, 92(13):134106, 2008.

[172] R. Mukundan and R. L. Borup. Visualising liquid water in PEM fuel cells using neutron imaging. *Fuel Cells*, 9:499–505, 2009.

[173] R. J. Bellows, M. Y. Lin, M. Arif, A. K. Thompson, and D. Jacobson. Neutron imaging technique for in situ measurement of water transport gradients within Nafion in polymer electrolyte fuel cells. *J. Electrochem. Soc.*, 146(3):1099–1103, 1999.

[174] J. M. Le Canut, R. Latham, W. Merida, and D. A. Harrington. Impedance study of membrane dehydration and compression in proton exchange membrane fuel cells. *J. Power Sources*, 192(2):457–466, 2009.

[175] J. St Pierre, D. P. Wilkinson, S. Knights, and M. L. Bos. Relationships between water management, contamination and lifetime degradation in PEFC. *J. New Mat.Electrochem. Syst.*, 3(2):99–106, 2000.

[176] T. R. Ralph and M. P. Hogarth. Catalysis for low temperature fuel cells part I: The cathode challenges. *Platin. Met. Rev.*, 46(1):3–14, 2002.

[177] S. D. Knights, K. M. Colbow, J. St-Pierre, and D. P. Wilkinson. Aging mechanisms and lifetime of PEFC and DMFC. *J. Power Sources*, 127(1-2):127–134, 2004.

[178] F. N. Büchi, A. Marek, and G. G. Scherer. In-situ membrane resistance measurements in polymer electrolyte fuel-cells by fast auxiliary current pulses. *J. Electrochem. Soc.*, 142(6):1895–1901, 1995.

[179] F. N. Büchi and G. G. Scherer. In-situ resistance measurements of Nafion 117 membranes in polymer electrolyte fuel cells. *J. Electroanal. Chem.*, 404(1):37–43, 1996.

[180] F. N. Büchi and G. G. Scherer. Investigation of the transversal water profile in Nafion membranes in polymer electrolyte fuel cells. *J. Electrochem. Soc.*, 148(3):A183–A188, 2001.

[181] T. Mennola, M. Mikkola, M. Noponen, T. Hottinen, and P. Lund. Measurement of ohmic voltage losses in individual cells of a PEMFC stack. *J. Power Sources*, 112(1):261–272, 2002.

[182] M. Noponen, T. Hottinen, T. Mennola, M. Mikkola, and P. Lund. Determination of mass diffusion overpotential distribution with flow pulse method from current distribution measurements in a PEMFC. *J. Appl. Electrochem.*, 32(10):1081–1089, 2002.

[183] F. Jaouen, G. Lindbergh, and K. Wiezell. Transient techniques for investigating mass-transport limitations in gas diffusion electrodes - II. Experimental characterization of the PEFC cathode. *J. Electrochem. Soc.*, 150(12):A1711–A1717, 2003.

[184] T. Abe, H. Shima, K. Watanabe, and Y. Ito. Study of PEFCs by AC impedance, current interrupt and dew point measurements I. Effect of humidity in oxygen gas. *J. Electrochem. Soc.*, 151(1):A101–A105, 2004.

[185] M. Smith, K. Cooper, D. Johnson, and L. Scribner. Advanced fuel cell diagnostic techniques for measuring MEA resistance. Technical report, Scribner Associates Inc., 2005.

[186] H. Yamada, T. Hatanaka, H. Murata, and Y. Morimoto. Measurement of flooding in gas diffusion layers of polymer electrolyte fuel cells with conventional flow field. *J. Electrochem. Soc.*, 153(9):A1748–A1754, 2006.

[187] F. Barbir, H. Gorgun, and X. Wang. Relationship between pressure drop and cell resistance as a diagnostic tool for PEM fuel cells. *J. Power Sources*, 141(1):96–101, 2005.

[188] W. S. He, G. Y. Lin, and T. Van Nguyen. Diagnostic tool to detect electrode flooding in proton-exchange-membrane fuel cells. *AICHE J.*, 49(12):3221–3228, 2003.

[189] A. D. Bosco and M. H. Fronk. Fuel cell flooding detection and correction. US Patent 6,103,409, August 15 2000.

[190] E. Stumper, M. Lohr, and S. Hamada. Diagnostic tools for liquid water in PEM fuel cells. *J. Power Sources*, 143(1-2):150–157, 2005.

[191] A. J. Bard and L. R. Faulkner. *Electrochemical Methods: Fundamentals and Applications*. Wiley, 2nd edition, 2001.

[192] E. Barsoukov and J. R. MacDonald. *Impedance Spectroscopy: Theory, Experiment, and Applications*. John Wiley and Sons, 2 edition, 2005.

[193] M. E. Orazem and B. Tribollet. *Electrochemical Impedance Spectroscopy*, volume 48 of *The Electrochemical Society Series*. Wiley-Interscience, 2008.

[194] X.Z. Yuan, C. Song, H. Wang, and J. Zhang. *Electrochemical Impedance Spectroscopy in PEM Fuel Cells: Fundamentals and Applications*. Springer, 2009.

[195] T. J. P. Freire and E. R. Gonzalez. Effect of membrane characteristics and humidification conditions on the impedance response of polymer electrolyte fuel cells. *J. Electroanal. Chem.*, 503(1-2):57–68, 2001.

[196] B. H. Andreaus. *Die Polymer-Elektrolyt Brennstoffzelle – Charakterisierung ausgewählter Phänomene durch elektrochemische Impedanzspektroskopie*. PhD thesis, École Polytechnique Fédérale de Lausanne, 2002.

[197] W. Merida, D. A. Harrington, J. M. Le Canut, and G. McLean. Characterisation of proton exchange membrane fuel cell (PEMFC) failures via electrochemical impedance spectroscopy. *J. Power Sources*, 161(1):264–274, 2006.

[198] N. Fouquet, C. Doulet, C. Nouillant, G. Dauphin-Tanguy, and B. Ould-Bouamama. Model based PEM fuel cell state-of-health monitoring via AC impedance measurements. *J. Power Sources*, 159(2):905–913, 2006.

[199] J. M. Le Canut, R. M. Abouatallah, and D. A. Harrington. Detection of membrane drying, fuel cell flooding, and anode catalyst poisoning on PEMFC stacks by electrochemical impedance spectroscopy. *J. Electrochem. Soc.*, 153(5):A857–A864, 2006.

[200] C. V. G. Reddy, P. K. Dutta, and S. A. Akbar. Detection of CO in a reducing, hydrous environment using CuBr as electrolyte. *Sens. Actuator B-Chem.*, 92(3):351–355, 2003.

[201] A. M. Azad and M. Hammoud. Fine-tuning of ceramic-based chemical sensors via novel microstructural modification I: Low level CO sensing by tungsten oxide, WO3. *Sens. Actuator B-Chem.*, 119(2):384–391, 2006.

[202] A. M. Azad. Fine-tuning of ceramic-based chemical sensors via novel microstructural modificationpart II: Low level CO sensing by molybdenum oxide, MoO3. *Sens. Actuator B-Chem.*, 120(1):25–34, 2006.

[203] A. Hashimoto, T. Hibino, and M. Sano. A fuel-cell-type sensor for detection of carbon monoxide in reformed gases. *Electrochem. Solid State Lett.*, 5(2):H1–H3, 2002.

[204] K. W. Kirby, A. C. Chu, and K. C. Fuller. Detection of low level carbon monoxide in hydrogen-rich gas streams. *Sens. Actuator B-Chem.*, 95(1-3):224–231, 2003.

[205] R. Mukundan, E. L. Brosha, and F. H. Garzon. A low temperature sensor for the detection of carbon monoxide in hydrogen. *Solid State Ion.*, 175(1-4):497–501, 2004.

[206] C. Pijolat, G. Tournier, and J. P. Viricelle. CO detection in H_2 reducing atmosphere with mini fuel cell. *Sens. Actuator B-Chem.*, 156(1):283–289, 2011.

[207] T.E. Springer, T.A. Zawodzinski, and S. Gottesfeld. Modelling of polymer electrolyte fuel cell performance with reformate feed streams: Effects of low levels

of CO in hydrogen. In McBreen J., S Muckerjee, and Srinivasan S., editors, *Electrode Materials and Processes for Energy Conversion and Storage*, volume 97 of *The Electrochemical Society Proceedings*, pages 15 – 24, 1997.

[208] S. J. Lee, S. Mukerjee, E. A. Ticianelli, and J. McBreen. Electrocatalysis of CO tolerance in hydrogen oxidation reaction in PEM fuel cells. *Electrochim. Acta*, 44(19):3283–3293, 1999.

[209] G. A. Camara, E. A. Ticianelli, S. Mukerjee, S. J. Lee, and J. McBreen. The CO poisoning mechanism of the hydrogen oxidation reaction in proton exchange membrane fuel cells. *J. Electrochem. Soc.*, 149(6):A748–A753, 2002.

[210] P. P. Lopes and E. A. Ticianelli. The CO tolerance pathways on the Pt-Ru electrocatalytic system. *J. Electroanal. Chem.*, 644(2):110–116, 2010.

[211] C. H. Hamann, A. Hamnett, and W. Vielstich. *Electrochemistry*. Wiley-VCH, 2007.

[212] D. J. L. Brett, S. Atkins, N. P. Brandon, V. Vesovic, N. Vasileiadis, and A. R. Kucernak. Investigation of reactant transport within a polymer electrolyte fuel cell using localised CO stripping voltammetry and adsorption transients. *J. Power Sources*, 133(2):205–213, 2004.

[213] M. Ciureanu and H. Wang. Electrochemical impedance study of anode CO-poisoning in PEM fuel cells. *J. New Mat. Electrochem. Syst.*, 3(2):107–119, 2000.

[214] J. D. Kim, Y. I. Park, K. Kobayashi, M. Nagai, and M. Kunimatsu. Characterization of CO tolerance of PEMFC by AC impedance spectroscopy. *Solid State Ion.*, 140(3-4):313–325, 2001.

[215] N. Wagner and M. Schulze. Change of electrochemical impedance spectra during CO poisoning of the Pt and Pt-Ru anodes in a membrane fuel cell (PEFC). *Electrochim. Acta*, 48(25-26):3899–3907, 2003.

[216] Yu. Bessarab, I. Merfert, W. Fischer, and A. Lindemann. Different control methods of bidirectional DC-DC converters for fuel cell power systems. In *PCIM Europe 2008. International Exhibition & Conference for Power Electronics Intelligent Motion Power Quality*, page 5 pp. Mesago PCIM GmbH, Stuttgart, Germany, 2008.

[217] T. Kadyk, R. Hanke-Rauschenbach, and K. Sundmacher. Nonlinear frequency response analysis of PEM fuel cells for diagnosis of dehydration, flooding and CO-poisoning. *J. Electroanalyt. Chem.*, 630:19 – 27, 2009.

[218] M. Ciureanu and R. Roberge. Electrochemical impedance study of PEM fuel cells. experimental diagnostics and modeling of air cathodes. *J. Phys. Chem. B*, 105(17):3531–3539, 2001.

[219] V. A. Paganin, C. L. F. Oliveira, E. A. Ticianelli, T. E. Springer, and E. R. Gonzalez. Modelistic interpretation of the impedance response of a polymer electrolyte fuel cell. *Electrochim. Acta*, 43(24):3761 – 3766, 1998.

[220] S. O. Engblom, J. C. Myland, and K. B. Oldham. Must AC voltammetry employ small signals? *J. Electroanal. Chem.*, 480(1-2):120–132, 2000.

[221] D. J. Gavaghan and A. M. Bond. A complete numerical simulation of the techniques of alternating current linear sweep and cyclic voltammetry: analysis of a reversible process by conventional and fast fourier transform methods. *J. Electroanal. Chem.*, 480(1-2):133–149, 2000.

[222] D. E. Smith. *Electroanalytical Chemistry: A Series of Advances*. Marcel Dekker, New York, 1966.

[223] J. Jankowski. Electrochemical methods for corrosion rate determination under cathodic polarisation conditions: A review. Part 2: AC methods. *Corros. Rev.*, 20(3):179–200, 2002.

[224] K. Darowicki and J. Majewska. Harmonic analysis of electrochemical and corrosion systems – A review. *Corros. Rev.*, 17(5-6):383–399, 1999.

[225] A. Groysman. Corrosion monitoring. *Corros. Rev.*, 27(4-5):205–343, 2009.

[226] Q. Mao, U. Krewer, and R. Hanke-Rauschenbach. Total harmonic distortion analysis for direct methanol fuel cell anode. *Electrochem. Commun.*, 12:1517 – 1519, 2010.

[227] Q. Mao, U. Krewer, and R. Hanke-Rauschenbach. Comparative studies on linear and nonlinear frequency response for direct methanol fuel cell anode. *Submitted to J. Electrochem. Soc.*, 2011.

[228] B. Bensmann, M. Petkovska, T. Vidaković-Koch, R. Hanke-Rauschenbach, and K. Sundmacher. Nonlinear frequency response of electrochemical methanol oxidation kinetics: A theoretical analysis. *J. Electrochem. Soc.*, 157(9):B1279 – B1289, 2010.

[229] K. Darowicki. Fundamental-harmonic impedance of 1st-order elextrode reactions. *Electrochim. Acta*, 39(18):2757–2762, 1994.

[230] K. Darowicki. Corrosion rate measurements by nonlinear electrochemical impedance spectroscopy. *Corrosion Sci.*, 37(6):913–925, 1995.

[231] K. Darowicki. The amplitude analysis of impedance spectra. *Electrochim. Acta*, 40(4):439–445, 1995.

[232] D.D. Weiner and J.F. Spina. *Sinusoidal Analysis and Modeling of Weakly Nonlinear Circuits*. Van Nostrand Reinhold Company, New York, 1980.

[233] M. Petkovska. Nonlinear frequency response method for investigation of equilibria and kinetics of adsorption systems. In Aleksandar M. Spasic and Jyh-Ping Hsu, editors, *Finely Dispersed Particles – Micro-, Nano-, and Atto-Engineering*, chapter 12, pages 283 – 328. CRC Press, 2006.

[234] M. Petkovska and D. D. Do. Use of higher-order frequency response functions for identification of nonlinear adsorption kinetics: Single mechanisms under isothermal conditions. *Nonlinear Dyn.*, 21(4):353–376, 2000.

[235] Martin Schetzen. *The Volterra and Wiener theories of nonlinear systems*. Krieger Publishing Company, 2006.

[236] G. M. Lee. Estimation of non-linear system parameters using higher-order frequency response functions. *Mech. Syst. Signal Proc.*, 11(2):219–228, 1997.

[237] R. Kories and H. Schmidt-Walter. *Taschenbuch der Elektrotechnik*. Verlag Harri Deutsch, 4 edition, 2000.

[238] Xiaozi Yuan, J. C. Sun, M. Blanco, H. Wang, J. Zhang, and D. P. Wilkinson. AC impedance diagnosis of a 500 W PEM fuel cell stack - Part I: Stack impedance. *J. Power Sources*, 161(2):920 – 928, 2006.

[239] K. Wiezell, P. Gode, and G. Lindbergh. Steady-state and EIS investigations of hydrogen electrodes and membranes in polymer electrolyte fuel cells I. Modeling. *J. Electrochem. Soc.*, 153(4):A749–A758, 2006.

[240] K. Wiezell, P. Gode, and G. Lindbergh. Steady-state and EIS investigations of hydrogen electrodes and membranes in polymer electrolyte fuel cells II. Experimental. *J. Electrochem. Soc.*, 153(4):A759–A764, 2006.

[241] S. K. Roy, M. E. Orazem, and B Tribollet. Interpretation of low-frequency inductive loops in PEM fuel cells. *J. Electrochem. Soc.*, 154(12):B1378–B1388, 2007.

[242] D.P. Wilkinson and J. St-Pierre. Durability. In W. Vielstich, A. Lamm, and H. Gasteiger, editors, *Handbook of Fuel Cells – Fundamentals, Technology and Applications*, volume 3, page 611. John Wiley & Sons, Ltd., New York, 2003.

[243] M. Fowler, R. F. Mann, J. C. Amphlett, B. A. Peppley, and P. R. Roberge. Reliability issues and voltage degradation. In W. Vielstich, A. Lamm, and H. Gasteiger, editors, *Handbook of Fuel Cells – Fundamentals, Technology and Applications*, volume 3, page 663. John Wiley & Sons, Ltd., New York, 2003.

[244] J. X. Zhang, T. Thampan, and R. Datta. Influence of anode flow rate and cathode oxygen pressure on CO poisoning of proton exchange membrane fuel cells. *J. Electrochem. Soc.*, 149(6):A765–A772, 2002.

[245] A. H. Thomason, T. R. Lalk, and A. J. Appleby. Effect of current pulsing and "self oxidation" on the CO tolerance of a PEM fuel cell. *J. Power Sources*, 135:204 – 211, 2004.

[246] C. G. Farell, C. L. Gardner, and M Ternan. Experimental and modelling studies of CO poisoning in PEM fuel cells. *J. Power Sources*, 171:282 – 293, 2007.

[247] J. J. Zhang, H. J. Wang, D. P. Wilkinson, D. T. Song, J. Shen, and Z. S. Liu. Model for the contamination of fuel cell anode catalyst in the presence of fuel stream impurities. *J. Power Sources*, 147(1-2):58–71, 2005.

[248] J. Siegmeier, N. Baba, and K. Krischer. Bistability and oscillations during electrooxidation of H_2 – CO mixtures on Pt: Modeling and bifurcation analysis. *J. Phys. Chem. C*, 111:13481–13489, 2007.

[249] M. C. Deibert and D. L. Williams. Voltage oscillations of H_2-CO system. *J. Electrochem. Soc.*, 116(9):1290–1292, 1969.

[250] S. Szpak. Potential oscillations of H_2-CO system at low CO content. *J. Electrochem. Soc.*, 117(8):1056–1058, 1970.

[251] T. Yamazaki, T. Kodera, R. OHNISHI, and M. MASUDA. Potential oscillation during anodic oxidation of hydrogen at a platinum electrode. 2. Kinetic analysis. *Electrochim. Acta*, 35(2):431–435, 1990.

[252] G. Kohlmayr and Stonehart.P. Adsorption kinetics for carbon-monoxide on platinum in hot phosphoric acid. *Electrochim. Acta*, 18(2):211–223, 1973.

[253] J. J. Baschuk and X. G. Li. Modelling CO poisoning and O_2 bleeding in a PEM fuel cell anode. *Int. J. Energy Res.*, 27(12):1095–1116, 2003.

[254] N.M. Marković, B.N. Grgur, and P.N. Ross. Temperature-dependent hydrogen electrochemistry on platinum low-index single-crystal surfaces in acid solutions. *J. Phys. Chem. B*, 101:5405–5413, 1997.

[255] J.X. Wang, T.E. Springer, and R.R. Adzic. Dual-pathway kinetic equation for the hydrogen oxidation reaction on Pt electrodes. *J. Electrochem. Soc.*, 153:A1732–A1740, 2006.

[256] N. R. Elezović, L. Gajic-Krstajic, V. Radmilovic, L. Vracar, and N. V. Krstajic. Effect of chemisorbed carbon monoxide on Pt/C electrode on the mechanism of the hydrogen oxidation reaction. *Electrochim. Acta*, 54(4):1375–1382, 2009.

[257] S.A. Vilekar, I. Fishtik, and R. Datta. Kinetics of the hydrogen electrode reaction. *J. Electrochem. Soc.*, 157(7):B1040–B1050, 2010.

[258] A. Bonnefont, H. Varela, and K. Krischer. Stationary spatial patterns during bulk CO electrooxidation on platinum. *J. Phys. Chem. B*, 109(8):3408–3415, 2005.

[259] R. Morschl, J. Bolten, A. Bonnefont, and K. Krischer. Pattern formation during CO electrooxidation on thin Pt films studied with spatially resolved infrared absorption spectroscopy. *J. Phys. Chem. B*, 112(26):9548–9551, 2008.

[260] P.R. Bauer, A. Bonnefont, and K. Krischer. Spatially resolved ATR-FTIRS study of the formation of macroscopic domains and microislands during CO electrooxidation on Pt. *Chem. Phys. Chem.*, 11(13):3002–3010, 2010.

[261] J. D. Kim, Y. I. Park, K. Kobayashi, and M. Nagai. Effect of CO gas and anode-metal loading on H_2 oxidation in proton exchange membrane fuel cell. *J. Power Sources*, 103(1):127–133, 2001.

[262] N. Wagner and E. Gülzow. Change of electrochemical impedance spectra (EIS) with time during CO-poisoning of the Pt-anode in a membrane fuel cell. *J. Power Sources*, 127(1-2):341–347, 2004.

[263] M. Ciureanu, H. Wang, and Z. G. Qi. Electrochemical impedance study of membrane-electrode assemblies in PEM fuel cells. II. Electrooxidation of H_2 and H_2/CO mixtures on Pt/Ru-based gas-diffusion electrodes. *J. Phys. Chem. B*, 103(44):9645–9657, 1999.

[264] A.W. Adamson. *Physical Chemistry of Surfaces*. Interscience, 1967.

[265] A. A. Shah, P. C. Sui, G. S. Kim, and S. Ye. A transient PEMFC model with CO poisoning and mitigation by O_2 bleeding and Ru-containing catalyst. *J. Power Sources*, 166(1):1–21, 2007.

[266] T. Ioroi, T. Akita, S. Yamazaki, Z. Siroma, N. Fujiwara, and K. Yasuda. Comparative study of carbon-supported Pt/Mo-oxide and PtRu for use as CO-tolerant anode catalysts. *Electrochim. Acta*, 52(2):491–498, 2006.

[267] J. X. Zhang and R. Datta. Sustained potential oscillations in proton exchange membrane fuel cells with PtRu as anode catalyst. *J. Electrochem. Soc.*, 149(11):A1423–A1431, 2002.

[268] J. Heyrovský. A theory of overpotential. *Recl. Trav. Chim. Pays-Bas*, 46:582 – 585, 1927.

[269] J. S. Newman. *Electrochemical Systems*, chapter 5, pages 116 – 133. Prentice-Hall, New Jersey, 2nd edition, 1991.

[270] T. E. Springer, T. A. Zawodzinski, and S. Gottesfeld. Polymer electrolyte fuel cell model. *J. Electrochem. Soc.*, 138(8):2334–2341, August 1991.

[271] L. A. Belfiore. *Transport Phenomena for Chemical Reactor Design*. John Wiley & Sons, 2003.